Residual Strain Analysis via a Non-Bonded Interface Technique in Comparison to a Finite Element Model

by

Brandon Gorman

Submitted in partial fulfilment of the requirements
for the degree of Master of Applied Science

at

Dalhousie University
Halifax, Nova Scotia
August 2019

Table of Contents

List of Tables

List of Figures

Abstract

The determination of residual strains in materials after an applied load is an important quantity for the understanding of the deformation behaviour of materials. There exist many quantifying techniques to measure residual strains however these techniques have limitations when micro scale measurements are of interest. In this study a technique is developed capable of quantifying localized deformation at the microstructural level by utilizing a micro-array of pre-defined circles on the internal non-bonded interface of a split sample. By performing an indentation test on the circle array, the circles will deform along with the material. By measuring the major and minor axes of the plastically deformed circles, the residual principal total strains are determined.

The results from this non-bonded interface technique (NBIT) are then compared to results from a validated non-linear finite element (FE) model. Experimental homogeneous and split samples made of AISI 4340 steel were used. FE analysis was used to examine the effect of the internal non-bonded interface which showed that the split interface caused less than a 10% difference between the split and whole samples when measuring principal major and minor strains.

The residual principal major and minor strain were experimentally examined for 588.6N, 981.0N, and 1471.5N indentation forces and compared to the FE model. The results of which ranged from a percent difference of 25.99% for the principal minor strain from the 1471.4N indentation, to 69.94% for the principal minor strain from the 981.0N indentation. The large difference between the experimental and FE model was explained by the inability of the FE model to simulate the local nonhomogeneous nature of a multi-phase material, as well as the measurement errors caused by human involvement. From all of this analysis it was determined that NBIT can be utilized as a reliable internal residual strain analysis technique which has the capabilities of experimentally resolving residual principle micro strains with the main limitations being the circle measurement accuracy.

List of Abbreviations and Symbols Used

A	Johnson-Cook yield strength coefficient
A_i	Area of element face
B, n	Johnson-Cook strain hardening coefficients
BIT	Bonded Interface Technique
C	Dampening matrix
C	Johnson-Cook strain rate coefficient
EDM	Electro-Discharge Machining
E^*	Equivalent elastic modulus
FE	Finite Element
FIB	Focused Ion Beam
HRB	Rockwell B Hardness
K_i	Bulk modulus
K_s	Slave segment stiffness modulus
M	Mass matrix
MBN	Magnetic Barkhausen Noise
$NBIT$	Non-Bonded Interface Technique
P	Indentation force
R	Spherical radius
R^*	Relative curvature between two spherical bodies
SFM	Master scale factor
SFS	Slave scale factor
$SLSFAC$	Sliding scale factor
$SOFCL$	Stiffness factor
S_y	Shear yield strength
XRD	X-Ray Diffraction
Y	Yield strength
Δt_c	Initial timestep
α	Stiffness scaling factor
$\bar{\boldsymbol{K}}$	Dynamic tangential stiffness matrix

$\bar{g}_{n+1}$	Dynamic out of balance force
$\bar{g}_{n+1}$	Static out of balance force
β	Stiffness scale factor
$\ddot{d}_n$	Nodal acceleration
δ	Distance of mutual approach
$\dot{\epsilon}^*$	Effective plastic strain rate
$\dot{d}_n$	Nodal velocity
ϵ_p	Effective plastic strain
ϵ_{yp}	Elastic yield strain
γ	Angle of slip line intersection
γ, β	Newmark constants
λ	Incident x-ray wavelength
$[B]$	Interpolation matrix
$[D]$	Material elasticity matrix
ν	Poisson's ratio
σ_1	Principle major stress
σ_2	Principle hoop stress
σ_3	Principle minor stress
σ_θ	Hoop stress
σ_n	Mortar contact pressure
σ_r	Radial stress
σ_y	Effective stress
σ_z	Depth stress
τ_{max}	Maximum shear stress
τ_{rz}	Shear stress
$\mathbf{f}$	Interface force
θ	Diffraction scattering angle
ξ, ζ, η	Normalized coordinate system
a	Contact radius
a	Elemental displacement
c	Elastic constraint factor
d	Interplaner spacing
d	Penetration length
d_c^s	Characteristic length of slave segment in contact
d_n	Nodal displacement
e	Element identifier
f_{si}	Scale factor for stiffness factor
k	Elemental stiffness
k	Shear flow stress
k	Strength coefficient
k_i	Stiffness factor

k_{sc}	Soft constraint stiffness factor
l	Depth of interpenetration
m	Johnson-Cook thermal softening coefficient
m^*	Mass function of the slave and master nodes
n	Constructive order of reflection
n	Hardening coefficient
n	Number of nodes within element
n_i	Normal vector from point of contact
p_m	Mean contact pressure
p_r	Radial pressure distribution
q	Elemental force
$q_{i,n+1}$	Static external force
$q_{i,n+1}$	Static internal force
r	Radial distance
z	Distance below indentation
u_z	Hertzian boundary displacement
$\mu\sigma_n$	Tangential frictional stress

Acknowledgements

I would first like to thank my supervisors, Drs. Zoheir Farhat and Andrew Warkentin for their constant support, patience, availability, and extensive knowledge of materials, finite element theory, and technical communication which was essential for completing this research, and communicating the results. It is from both of these gentlemen's confidence in me, as well as their general efforts that I can say I have improved in being a researcher, technical communicator, as well as more generally, an individual. For these reasons, I will be forever grateful.

I would also like to thank my committee members, Drs. Darrel Doman and Uday Venkatadri for their support of this research work and review of my thesis, as well as the Natural Sciences and Engineering Research Council of Canada for their financial support which made this research possible.

The staff at Dalhousie also deserve recognition such as the machine shop staff for creating all of the samples used in this work, the Minerals Engineering Center for performing composition analysis, as well as Patricia Scallion for her constant support with utilizing the focused ion beam which played an essential role in this research. If not for these and many other staff at Dalhousie, research much like my own would simply not be possible.

Finally, I would like to thank my friends and family for their support over the past two years, but more specifically my partner Lindsay. If not for her diligent support, the perseverance required for this work would not have been found. I owe a lot of my success to her efforts via the confidence she instills in me, for which I stand where I am today. Thank you.

Chapter 1

Introduction

Indentation testing is one of the most commonly used techniques for materials characterization. After an indentation test occurs, residual deformations and strains are present in the material which typically remain unquantified. In general, residual strains within a material specimen can be beneficial or detrimental which is dependent upon the exact quantity. For example, if there is a fair amount of residual strain as from a shot-peening process, then the results will be beneficial where the surface properties improve due to the induced compressive layer. However, if there is too much residual strain, then the material can exhibit micro-cracking as well as ablation which compromises the integrity of the material. Therefore, measuring the exact quantity of residual strain within a material sample after an indentation test can be beneficial, especially in the field of new materials development and characterization.

There exist experimental residual strain analysis techniques which can analyze such a quantity, however, there is a general trade-off between measurement resolution to depth of analysis. On the scale of a standard indentation, current residual strain analysis techniques prove difficult to produce high resolution residual strain results. Therefore, this work presents a comparison between a new experimental residual strain analysis method called the non-bonded interface technique (NBIT), and a non-linear finite element (FE) model.

NBIT is a development based upon the bonded interface technique (BIT), where the experimental setup for BIT is shown in Figure 1.1 a. BIT utilizes two square samples of material, held together internally using an adhesive layer, and externally using a vice. An indentation is placed along the internal interface, where the residual internal deformations and damage can be directly observed once the adhesive layer is chemically removed. This technique was developed by Guiberteau et al [1] in 1994 and was used for several years in research for analyzing residual damage in brittle ceramics. That was until 2001 when Helbawi et al [2] determined that the split sample was not an accurate representation of a whole sample due to the bonded interface.

Therefore, in 2016, Almotairi [3] modified BIT to become NBIT as shown in Figure 1.1 b. This modification removed the bonded interface to allow for a direct contact between the two free surfaces. Almotairi also introduced a quantitative technique commonly used in sheet metal fabrication called the circular grid analysis technique [4]. The grid of circles for NBIT is applied to the internal interface using a focused ion beam (FIB) in order to resolve the internal residual major and minor strains. NBIT was utilized by Almotairi for analyzing the crack propagations in hard chromium coatings as well as for a preliminary examination on internal residual principal major and minor strains [3]. What was not completed with NBIT was an examination on the effect of the split interface, as well as any comparison between the experimental residual strain results from NBIT to any of the current existing residual strain analysis techniques.

This research is significant as it presents a comparison between current simulated residual strain analysis methods being the FE analysis, with the novel experimental method of

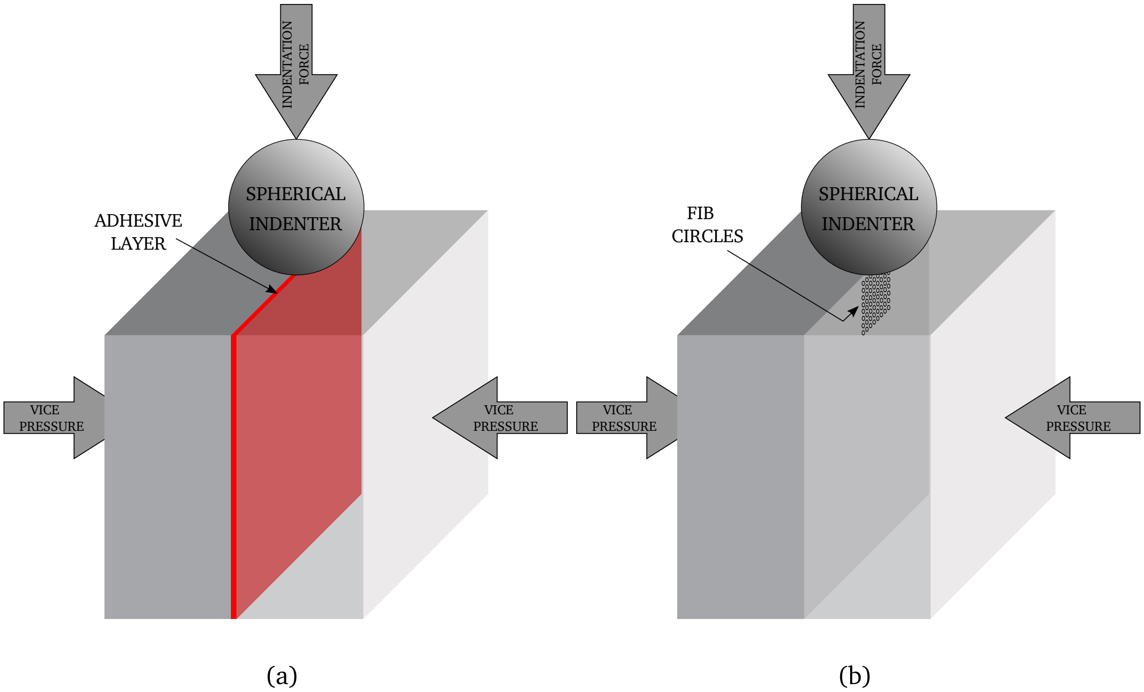

Figure 1.1: Experimental set-up diagrams of (a) Bonded interface technique and (b) Non-bonded interface technique

NBIT. The results of which will show agreement between the macro scale measurements from the FE model with micro scale measurements from NBIT.

1.1 Objectives

The objectives for this work are

- Investigate a novel technique to determine residual deformations at the material microstructural level using a micro-grid pattern on a split non-bonded interface.
- Create an accurate and experimentally validated FE model to determine the effect that the split interface has on the displacement, strain, and stress continuity across the interface.
- Compare analytical and experimental indentation data with the FE model.

- Examine residual strain distribution of AISI 4340 steel subjected to three indentation loads.

1.2 Thesis Outline

This work will be divided into 5 chapters. Chapter 2 will cover fundamental concepts in residual strain analysis, elastic and plastic deformation theory, and will review applicable FE theory. Chapter 3 will discuss the experimental procedure, circle optimization, and experimental setup along with the simulation methods used to discover optimal material model, material parameters, timestep, contact algorithm, element formulation, and element size for the FE model. Chapter 4 will present the experimental and FE results discovered via this work as well as discuss their significance. Chapter 5 will provide the summary of conclusions, contributions, and recommendations for future work.

Chapter 2

Background and Literature Review

2.1 Residual Strain Analysis

There are many different methods of residual strain analysis as the typical requirement is to measure a property of the material before and after a force is applied. Industrially these methods can be classified as either destructive or non-destructive. Both of these classifications can have techniques that measure either the residual elastic strain or the total strain being the combination of both residual elastic and plastic strain. The methods of x-ray diffraction (XRD) and the hole drilling technique measure the residual elastic strain which through Hooke's Law can be used for direct relation to the residual stress field within the sample. Other methods can also resolve the internal stress either through calibrated comparisons such as the acoustic wave analysis technique and the magnetic methods or through a finite element (FE) analysis such as from the contour method. One of the main focuses for these methods is the resolution of the determined results. The main factor that attributes to the resolution is the achievable gage dimension of the method. This gage dimension value is the length or diameter of the material being analyzed at any given time. Therefore, the smaller the gage dimension, the higher the resultant resolution will be.

2.1.1 Non-Destructive Techniques

The non-destructive testing methods are highly sought after for use in industry as they do not require the sample to be damaged, and in some cases can be used as a portable analysis technique. These non-destructive methods include x-ray diffraction, synchrotron x-ray diffraction, neutron diffraction, micro-Raman spectroscopy, acoustic wave analysis, and magnetic methods.

X-ray diffraction (XRD) techniques are one of the most common methods for residual strain analysis. This method uses a beam of monochromatic x-rays to excite the atomic structure of the desired specimen. Upon excitation, diffraction occurs where the emitted x-rays can be recorded and if a defined atomic plane is present the diffracted x-rays will constructively interfere causing large peaks in the recorded intensity. The general outline for this process is shown in Figure 2.1. This method can be used to measure the interatomic plane spacing through Bragg's law [5] which is defined as

$$n\lambda = 2d \sin\theta \tag{2.1}$$

where n is a positive integer representing the constructive order of reflection, λ is the wavelength of the incident x-ray, d is the interplanar spacing, and θ is the scattering angle.

Due to the simplicity of Bragg's Law, XRD is largely used for material characterization

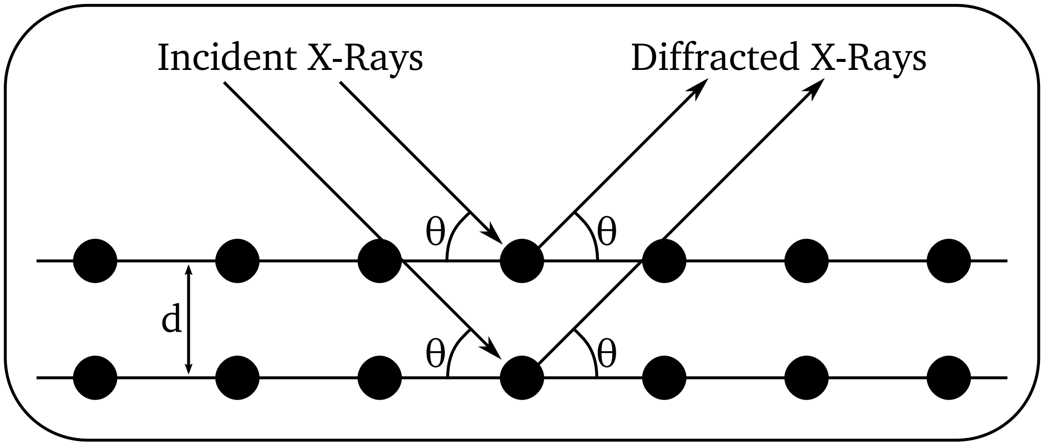

Figure 2.1: General outline of diffraction techniques where this example shows incident and emitted x-rays

however, it is also a useful technique for residual stress analysis. This is because as a sample is increasingly strained, the interatomic spacing will change. By comparing the measured to natural interatomic spacings, strain can be resolved which through Hooke's law can also be used for determining stress. This method is capable of a spatial resolution on the micron scale however the depth of penetration is limited to surface analysis (5-10µm depth) especially for polycrystalline materials [6, 7]. This small penetration depth can be mitigated by using a newer technique called synchrotron x-ray diffraction. Synchrotron x-ray diffraction is identical to the standard x-ray diffraction method however the initial energy from the x-rays are much higher due the use of a synchrotron. Therefore, this method is capable of a larger penetration depth on the order of 100µm as well as a small gage dimension of 20µm [7, 8].

Another similar method to x-ray diffraction is the neutron diffraction method. Due to the lower interaction of neutrons compared to x-rays, larger penetration depths are achievable with a maximum around 20mm [9, 8]. This low interaction increases the required time for analyzing a sample which causes a large gage size of over 100µm [7, 8]. The long count times and increased gage size can be a disadvantage for small penetration depths as other methods can provide faster counts with more precise results. For deeper analysis however, the count times can be advantageous as other techniques which can achieve the same penetration depth are typically destructive and are more tedious. Therefore, the neutron diffraction method is a useful technique for thick specimens which contain gradual stress gradients. The main disadvantage to this method is the requirement of a nuclear reactor for neutron generation and therefore most neutron experiments are completed within nuclear research facilities.

Micro-Raman spectroscopy is a technique that emits a focused beam of monochromatic light onto a desired surface. The incoming photons interact with the atoms of the material where the incoming energy is absorbed and scattered much like x-ray diffraction. This scattered light is either from elastic or inelastic scattering. The elastic scattering is when the resultant light has the same frequency as the initial light and is termed Rayleigh scattering. Inelastic scattering is when the frequency of the emitted photons is different than the incident photons and is termed Raman scattering [10]. Raman scattering consists of about 1/1000th of the total incoming energy while Rayleigh scattering contains the rest [10]. This micro-Raman technique measures this Raman scattering intensity to produce a total Raman spectrum as the frequency of the emitted light changes. For measuring residual strain this method uses the change in interatomic forces which causes the vibrational mode of the atoms to change and therefore the inelastically scattered energy will be different between a strained and unstrained sample [11]. These vibrational differences show themselves as a frequency shift in the resultant Raman spectrum [12]. By comparing the shift that occurs, the residual strain can be retrieved and much like XRD, the stresses can be resolved through Hooke's law. Micro-Raman spectroscopy is capable of providing spatial resolution on the sub-micron scale however the depth of penetration is also on the sub-micron scale and therefore this method is solely used for surface analysis [13, 7].

The acoustic wave analysis method sends a sound wave through the bulk of the material where the resultant velocity of the wave is recorded and is dependent upon the strain within the material [14]. By comparing the velocity from the strained to strain free sample the residual strain can be determined. By comparing these residual strain values to existing calibrations, the residual stress can also be determined. Due to the small change that the stress has on the sound wave even when the stress is on the order of the materials yield strength, the waves must be long [14]. Therefore, this method produces an inverse relation between the desired resolution and the accuracy of the results [7]. For the results from this method to be considered accurate, the resolution must be in the order of 1-10mm [7]. This method may not achieve the spatial resolution comparable to other methods however its ease of use allows it to be a portable analysis technique widely used in industry for residual stress analysis as well as internal crack monitoring.

The final set of non-destructive methods commonly used are the magnetic methods. These methods are used solely for magnetic materials and can be classified as either active or passive analysis [15]. In active magnetic analysis a moving magnetic field is applied to the material and the resultant magnetic response called the magnetic Barkhausen noise (MBN) emission is recorded. Peaks in the MBN emission are produced when a change in the magnetic field occurs such as around grain boundaries, dislocations, or any other micro-structural feature [16]. This is useful as the MBN will increase in the presence of residual strain. As active magnetic analysis applies a strong magnetic field, passive magnetic analysis uses the existing magnetic field from the earth [17]. This method works in a similar manner to the active MBN method where the micro-structural properties cause fluctuations in the measured magnetic response. The magnetic methods have historically been used for larger specimens as the spatial resolution was on the order of over 1mm [7]. With newer advancements in measurement equipment however, Robert et. al. [18] has been able to successfully use the passive magnetic method with a spatial resolution of 10μm. The recorded MBN from both the active and passive methods are resolved to residual stress through controlled testing, where various loadings are applied to a sample which generate a calibration curve relating the residual stress to MBN [19].

2.1.2 Destructive Techniques

Although the destructive techniques may not be highly utilized in industry, they still play an essential role in determining residual stress or strain especially in research and development. The destructive methods tend to be capable of large penetration depths and their main analysis factor is by measuring material relaxation. The destructive methods commonly used are the contour method, hole drilling and slitting methods, as well as the sectioning method.

The first residual strain analysis method was introduced by Mathar [20] and is the destructive hole-drilling method. The main purpose of this method is for surface stress analysis specifically when the sample is in a state of biaxial strain [21]. This method uses circular strain gauges on the surface of the specimen and by drilling a hole in the center the strain gauges will record the material relaxation that occurs. This method was first introduced as a surface analysis method however with current advancements, it can now be used for deeper analysis. Deep hole drilling methods use a drill to produce a deep hole in the specimen. The hole diameter is measured at various depths and then material around the hole is removed through electro-discharge machining (EDM) [22]. After material relaxation occurs caused by EDM the hole diameter is then measured again at the same depths [22]. Using this method can produce strain values at large depths on par with the contour method however the spatial resolution for the deep hole drilling method is around 10mm [7]. As the elastic strain is the recorded measurement, the stresses can also be resolved using Hooke's law.

The contour method was first introduced by Prime [23] in 2001. This method uses

Bueckner's superposition principle [24] which states that when a sample is split and the material begins to deform due to relaxation, if the deformations are reversed to their original positions then the original strain within the sample will be present. Therefore, this method splits a sample of material at a desired location and measures the resultant material relaxation typically using a coordinate measurement machine [25]. The measured displacements are then used as boundary conditions in an FE model in order to recreate the original residual strain. The results from the FE model are then used as the initial residual strains which allows for extremely large penetration depths up to 1m [7] as well as good spatial resolution where the limiting factors are accuracy of the measurement tools and the smallest achievable size of the elements in the FE model. The main disadvantage to this method is that due to the required use of FE software, it can be cumbersome to achieve accurate results because the correct material model and parameters are difficult to accurately determine.

As seen with the previous destructive techniques the samples material relaxation is recorded and translated to stress and strain. This is the typical requirement for destructive techniques however one method first introduced by Guiberteau et al. [1] called the bonded-interface technique (BIT) does not measure relaxation. BIT uses a pre-sectioned sample of material and has been used in research for examining internal residual damage especially for brittle materials [26, 27, 28]. This method uses two square samples of material that are polished and bonded together using cyanoacrylate. An indentation is performed along the split interface after which the cyanoacrylate is chemically removed. The result allows for a direct observation of the internal residual deformation. This method has been utilized in research for many years as the bond layer was assumed to be negligible in terms of the material response [2]. This has since been disproven by Helbawi et al. [2] who discovered that for brittle materials such as ceramics the bond layer violates the primary assumptions of an axisymmetric, continuous, and homogeneous material continuum [2]. Helbawi et al. [2] found that regardless of bond layer thickness, discrepancies remained between FE and experimental results. Therefore, the main cause of discrepancy was determined to be the bond layer itself. These findings do not mean that BIT or other sectioning analysis methods cannot be useful, it just means that the findings from these methods must account for the interface.

Almotairi [3] began using a modified BIT method which used a circular grid analysis technique commonly found in sheet metal fabrication [4] on the internal surface of a non-bonded specimen. Almotairi demonstrated that this modification could be used to resolve principal major and minor residual internal strain by measuring the plastic deformation of the circles from an applied force. Although Almotairi used this modified BIT method, no examination was completed regarding the effect of the split interface as well as no comparison of the residual principal strain results to any other analysis method. This is necessary because free surfaces will be present at the interface without the bond layer applied. These free surfaces are known to attract dislocation movement resulting in a reduced resistance to deformation [29]. Due to this reduced deformation, a sample with a split interface is thought to be an inaccurate representation of a whole sample, however, this has yet to be experimentally tested. This work aims to use an FE model to examine the effect of the split interface as well as to compare to the experimental NBIT. With this novel NBIT, free surfaces will remain however the present work will show the experimental verification of the split interface as well as the computational model being verified by the quantitative experimental data to achieve an increase in confidence for this method. NBIT can be used in future research when residual micro or macro scale strain measurements are of importance with a highly adjustable spatial resolution to be determined by the researcher and available equipment.

2.2 Indentation Theory

2.2.1 Elasticity

There have been many developments in terms of elastic deformation theory, however the concepts derived by Heinrich Hertz in 1881 [30] are still one of the main elastic analysis methods in use to this day. Hertz presented the formulation for purely elastic contact between two circular bodies each with their own radii and material properties. To produce these formulations, Hertz [30] made various boundary conditions such as

- The displacements and stresses between two contacting surfaces must satisfy the differential equations of equilibrium of elastic bodies, and that the stresses must vanish at a great distance from the contact surface
- The tangential components of stress must vanish on both the surfaces
- The normal component of the force must vanish outside the contact surface; but inside the contact surface, the force and counterforce are equal
- The distance between the two surfaces must vanish in the circle of contact, and be greater than zero outside of it

The overall boundary condition for displacements (u_z) within the contact area that were found to satisfy these conditions is written as

$$u_{z1} + u_{z2} = \delta - \left(\frac{1}{2R^*}\right) r^2 \tag{2.2}$$

where r is radial distance from center of contact, δ is the distance of mutual approach or occasionally termed the load point displacement, and R^* is the relative curvature between two spherical contacting bodies found by

$$\frac{1}{R^*} = \frac{1}{R_1} + \frac{1}{R_2} \tag{2.3}$$

where R_1 and R_2 are the radii of the two contacting bodies. A schematic depicting the variables for the case of a sphere contacting a flat plate ($R_2 = \infty$) is shown in Figure 2.2.

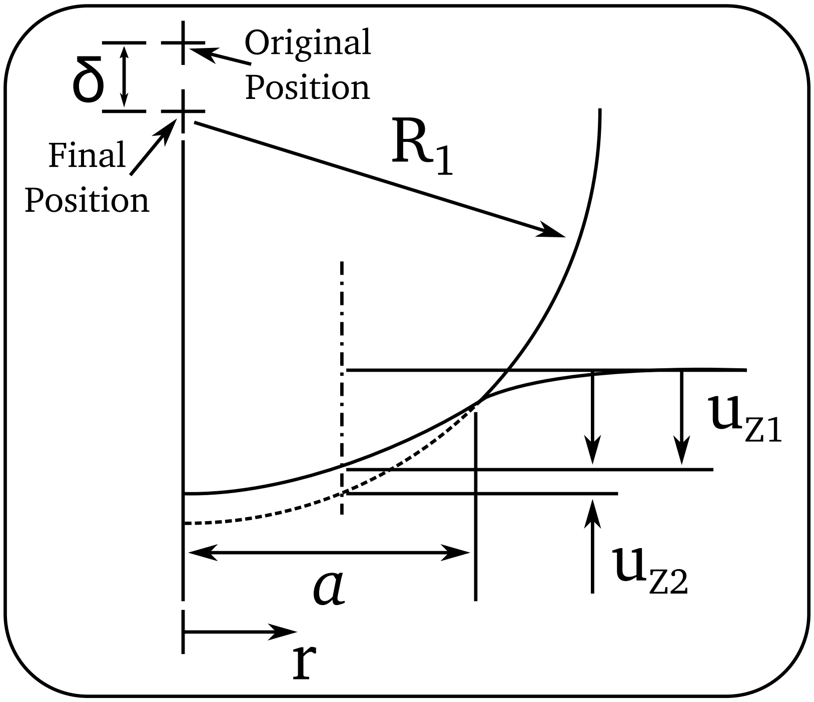

Figure 2.2: Schematic of Hertzian contact between a sphere and a flat plate [31]

This figure shows one of the important features of the Hertzian theory. If one of the spherical bodies in contact is said to have an infinite radius, then it can be analyzed such as if it were an infinitely long flat plate. This is useful as it can be used for directly analyzing the elastic deformations from an indentation test. To increase clarity in the coming definitions, properties related to the spherical indenter or substrate will be denoted with subscripts *i* or *s* respectively. The load point displacement seen in Equation 2.2 is also an important feature to the Hertzian contact theory as it is used for defining the displacement of the indenter which is defined as

$$\delta = \frac{3P}{4aE^*} \tag{2.4}$$

where P is the applied force, a is the contact radius found through

$$a^3 = \frac{3PR^*}{4E^*} \tag{2.5}$$

and E^* is the equivalent elastic modulus given by

$$\frac{1}{E^*} = \frac{1-\nu_i^2}{E_i} + \frac{1-\nu_s^2}{E_s} \tag{2.6}$$

As shown in Figure 2.3, Hertz [30] also found that for the case of a sphere on a flat plate, the normal pressure distribution directly beneath the spherical indenter that would satisfy Equation 2.2 can be written (for $r \leq a$) as

$$p_r = \frac{3P}{2\pi a^2}\sqrt{1-\frac{r^2}{a^2}} \tag{2.7}$$

Other related equations of interest are typically the indentation force as a function of contact radius produced by rearranging Equation 2.5 shown as

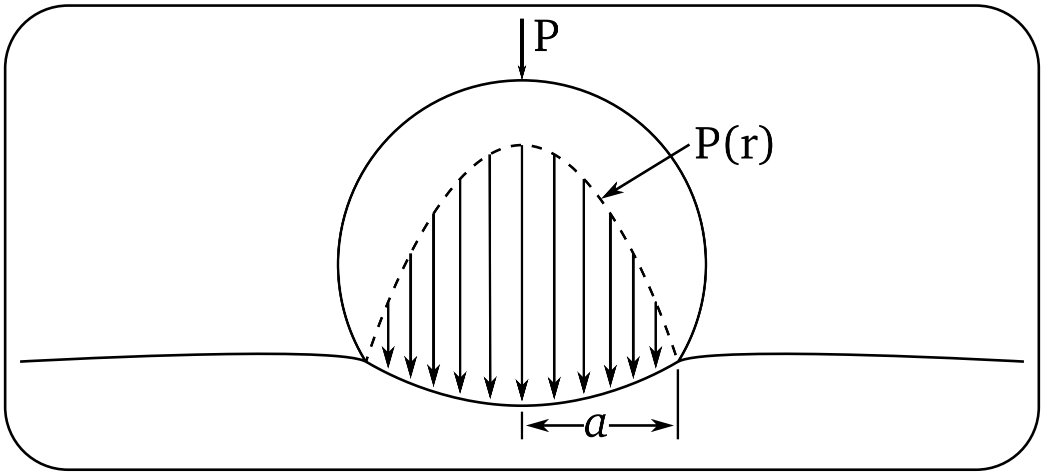

Figure 2.3: Indentation example showing the parabolic pressure curve caused by an applied force

$$P = \frac{4E^*a^3}{3R^*} \tag{2.8}$$

as well as the indentation force as a function of distance of mutual approach produced by rearranging Equation 2.4 for a and substituting into Equation 2.8 to produce

$$P = \frac{4}{3}\sqrt{R^*}E^*\delta^{\frac{3}{2}} \tag{2.9}$$

Hertz also found that the displacements which satisfy Equation 2.7 can be calculated within the contact circle ($r \leq a$) by

$$u_{z(s)} = \frac{1-\nu_s^2}{E_s}\frac{3P}{8a^3}\left(2a^2 - r^2\right) \tag{2.10}$$

as well as outside the contact circle ($r \geq a$) by

$$u_{z(s)} = \frac{1-\nu_s^2}{E_s}\frac{3P}{4\pi a^3}\left[\left(2a^2 - r^2\right)\sin^{-1}\left(\frac{a}{r}\right) + r^2\frac{a}{r}\sqrt{1-\frac{a^2}{r^2}}\right] \tag{2.11}$$

As a force is being applied, the points that lay on the surface of the specimen also move radially as the indenter moves into the specimen. Inside this contact circle ($r \leq a$) the radial displacement can be calculated by

$$u_{r(s)} = \frac{(1-2\nu_s)(1+\nu_s)}{3Es}\frac{a^2}{r}\frac{3}{2}p_m\left[1-\left(1-\frac{r^2}{a^2}\right)^{\frac{3}{2}}\right] \tag{2.12}$$

and the radial displacement outside the circle of contact ($r > a$) which will have the points displacing towards the center of contact by

$$u_{r(s)} = \frac{(1-2\nu_s)(1+\nu_s)}{3E_s}\frac{a^2}{r}\frac{3}{2}p_m \tag{2.13}$$

As the parabolic pressure within the contact is occurring identically between the contacting bodies, the normal displacements for each body found from Equation 2.10 can be substituted into Equation 2.2 to produce

$$\frac{3P}{8a^3E^*}(2a^2-r^2)=\delta-\frac{1}{2R^*}r^2 \tag{2.14}$$

Upon further examination of the contact between an indenter and substrate, the resultant curve that is formed between the contacting surfaces is dependent upon the specific materials used for each body as well as the forces applied. This is because as a force is applied to the indenter, the specimen and indenter will begin to deform. Therefore, the resultant contact curve is a function of the elastic properties of the indenter and specimen as seen from Equation 2.5. Another way to view the Hertzian theory however is to look at the resultant contact curve, and use an indenter radius which would produce that curve as if it were perfectly rigid, as shown in Figure 2.4 denoted by R_{rigid}. This can be utilized for all Hertzian equations such that the relative curvature denoted by R^* simply becomes R_{rigid}. This change also changes the distance of mutual approach where now the distance of mutual approach applies to all points on the indenting body. Therefore, by now assuming a rigid indenter the Hertzian contact radius can be found by using

$$a^3=\frac{3}{4}\frac{P\left(1-\nu_s^2\right)R_{rigid}}{E_s} \tag{2.15}$$

where there is now no material influence from the indenter. Using this method is not ideal for every situation, however for contact scenarios where the ratio R_{rigid}/R_i approaches unity such as a diamond indenting a steel or aluminum substrate, the indenter can be assumed rigid with marginal error.

Aside from the displacements caused by a purely elastic contact, Hertz also began developing the basis for the stresses. These stresses are typically normalized via the mean pressure (P_m) where $P_m=P/(\pi a^2)$. Hertz found that the radial stress on the

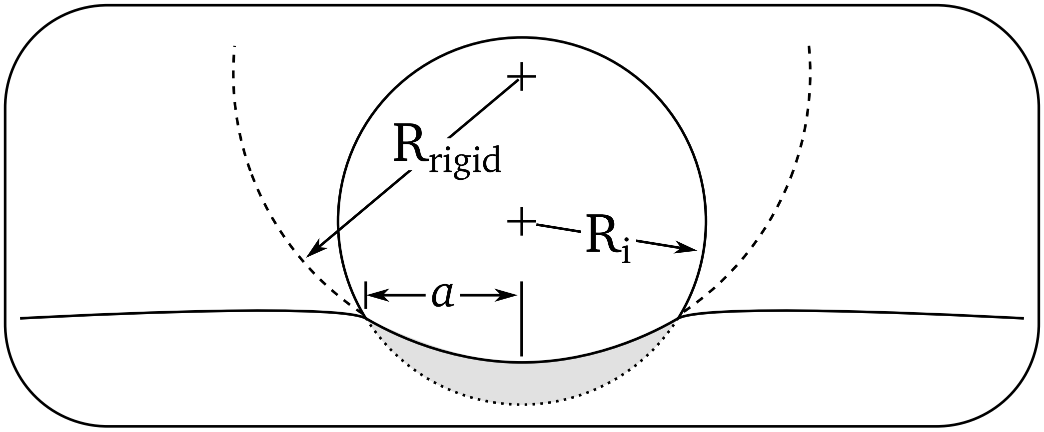

Figure 2.4: Indentation example showing contact radius, initial radius, and rigid radius [31]

surface of the substrate can be defined inside the contact area ($r \leq a$) by

$$\frac{\sigma_r}{p_m} = \frac{1-2\nu_s}{2}\frac{a^2}{r^2}\left[1-\left(\frac{1-r^2}{a^2}\right)^{\frac{3}{2}}\right]-\frac{3}{2}\sqrt{1-\frac{r^2}{a^2}} \tag{2.16}$$

and outside the circle of contact ($r > a$) by

$$\frac{\sigma_r}{p_m} = \frac{1-2\nu_s}{2}\frac{a^2}{r^2} \tag{2.17}$$

The hoop stress on the surface of the specimen is always a principal stress, and outside the circle of contact ($r > a$), the hoop stress is equal in magnitude to the radial stress shown as

$$\sigma_\theta = -\sigma_r \tag{2.18}$$

Within the interior of the specimen, much work has been completed by Huber [32] who derived the internal stresses which can be calculated from

$$\frac{\sigma_r}{p_m} = \frac{3}{2}\frac{1-2\nu_s}{3}\frac{a^2}{r^2}\left[1-\left(\frac{z}{\sqrt{u}}\right)^3\right]+\left(\frac{z}{\sqrt{u}}\right)^3\frac{a^2u}{u^2+a^2z^2} \\ +\frac{z}{\sqrt{u}}\left[u\frac{1-\nu_s}{a^2+u}+(1+\nu_s)\frac{\sqrt{u}}{a}tan^{-1}\left(\frac{a}{\sqrt{u}}\right)-2\right] \tag{2.19}$$

$$\frac{\sigma_\theta}{p_m} = \frac{-3}{2}\frac{1-2\nu_s}{3}\frac{a^2}{r^2}\left[1-\left(\frac{z}{\sqrt{u}}\right)^3\right]+\frac{z}{\sqrt{u}}\left[u\frac{1-\nu_s}{a^2+u} \\ -(1+\nu_s)\frac{\sqrt{u}}{a}tan^{-1}\left(\frac{a}{\sqrt{u}}\right)+2\nu_s\right] \tag{2.20}$$

$$\frac{\sigma_z}{p_m} = \frac{-3}{2}\left(\frac{z}{\sqrt{u}}\right)^3\frac{a^2u}{u^2+a^2z^2} \tag{2.21}$$

$$\frac{\tau_{rz}}{p_m} = \frac{-3}{2}\frac{(rz)^2}{u^2+a^2z^2}\frac{a^2\sqrt{u}}{a^2+u} \tag{2.22}$$

where

$$u = \frac{1}{2}\left[\left(r^2+z^2-a^2\right)+\sqrt{(r^2+z^2-a^2)^2+4a^2z^2}\right] \tag{2.23}$$

Something to note is that for values of $z = 0$ and values of $r/a < 1$, the value of u will be zero, however the value of stress directly below the indenter can be calculated by taking a small value of z. By using Equations 2.19 - 2.22 the principal stresses can be determined through

$$\sigma_{1,3} = \frac{\sigma_r+\sigma_z}{2} \pm \sqrt{\left(\frac{\sigma_r+\sigma_z}{2}\right)^2+\tau_{rz}^2} \tag{2.24}$$

$$\sigma_2 = \sigma_\theta \tag{2.25}$$

$$\tau_{max} = \frac{1}{2}\left[\sigma_1-\sigma_3\right] \tag{2.26}$$

2.2.2 Plasticity

Due to the elastic deformation consisting of the linear section in a stress strain curve, many numerical models were able to be created that could accurately predict the resultant deformation. Once yielding begins to occur, plasticity effects begin and therefore the resultant deformation becomes much more complex. For this reason, there has not been nearly as much advancement towards the number of numerical models for plastic deformation as seen with elastic deformation. The deformations and stress field of an elastic-plastic material will be similar to that of a purely elastic material, however since the material will now undergo permanent plastic deformations, the resultant deformations and stress field will be more dependent upon the elastic modulus and the yield strength of the material. Unlike elastic contact, elastic-plastic contact does not have a unified mathematical model to describe the deformations or stress field caused by an indentation. Currently the main method for viewing an elastic-plastic stress field is by using finite element (FE) analysis which will be discussed further in section 2.3. Albeit not as informative as FE analysis there are three methods that can be used to analyze the elastic-plastic response from an indentation. These are the elastic constraint factor, expanding cavity model, and rigid plastic slip line theory.

Timoshenko [33] has found that for an indentation, there is a maximum stress point below the indented surface where the plastic yield will first occur. This maximum can be seen in Figure 2.5 where the maximum shear stress is seen to occur at a distance below the surface that is equivalent to $0.47a$, where a is the radius of the circle of contact. The value for the stress at this point depends upon the materials Poisson ratio however for common materials such as steel with a Poisson ratio of approximately 0.3, the stress at the maximum point will then be approximately $0.47P_m$ [34]. This max stress can then be related to the yield criterion being $0.5Y$ such that $0.47P_m = 0.5Y$ which can be reduced to $P_m = 1.1Y$ [34].

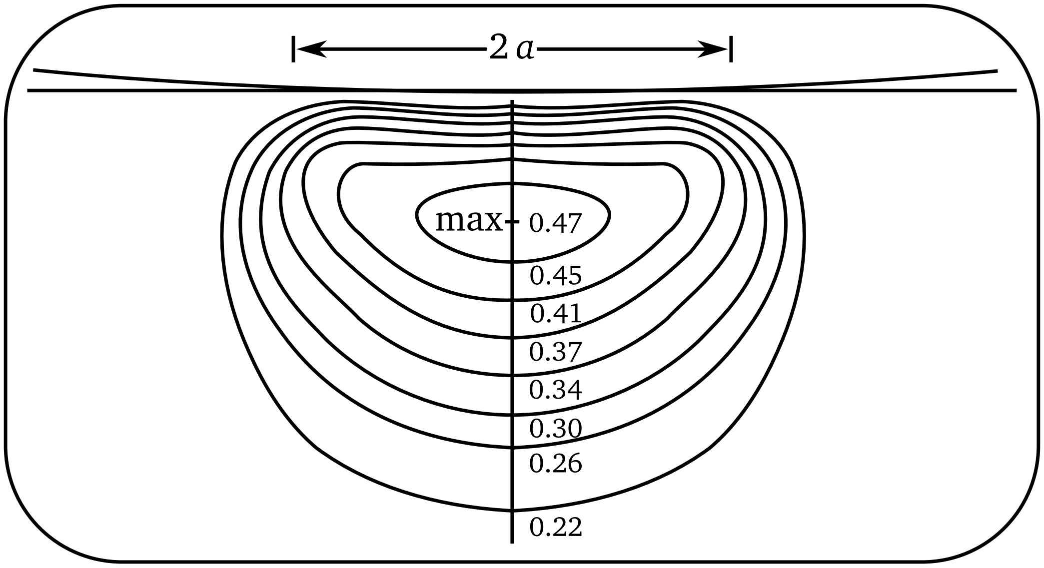

Figure 2.5: Indentation stress field lines as function of indenter radius [35]

If the mean pressure within the material does not exceed $1.1Y$, the material response will be fully elastic. However, once the pressure increases beyond $1.1Y$, plasticity will begin to take effect until a fully plastic response is achieved. This can be seen visually in Figure 2.6 where the line from point O to A represents a fully elastic response, L is when the material begins to yield, the line from L to M is where the material is exhibiting elastic and plastic behavior, and the final line from M to N depicts a fully plastic response where M is the point of full plastic yielding [34]. This figure can be simplified down to $P_m = cY$ where c is the elastic constraint factor first introduced by Tabor [36]. Tabor experimented with several different standard materials such as mild steel, copper, and aluminum, and found that all of these materials began to fully yield when $c \approx 3.0$.

The reason in Figure 2.6 that the mean pressure eventually stops increasing between points M and N with increasing load is because of the fully plastic response. Underneath the indenter when the area is fully plastic, increasing the indenter load advances the plastic zone further into the elastic zone. This sort of plasticity zone movement can be described more accurately by analyzing the expanding cavity model.

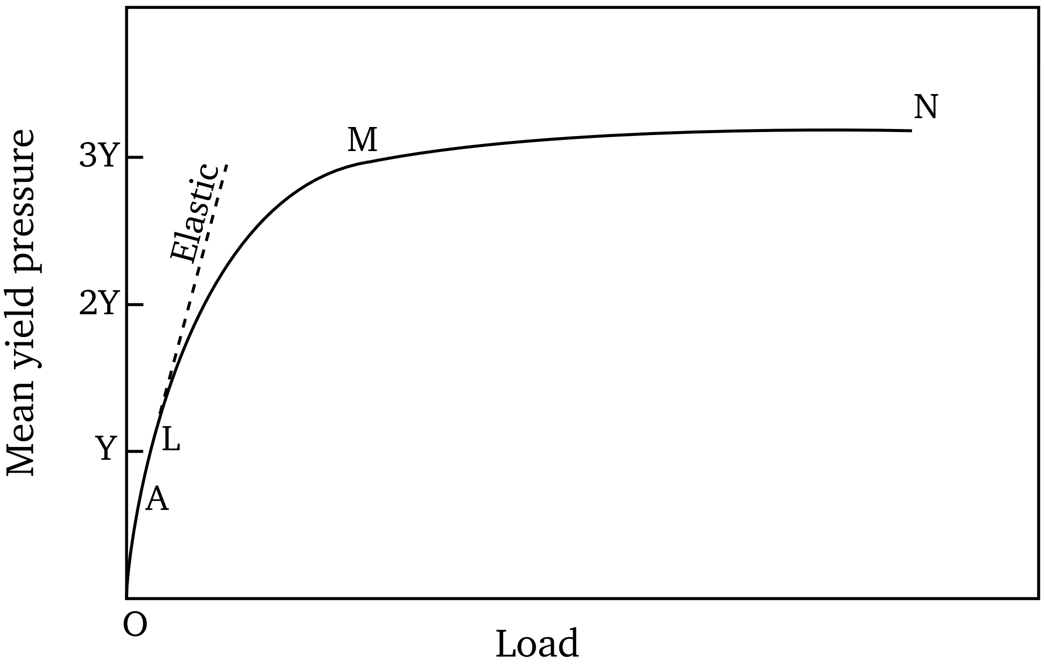

Figure 2.6: Load curve of a plastic material deformed via a spherical indenter [34]

The expanding cavity model utilizes the initial observations from Samuels and Mulhearn [37] and Mulhearn [38] who found that the internal displacements that occur due to material flow underneath a blunt indenter are approximately radial from the point at which the indenter first contacts the sample as shown in Figure 2.7.

Since the displacements are radial away from the indenter, this can be used for the expanding cavity model which has been developed by Johnson [39] who used the initial developments from Hill [40] and Marsh [41]. This method assumes that directly below the indenter there is a hemispherical core of material applying a hydrostatic pressure onto the inside surface of the outer elastic region [39]. Past this region, the stresses and displacements are assumed to have radial symmetry and therefore are the same as an infinite elastic perfectly-plastic solid which contains a spherical cavity under pressure [42]. As seen in Figure 2.8, the expanding cavity has a radius of r_c, where r_c must be greater than the radius of the initial core of material, and has an incompressible plastic zone. The reason that the plastic zone is assumed to be incompressible is so that for

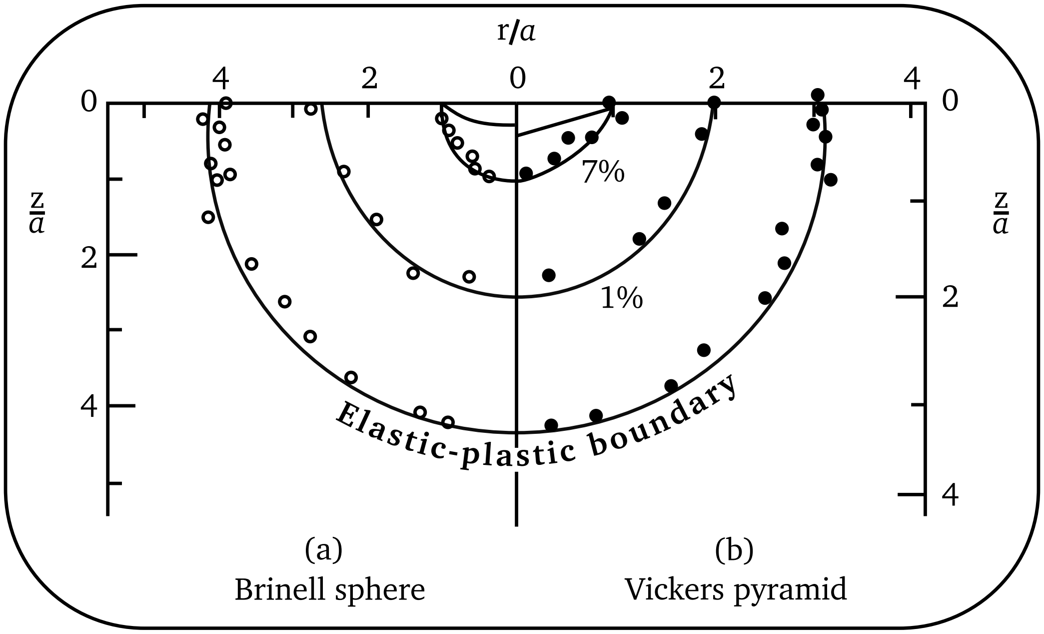

Figure 2.7: Results from Samuels and Mulhearn [37] showing hemispherical strain contours for Brinell (a) and Vickers (b) indentation

analysis, it can be said that during an indentation increment where the indenter moves a distance dh into the sample, the volume of the material displaced must be equal to the displacement of particles at the elastic-plastic boundary [42]. By using this principal, Hill [40] was able to develop equations for the stress within the plastic and elastic zones during an indentation. More importantly there is also an equation found where the pressure of the hydrostatic core caused by a spherical indenter as seen in Figure 2.8 can be described by

$$\frac{\bar{P}}{Y} = \frac{2}{3}\left[1 + \ln\left(\left(\frac{E}{Y}\frac{1}{2}\frac{a}{R} + 4(1-2\nu)\right)\frac{1}{6(1-\nu)}\right)\right] \tag{2.27}$$

Another method which can be used for plasticity analysis is the rigid plastic slip line theory which is typically used for analyzing machining, however it is also useful for indentation analysis [44]. This theory can be used to help relate the yield strength of a

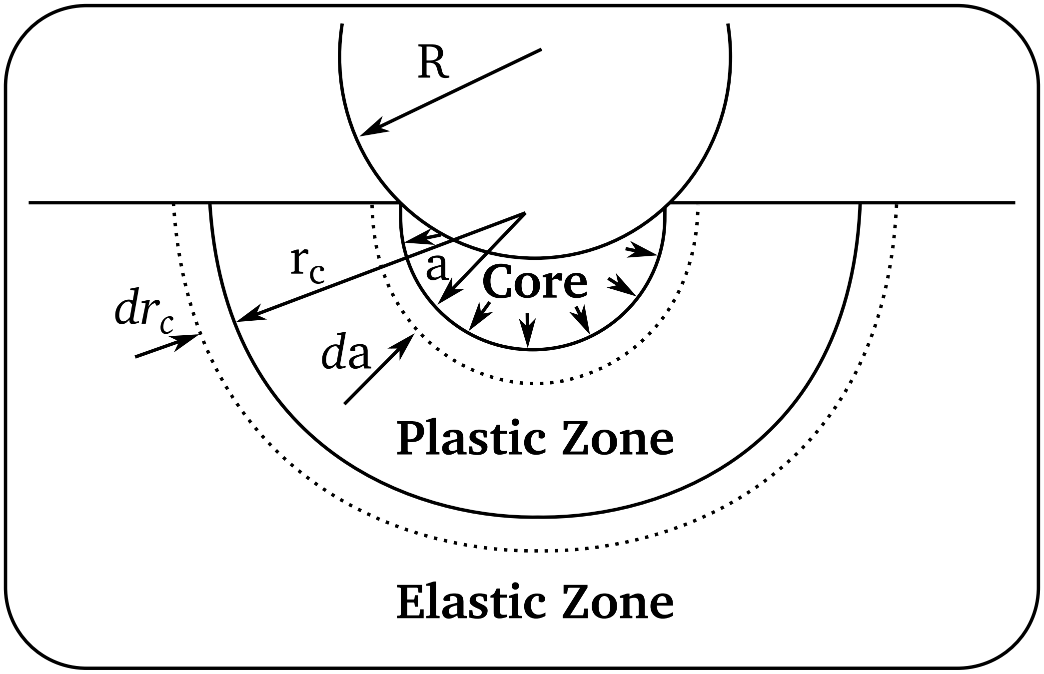

Figure 2.8: Expanding cavity schematic from a spherical indenter [43]

material and average pressure caused by contact from a rigid indenter to the magnitude of deformation occurring [45]. The slip lines as seen from lines BFC and DFH in Figure 2.9 represent the lines of maximum shear stress and intersect with the free surface at 45° and with each other at 90° [44]. These slip lines also intersect with the indenter at angle γ which is defined by

$$\gamma = \frac{1}{2}\cos^{-1}\frac{\mu\sigma_n}{k} \tag{2.28}$$

where $\mu\sigma_n$ is the tangential frictional stress, and k is the shear flow stress [44].

In the current research, this method has been compared to simulations ran using the FE method, and the results as reported by Jackson [45] are fairly similar. This theory however, is based upon the assumptions that the applied load is quasi-static, no body forces are being applied, the von Mises yield criterion is the method to which the material yields, the material is perfectly plastic, and friction is considered negligible [45].

As developed by Hill et.al. [47] the amount of material that is displaced by the indenter

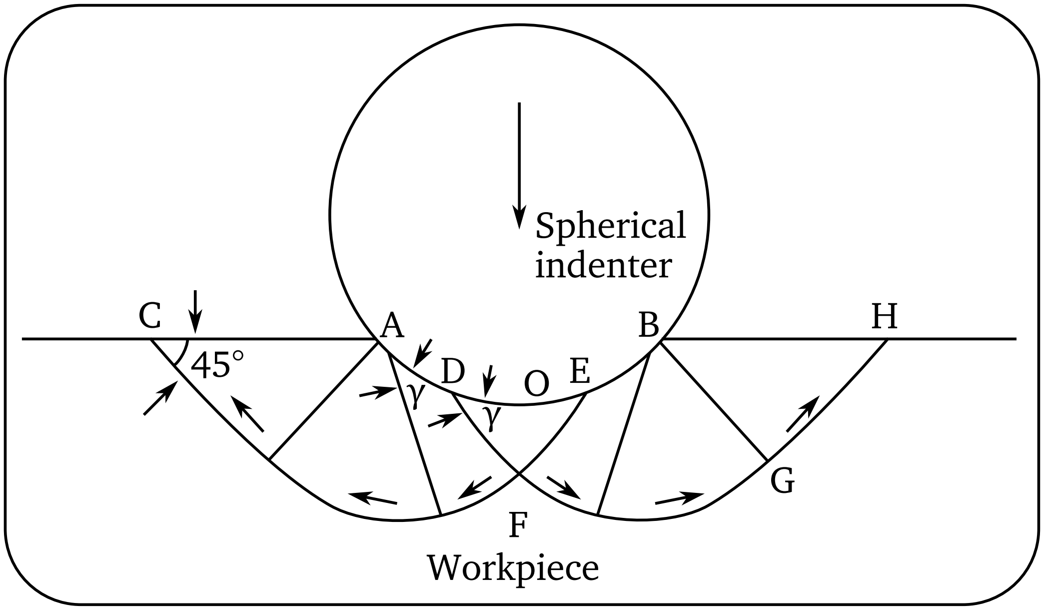

Figure 2.9: Rigid slip lines from a pyramidal indenter showing maximum shear stress lines [46]

is accounted for by upward flow shown by the arrows in Figure 2.9. As this theory utilizes the idea that shear stress is the main cause for plastic deformation, the slip lines can be used to represent the possible plastic flow. By using this theory, the pressure caused by the indenter can be found by

$$\frac{\bar{P}}{S_y}=\frac{4}{3\sqrt{3}}\left(\frac{a}{r}\right)^{-2}\left[\frac{1}{3}\left(\frac{a}{r}\right)^{3}-\left(1+\cos^{-1}\left(\frac{a}{r}\right)\right)\left(1-\left(\frac{a}{r}\right)^{2}\right)^{\frac{3}{2}})-\frac{a}{R}+\frac{\pi}{2}+1\right] \tag{2.29}$$

which similar to the expanding cavity model, can be used to relate to the mean contact pressure which can then also be used to determine hardness. It should also be noted that since this method assumes shear stress is the mode of failure, the pressure seen in Equation 2.29 is normalized by the materials maximum shear stress, whereas the expanding cavity model normalizes the pressure by the materials yield strength.

2.3 Finite Element Theory

The use of numerical simulations to predict physical phenomenon have been of continued interest since the evolution of computational systems. Finite element (FE) modeling is one such numerical simulation technique which uses the discretization of a finite number of elements where their respective corresponding constitutive equations are solved to produce an approximation of a real-world phenomenon. This description of approximation should not be understated as the mathematical models that represent these natural phenomenon are idealized representations and should not be misinterpreted with physical reality [48]. It is for this reason that FE results cannot be directly accepted, without validation. The typical validation and verification process for a solid-mechanics analysis is illustrated in Figure 2.10, where the verification process separated via the dashed outline is a large part of the overall validation process.

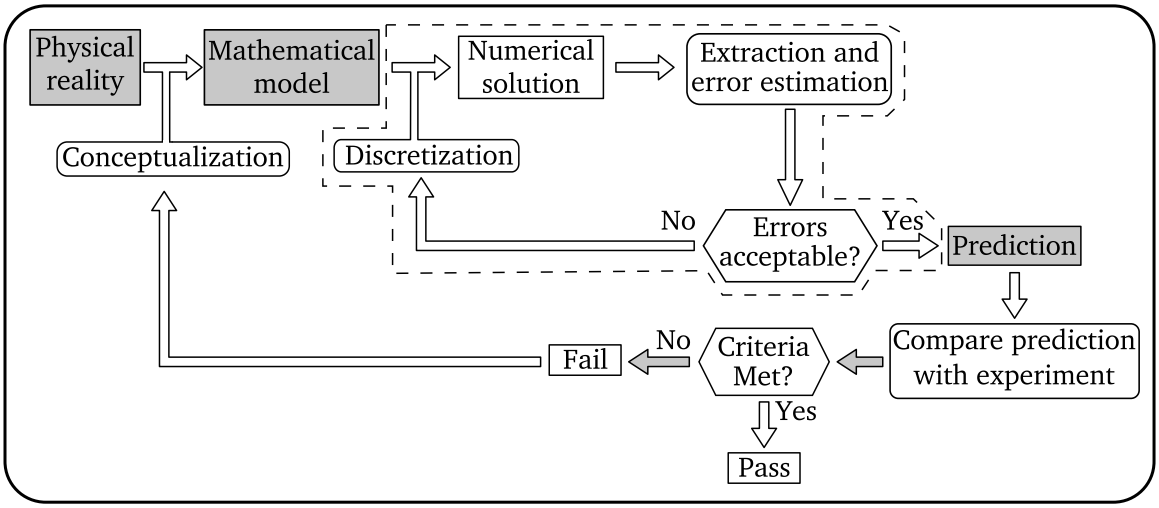

Figure 2.10: Validation process for FE analysis with verification process in dashed section [48]

The purpose of a verification process is to determine if the computed data is within acceptable error levels [48]. An example of verification would be much like a mesh convergence study. This is where element sizes are decreased until the resultant data of interest converges onto a solution. If the data of interest which could range from the measured displacement of a single node to the maximum stress within a specific element is within the acceptable error than the element size which produced those results is accepted. This verification process is a single part of the entire validation process and is focused more on the solution of the mathematical model than the physical reality it is representing [48]. The validation process is where the mathematical models are compared to physical experiments. Therefore, for an ideal FE model, physical experiments must be done in order for the validation and verification to be successfully completed.

For this work, FE analysis has played a large role for analyzing the physical phenomenon of indentation for measuring residual strain. Therefore, this section will discuss the basic theory behind FE analysis. Section 2.3.1 discusses the linear analysis method and how the stiffness matrix is formed. Section 2.3.2 discusses non-linear analysis along with the explicit and implicit time integration methods. Section 2.3.3 discusses mesh formulations. Section 2.3.4 discusses various material models along with their differences. Section 2.3.5 discusses the various contact algorithms available with the LS-DYNA hydrocode, while section 2.3.6 discusses the effects of friction on FE indentation results.

Two major software packages used for the FE analysis are Altair HyperWorks and LSTC LS-DYNA. Altair HyperWorks has a more user-friendly interface along with more helpful online forums than compared to LS-DYNA. This allows HyperWorks to be the optimal choice for problem set-up, meshing, and results analysis. This also leads HyperWorks to be highly useful for linear simulations however for the more complex phenomenon, LS-DYNA is the better choice as it is one of the leading simulation packages for non-linear analysis used in industry. For these reasons discussed HyperWorks was used in this work for basic problem set-up as well as mesh generation and result analysis while LS-DYNA was used for its industry leading non-linear solver. It should be noted that the entirety of this work was completed using the ls-dyna_smp_d_R901_winx64_ifort131 solver.

2.3.1 Linear Analysis

A linear analysis begins by the discretization of the problem into a set of nodes and elements. For modern FE analysis there are many different element types such as 1-dimensional bar, 2-dimensional triangular, and quadrilateral elements, or 3-dimensional tetrahedral, pentahedral, and hexahedral elements. As an element is simply the shape that forms with a specific set of nodal connections, any given node is likely to be connected to multiple elements. To maintain the elemental type as well as relation to other elements, all nodes are defined in both the elemental local coordinate system, and the models global coordinate system. Upon completion of the FE analysis the nodal displacement results will be the primarily determined outcome however in order to determine the results between individual nodes, a nodal shape function is used as an interpolation method. Shape functions come in various forms such as linear, quadratic, or cubic and also varies depending upon the type of element chosen. Regardless of the element type and interpolation method, the element is transformed into a normalized coordinate system with axes denoted by ξ, ζ, and η where the center of the element is at a position of (0,0,0) and the furthest points of the element are at a value of -1 or +1 with an example shown in Figure 2.11. This drastically simplifies the FE solution as the shape functions will remain constant for a given element type and interpolation method making it an efficient computational process. Therefore, when the solver computes the Jacobian matrix, the interpolated results within the original Cartesian coordinate system can be directly translated by using the shape functions normalized coordinate system. Once the shape functions are determined the stiffness matrix can then be computed.

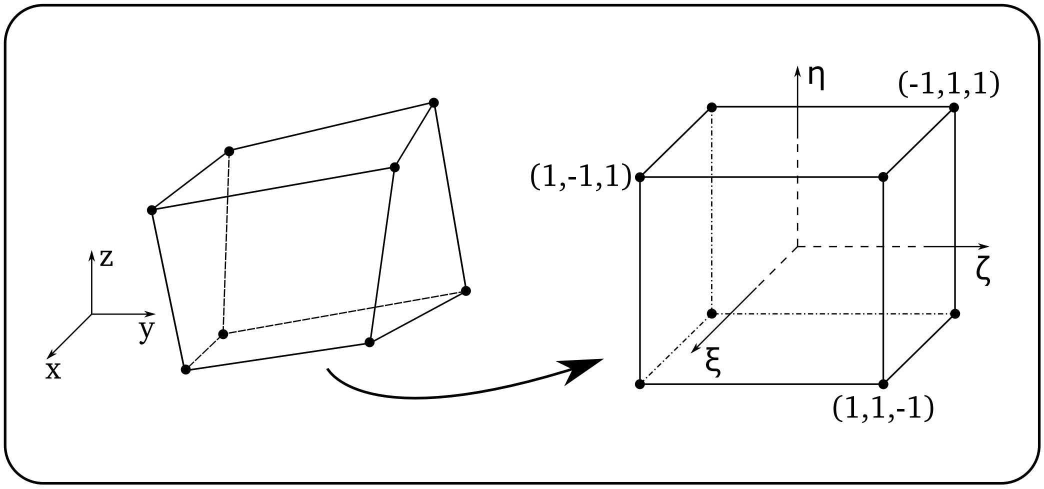

Figure 2.11: Transformation from Cartesian to normalized coordinate system

For a single element, the forces (q) and displacements (a) acting on its nodes can be arranged in the forms of

$$[q^e] = \begin{pmatrix} q_1^e \\ q_2^e \\ \vdots \\ q_n^e \end{pmatrix} \quad \text{and} \quad [a^e] = \begin{pmatrix} a_1^e \\ a_2^e \\ \vdots \\ a_n^e \end{pmatrix} \tag{2.30}$$

where e is the element identifier and n is the number of nodes within the element [49]. These forces and displacements are then related through

$$q^e = k^e a^e + f_p^e + f_{\epsilon_0}^e \tag{2.31}$$

where k^e is the elemental stiffness, f_p^e is the elemental force required to balance a distributed loading, and $f_{\epsilon 0}^e$ is the elemental force required to balance initial strains. As q^e and a^e contain the same number of components or degrees of freedom [49], the stiffness matrix will always be a square matrix in the form of

$$[k^e] = \begin{pmatrix} k_{ii}^e & k_{ij}^e & \cdots & k_{im}^e \\ \vdots & \vdots & \ddots & \vdots \\ k_{mi}^e & k_{mj}^e & \cdots & k_{mm}^e \end{pmatrix} \tag{2.32}$$

Once the stiffness matrix for each element is computed, the global stiffness matrix is assembled which sums all of the elemental stiffness matrices together to form a stiffness value for each node. The FE solver will then apply the boundary conditions to the global stiffness matrix which will adjust specific nodal stiffness values. With a complete global stiffness matrix, the linear solver then computes the nodal displacements of each and every node. From this resultant displacement data, the stresses within an element can be determined by

$$[\sigma^e] = [D][B][a^e] \tag{2.33}$$

where $[D]$ is the materials elasticity matrix and $[B]$ is the interpolation matrix found through the use of the shape function.

2.3.2 Non-Linear Analysis

Non-linear analysis as an FE method is used for more complex problems and therefore is more difficult to set-up, but if done correctly will typically yield better results than a purely linear solution. The downside to this non-linear method is that it increases the amount of computational power required which also increases the amount of time required to complete an analysis. Therefore, a linear solution should be used if the scenario is applicable as it will use less resources therefore requiring less time. There are however, several different aspects that can justify when it is appropriate and necessary to use a non-linear analysis. The four main scenarios are if an analysis is going to undergo material non-linearity, geometric non-linearity, force non-linearity, or a contact non-linearity [50].

These scenarios arise due to the relations between the boundary conditions, displacements, stresses, and strains. A material non-linearity will arise when the relation between the stress and strain becomes non-linear such as during plastic deformation. Geometrical non-linearity will arise when the relation between the displacements and strain becomes non-linear such as with sufficiently large deformations of a mesh. The force and contact non-linearities come from boundary conditions that effect the stresses and displacements respectively in a non-linear fashion. These occur because the contact condition changes the displacements based on the deformations of the mesh, and the force condition changes with the deformations which affect the stress. All of these scenarios cause the stiffness matrix to change from being constant, to being dependent upon the strain and displacements [51].

For an analysis which exhibits any of the non-linearities discussed, there are currently two different methods that a solver will use to complete the analysis. These methods are an explicit or implicit time integration. Both methods use incremental solutions to determine how the stiffness matrix updates based on the non-linearities and then uses the updated matrix to perform the subsequent iteration. There are some significant differences however which cause the explicit method to be used for wave propagation or high velocity impact problems, and cause the implicit method to be used for structural analysis, or more generally any analysis which exhibits low frequency responses [52].

Time Integration

The time integration methods used in modern FE analysis are based upon the classic Newmark integration method. For the sake of simplicity and increased clarity within this section, the following explanations will solely lie on the nodal displacements. For Newmark integration, a mass matrix $\boldsymbol{M}$ and dampening matrix $\boldsymbol{C}$ are assumed to be given and utilized to determine the dynamic equilibrium at the end of step state through the formulation [52]

$$\bar{g}_{n+1} = \{q_{i,n+1} - q_{e,n+1}\} + \boldsymbol{M}\ddot{d}_{n+1} + \boldsymbol{C}\dot{d}_{n+1} = g_{n+1} + \boldsymbol{M}\ddot{d}_{n+1} + \boldsymbol{C}\dot{d}_{n+1} = 0 \tag{2.34}$$

where $\bar{g}_{n+1}$ and g_{n+1} are the dynamic and static out of balance forces respectively, and $q_{i,n+1}$ and $q_{e,n+1}$ are the static internal and external forces respectively. The Newmark time integration also utilizes the formulations

$$d_{n+1} = d_n + \Delta t \dot{d}_n + \frac{\Delta t^2}{2}\{(1-2\beta)\ddot{d}_n + 2\beta \ddot{d}_{n+1}\} \tag{2.35}$$

$$\dot{d}_{n+1} = \dot{d}_n + \Delta t\{(1-\gamma)\ddot{d}_n + \gamma \ddot{d}_{n+1}\} \tag{2.36}$$

where γ and β are Newmark constants that define whether the integration will be either implicit or explicit.

The implicit method relies on the trapezoidal rule which uses $\gamma = 1/2$ and $\beta = 1/4$ to obtain

$$d_{n+1} = d_n + \Delta t \dot{d}_n + \frac{\Delta t^2}{4}\{\ddot{d}_n + \ddot{d}_{n+1}\} \tag{2.37}$$

$$\dot{d}_{n+1} = \dot{d}_n + \frac{\Delta t}{2}\{\ddot{d}_n + \ddot{d}_{n+1}\} \tag{2.38}$$

which can be combined to produce

$$d_{n+1} = d_n + \frac{\Delta t}{2}\{\dot{d}_n + \dot{d}_{n+1}\} \tag{2.39}$$

From here, Equations 2.38 and 2.39 can be combined with Equation 2.34 to form

$$\bar{g}_{n+1}(d_{n+1}) = \bar{g}_{n+1}(q_{i,n+1}(d_{n+1}), d_{n+1}) = 0 \tag{2.40}$$

This equation is solved for implicit analysis through a prediction and Newton-Raphson correction step which results in a solution of

$$\Delta d_{n+1} = -\bar{\boldsymbol{K}}_{t,n+1}^{-1} \cdot \bar{g}_{n+1} \tag{2.41}$$

where $\bar{\boldsymbol{K}}$ is the dynamic tangential stiffness matrix which also contains the effects of the mass and dampening matrix.

The explicit method however uses Newmark constant values of $\gamma = 1/2$ and $\beta = 0$ to obtain

$$d_{n+1} = d_n + \Delta t \dot{d}_n + \frac{\Delta t^2}{2} \ddot{d}_n \tag{2.42}$$

$$\dot{d}_{n+1} = \dot{d}_n + \frac{\Delta t}{2} \{(1-\gamma)\ddot{d}_n + \gamma \ddot{d}_{n+1}\} \tag{2.43}$$

where Equation 2.43 can be substituted into Equation 2.34 and solved to produce

$$\ddot{d}_{n+1} = -\boldsymbol{M}^{-1}(g_{n+1} + \boldsymbol{C}\dot{d}_n) \tag{2.44}$$

Therefore, at the end of the timestep, Equations 2.44, 2.43, and 2.42 will produce $\ddot{d}_{n+1}$, $\dot{d}_{n+1}$, and d_{n+1} respectively. As the explicit time integration utilizes the mass matrix which has the potential to be diagonalized, but is also generally smaller than the stiffness matrix used in the implicit time integration, the inversion of the mass matrix is significantly easier comparatively. Therefore, for a given timestep, the amount of computational resources will be reduced by using the explicit method.

The main issue with the explicit method however is that it is prone to run away errors and therefore, to combat this issue, a significantly smaller timestep is required compared to the implicit method. This small timestep is why the explicit method is useful when analyzing high velocity impacts or wave propagations however for lower frequency analysis, the implicit method is generally the chosen time integration method.

2.3.3 Mesh Formulations

As described by Anderson et.al [53] there are two different mesh formulations that use the material reference and spatial reference and are the Lagrangian and Eulerian formulations respectively. These two mesh formulations use different approaches for solving the deformations of the FE continuum. These methods have been heavily described in literature by Benson [54] however a brief overview of their distinct differences will follow.

The Lagrangian formulation is known as the material reference as this method ties the defined material to the mesh itself [55]. Therefore, as deformations occur both the material and the mesh deform together which can be seen in Figure 2.12. This Lagrangian formulation has also been defined by Zhangxin [56] as an element whose degrees of freedom are all given via function values. This means that for a given displacement the mesh and material move together however while equilibrium iterations are performed, the mesh and material are fixed in place [52]. This has its strengths as it is computationally less intensive than the Eulerian formulation, but if the deformations become too intense, numerical instabilities can occur due to the degraded quality of the mesh and the solver can fail or become stuck in a convergence loop. This degraded mesh quality can be fixed as programs such as LS-DYNA have capabilities to perform adaptive re-meshing once the mesh becomes too deformed. Adaptive re-meshing is highly resource intensive, however there is also a niche area where a user may create a pre-deformed mesh that upon further deformation improves the mesh quality. The alternative to these mesh improvement methods would be the use of the Eulerian formulation or potentially the Arbitrary Lagrangian Eulerian (ALE) formulation.

The Eulerian formulation is known as the spatial reference and is where the material and mesh are not directly tied to each other, and the material moves through the mesh as it is deformed [57]. This can be seen schematically in Figure 2.13. For this reason the Eulerian mesh is capable of simulating large deformations without the risk of mesh quality degrading and is also capable of simulating natural free surface creation [54]. For these reasons, the Eulerian formulation is used mostly for fluid dynamics, and in other situations where large deformations occur such as deep indentations, some metal forming processes, and scratch tests to name a few.

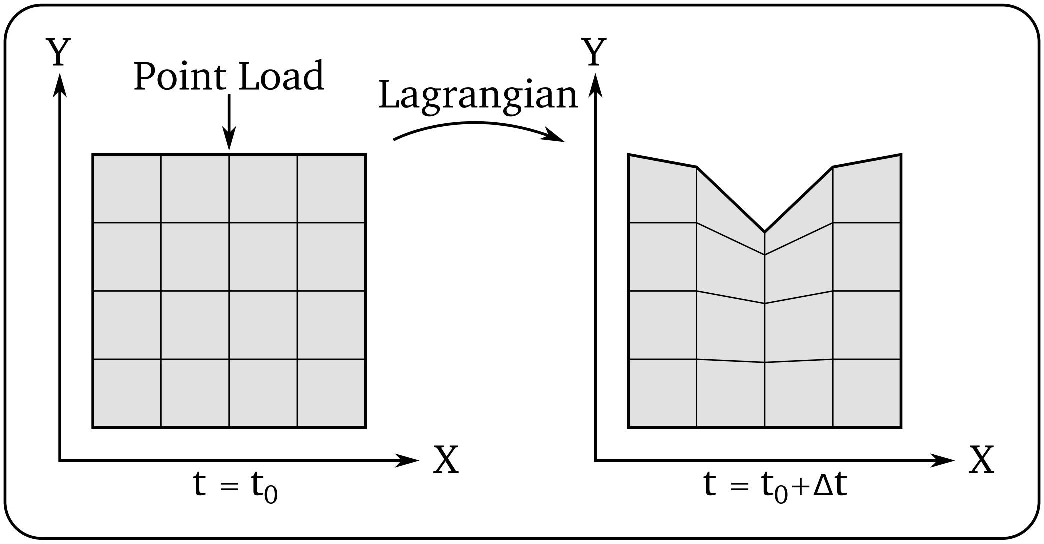

Figure 2.12: Lagrangian mesh formulation showing before (left) and after (right) deformation

The ALE formulation is fairly complex however a basic description is that it uses the positives from both the Eulerian and Lagrangian formulation by using the spatially free aspect of the Eulerian formulation and the time-step of the Lagrangian [54]. Once the Lagrangian time-step is successfully completed, this formulation uses an adaptive re-meshing technique which is used to associate the deformed Lagrangian mesh to the spatially free Eulerian Mesh [54]. Another method that combines Eulerian and Lagrangian formulations was completed by Anderson [53] who performed indentation testing on a workpiece and used the Hybrid Eulerian-Lagrangian formulation. This method is where the area of interest under the indenter is using the Eulerian formulation,

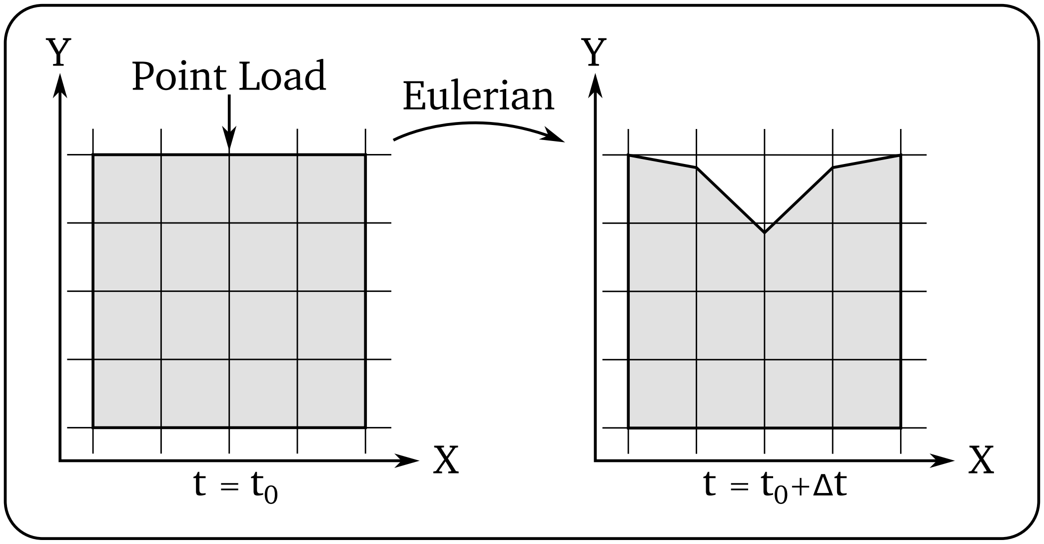

Figure 2.13: Eulerian mesh formulation showing before (left) and after (right) deformation

and the remaining area is using the Lagrangian formulation. According to Anderson, by using this hybrid method, the model does not require adaptive re-meshing to transfer the deformations and improves the simulation time by around 50% compared to a purely Eulerian formulation.

2.3.4 Material Models

When running a simulation using a FE analysis, the material model chosen can have a significant impact on the results. Therefore, careful consideration must be taken to ensure that the chosen material model is an accurate representation of the material that is going to be used in the desired application. The most basic material model is a purely elastic model, which can be used for scenarios where the elastic limit of the material will not be approached, and where strain-rate, thermal effects, and equation-of-state are not required. As the material models become more complex for simulations that require plasticity to be accounted for, there are many different models available however the power-law, and Johnson-Cook models are two of the most commonly used material models for elastic-plastic materials. LS-DYNA specifically has over 200 different material models which is continually increasing as newer models are developed.

The power-law is a highly utilized material model as it can be used to simulate isotropic plasticity with strain-rate effects by using a power-law hardening rule. This power-law model can simulate the effective stress σ_y through

$$\sigma_y = k\epsilon^n = k\left(\epsilon_{yp} + \bar{\epsilon}_p\right)^n \tag{2.45}$$

where ϵ_{yp} is the elastic strain needed to yield the material, $\bar{\epsilon}_p$ is the effective plastic strain, k is a strength component, and n is a hardening component. The disadvantage to this model is that it cannot consider thermal effects, failure effects, or equation-of-state effects if they are required.

The Johnson-Cook material model was developed by Gordon Johnson and William Cook in 1983 [58] and is used when strain-rate, thermal effects, equation-of-state, and failure effects are required. This method is more computationally intensive however if the required effects are needed then this is the better model. The Johnson-Cook material model defines effective stress as:

$$\sigma_y = \left(A + B\bar{\epsilon}_p^n\right)(1 + C\ln\dot{\epsilon}^*)\left(1 - \left(\frac{T - T_0}{T_m - T_0}\right)^m\right) \tag{2.46}$$

where A is the yield stress, B and n are strain hardening coefficients, C is the strain rate constant, $\dot{\epsilon}^*$ is the effective plastic strain rate, and m is for representing thermal softening [58]. These constants are defined by the user which are obtained via experiments, with many values of commonly used materials already tabulated by Johnson and Cook [58]. This model has been heavily used and proven in literature, especially for use in indentation testing on elastic-plastic materials such as Anderson et.al [53] who used a diamond indenter on a steel workpiece for deep indentations, Doman et.al. [59] who used a ceramic indenter on a steel workpiece for shallow indentations, Wang et.al [60] who used a tungsten carbide indenter on a Ti-6Al-4V sample, and many more.

If the Johnson-Cook model is the best option to use for a certain scenario, but thermal, equation of state, and failure effects are not required then there is also a simplified Johnson-Cook model which is simply defined as

$$\sigma_y = \left(A + B\bar{\epsilon}_p^n\right)(1 + C \ln \dot{\epsilon}^*) \tag{2.47}$$

Utilizing this material model will reduce computational requirements by 50% compared to the full Johnson-Cook model [61], but is still more computationally intensive than the power-law material model.

2.3.5 Contact Analysis

The ability to simulate contact or impact scenarios is a major part of FE analysis. LS-DYNA specifically, is one of the leading applications for use in car crash simulations with a big focus on air-bag deployment. The methods they use to simulate these scenarios are easily used to simulate a less complex contact problem such as an indentation test. The three main methods that are used to simulate a contact or impact scenario are the kinematic constraint method, penalty stiffness method, and the distributed parameter method.

The penalty stiffness method is the most commonly used contact algorithm which was introduced in 1988 by Kikuchi and Oden [62] and utilizes ideas such as the use of a normal spring by Hallquist et.al. [63] which was proposed in 1985. This penalty method is computationally implemented by applying springs normal between each node on the "slave" interface, and the "master" interface surface as shown schematically in Figure 2.14. This produces an interface force between the slave nodes and the master surface.

This interface force is proportional to the amount of penetration and is defined as

$$\mathrm{f}_s = -l k_i n_i \tag{2.48}$$

where f_s is the interface force applied to the slave node, l is the depth of interpretation, n_i is the normal vector from the point of contact, and k_i is the stiffness factor which for a brick element is given by

$$k_i = \frac{f_{si} K_i A_i^2}{\text{max(shell diagonal)}} \tag{2.49}$$

where f_{si} is a scale factor, K_i is the bulk modulus, and A_i is the area of the element face.

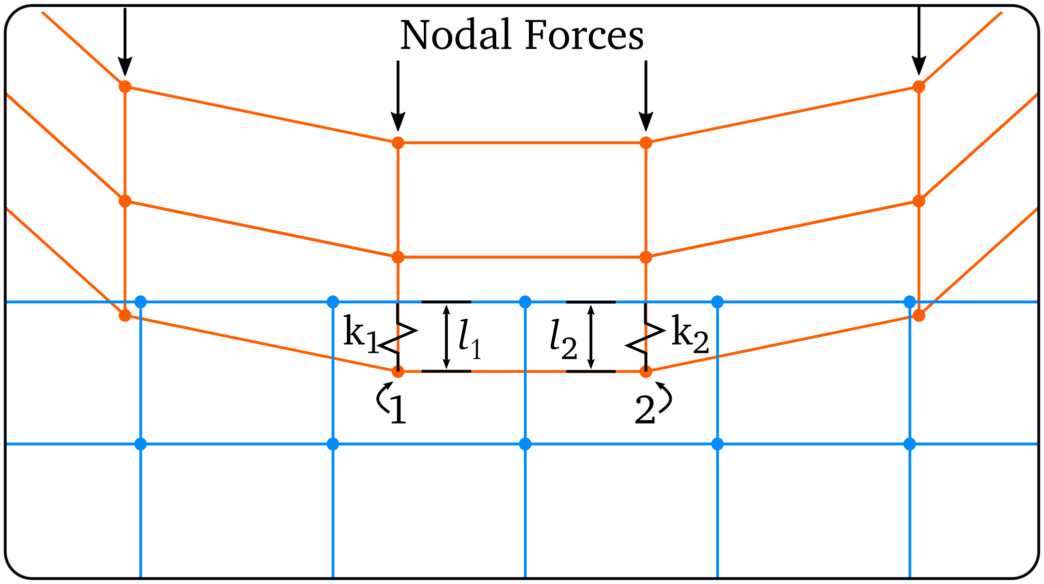

Figure 2.14: Schematic of slave nodes penetrating master surface

Once the solver then computes the unique stiffness modulus for each nodal spring system, the individual stiffnesses are then compiled into the global assembly matrix. Issues can occur with this method if the nodes on the master interface directly contact the nodes on the slave interface. As the penalty method is expecting a node to surface contact, it will be numerically unstable at these positions, so care should be taken to avoid this situation by adjusting the mesh size and/or positioning. This method of contact simulation is versatile as the penetration detection can be adjusted by adjusting the size of the timestep, and the stiffness value can be adjusted from the scale factor. There is a limit however to how effective this method can be. If there is a large enough difference between the elastic moduli of the contacting bodies, then the penetration can become too large for a timestep and therefore produce inaccurate results. Therefore, instead of lowering the stiffness scale factor, a soft constraint penalty formulation can be used. This formulation method uses the Courant-Friedrichs-Levy stability criterion in order to calculate a new stiffness value given by

$$k_{sc}(t) = 0.5 \cdot \mathrm{SOFSCL} \cdot m^{*} \cdot \left(\frac{1}{\Delta t_c(t)} \right)^2 \tag{2.50}$$

where k_{sc} is the soft constraint stiffness, SOFSCL is a scale factor, m^{*} is a mass function of the slave and master nodes, and Δt_c is the initial timestep. If the amount of time to successfully complete a timestep increases upon iteration, then the timestep is reset to its initial value to improve stability. Upon implementation, this contact formulation will typically use the largest stiffness value between k_i and k_{sc}.

Aside from the standard penalty stiffness, and the soft constraint formulations, there is also a general segment-penalty formulation that is highly used as well. This method is similar to the soft-constraint formulation however instead of a nodal mass function, this method is based on segment masses on the slave (m_1) and master (m_2) surface. This can be a more useful contact algorithm as it does not contain the issue of direct node on node contact that the standard penalty stiffness formulation contains because this method checks for segment penetration instead of nodal penetration. The stiffness formulation for this method is given by

$$k_{cs}(t) = 0.5 \cdot \text{SOFSCL} \cdot \left\{ \begin{matrix} \text{SFS} \\ \text{or} \\ \text{SFM} \end{matrix} \right\} \cdot \left(\frac{m_1 m_2}{m_1 + m_2} \right) \cdot \left(\frac{1}{\Delta t_c(t)} \right)^2 \tag{2.51}$$

where SFS and SFM are independent slave and master penalty scale factors respectively. For this formulation, Δt_c is still the initial timestep however this formulation allows for a 5% increase while still maintaining stability.

This penalty stiffness method is the standard method used within LS-DYNA however when using the implicit non-linear solver, there is also the option of using mortar contact. This contact scheme was initially created to improve upon metal forming analysis however, it has since been expanded into a general contact formulation [64]. Mortar contact determines if one segment has penetrated another segment and calculates the resultant contact pressure by

$$\sigma_n = \alpha \beta_s \beta_m \epsilon K_s f \left(\frac{d}{\epsilon d_c^s} \right) \tag{2.52}$$

where α is the stiffness scaling factor determined by the product of the scale factor of the slave surface (SFS), and a sliding scale factor (SLSFAC), K_s is the stiffness modulus of the slave segment, ϵ is a constant equal to 0.03, d_c^s is the characteristic length of the slave segment in contact, d is the penetration length, β_s and β_m are stiffness scale factors for the slave and master segments respectively, and f is a piecewise function given by

$$f\left(\frac{d}{\epsilon d_c^s} \right) = \begin{cases} \frac{1}{4} \left(\frac{d}{\epsilon d_c^s} \right)^2 & x < \frac{d_{max}}{2\epsilon d_c^s} \\ \text{cubic function dependent upon IGAP} & x \geq \frac{d_{max}}{2\epsilon d_c^s} \end{cases} \tag{2.53}$$

where $IGAP$ is a user input parameter for the contact card in LS-DYNA.

This method unlike the kinematic constraint method, can handle hourglassing effects. Hourglassing effects, as shown in Figure 2.15, arise in under integrated elements subjected to pure bending causing zero-energy deformation [64]. This causes the overall mesh to maintain its shape while individual elements become severely distorted. Hourglassing can be avoided all together by using higher-order elements however as the integration points increase, so does computational requirements. The penalty stiffness method can also achieve the conservation of momentum from a contact without the need of impact and release conditions [64].

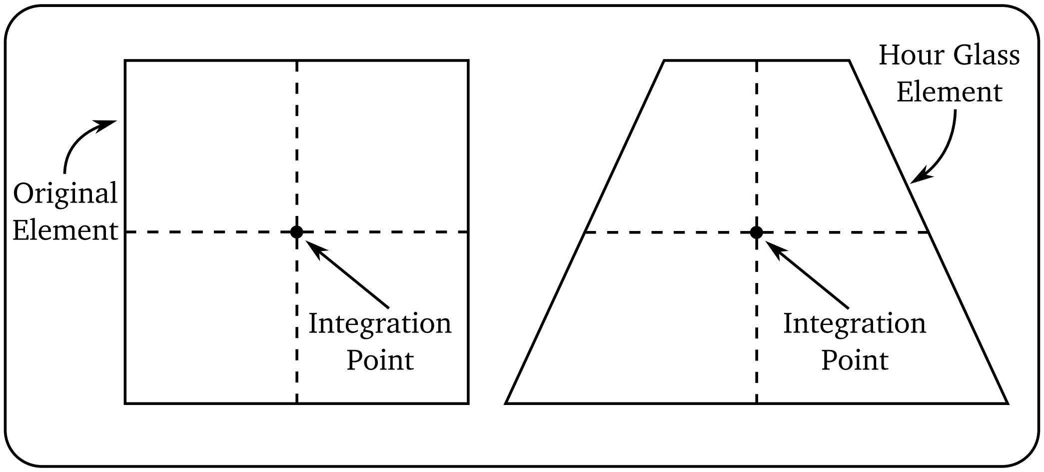

Figure 2.15: Schematic of an under integrated hourglassing element

The kinematic constraint method applies constraints to the global equations by transferring the displacement components of the slave nodes along the contact interface [64]. By doing this, the normal degree of freedom on the interface is eliminated, and during explicit analysis, the mass of each element is lumped together such that the global degrees of freedom on each master node are coupled [64]. This method then uses impact and release conditions to ensure that the momentum from the impact is conserved. The issue with this method is that under an application of high loading, kinks can appear in the mesh where a master node has penetrated the slave surface without any form of resistance, and therefore does not conserve the momentum of the contact

[64]. As discussed, this method also produces issues when hour glassing is of concern.

The distributed parameter method uses half of the slave elements mass for each element in contact, and distributes this to cover the master surface area which is determined via the internal stress of each element receiving the mass [64]. After the distribution of mass and pressure, the acceleration of the master surface can then be updated, and constraints can then be applied to the slave node accelerations and velocities [64]. This will ensure that the slave nodes simply move along the master surface. This method does not utilize the “put back on” approach that other methods use that allow a small amount of penetration and then place the slave nodes back on the master surface. Instead the calculations of the slave element volumes ignore any intrusion into the master surface.

2.3.6 Role of Friction on Indentation

As seen previously in Section 2.2.1 when discussing Hertzian contact for a purely elastic material, a contact with zero friction is assumed. Realistically this is not the case and there will always be some form of friction between two materials especially if the two materials are dry metals. Therefore, an analysis on the role that friction plays on indentation testing is necessary. Historically it has been assumed that due to the normality of indentation forces, the friction between the indenter and specimen has minimal effect on the resultant overall normal forces and stresses. For sharp indenters, Bucaille et.al. [65] determined that the effect of friction plays a large role in the normal forces at the tip of a sharp indenter if the tip half-angle is equal to or under 50°, but above 60°shows a negligible amount of normal force variation. Alcalá [66] determined that materials that exhibit a significant amount of material pile-up around the indentation site can be significantly affected due to frictional variations, whereas materials with less significant pileup shows negligible results due to friction. In contrast to these two findings, Tan and Shen [67] found that friction had a distinct effect, where including friction as opposed to a free-sliding surface provided a harder response. Harsono et.al. [68] examined the work from these previous studies and performed work of their own to find that using an indenter tip with a half-angle of 60°on a material that has a strain hardening coefficient greater than 0.2 showed that friction may be neglected, and for the alternatives friction should be considered. Therefore, the role of friction on a sharp indenter has been examined, however due to the absence of a sharp tip, the role of friction for a spherical indenter should be examined as well.

A spherical indenter unlike a sharp-tip indenter does not have a central stress concentrator at the tip. With a smooth indenter surface the effects of friction should be minimal, however as found by Carlsson et.al [69] for material characterization using Brinell indention, the difference between frictionless and full adhesion are less than 10%, but the stress and strain field can vary significantly. This has been additionally reinforced by Mesarovic and Fleck [70] who noted the same outcome but also noted that for material characterization, friction should also be included for elastic-plastic materials. Therefore, if the stress field underneath an indentation is of significant interest then the friction between the indenter and the workpiece should be accounted for.

Chapter 3

Experimental and Simulation Methods

3.1 Experimental Technique

3.1.1 Material Characterization

As this work aims to increase confidence towards NBIT being a successful modification of BIT, a popular elastic-plastic material was chosen as the substrate. Hot-rolled AISI 4340 steel was chosen due to its popularity, availability, and elastic-plastic properties. The chemical composition was gathered via inductively coupled plasma testing with results shown in Table 3.1a. These composition results show good agreement with the standard AISI 4340 composition ranges found in *ASM Handbook Volume 1* [71]. X-ray diffraction experiments were completed using a Bruker D8 Advance system with Cu-Kα radiation with a wavelength, tube current, and tube voltage of 0.154nm, 40kA, and 40kV respectively. The resultant peaks were compared to a standard Fe-Ni-Cr steel pattern where the angle of the major peaks coincide however intensities differed due to texturing on the surface of the solid sample [72].

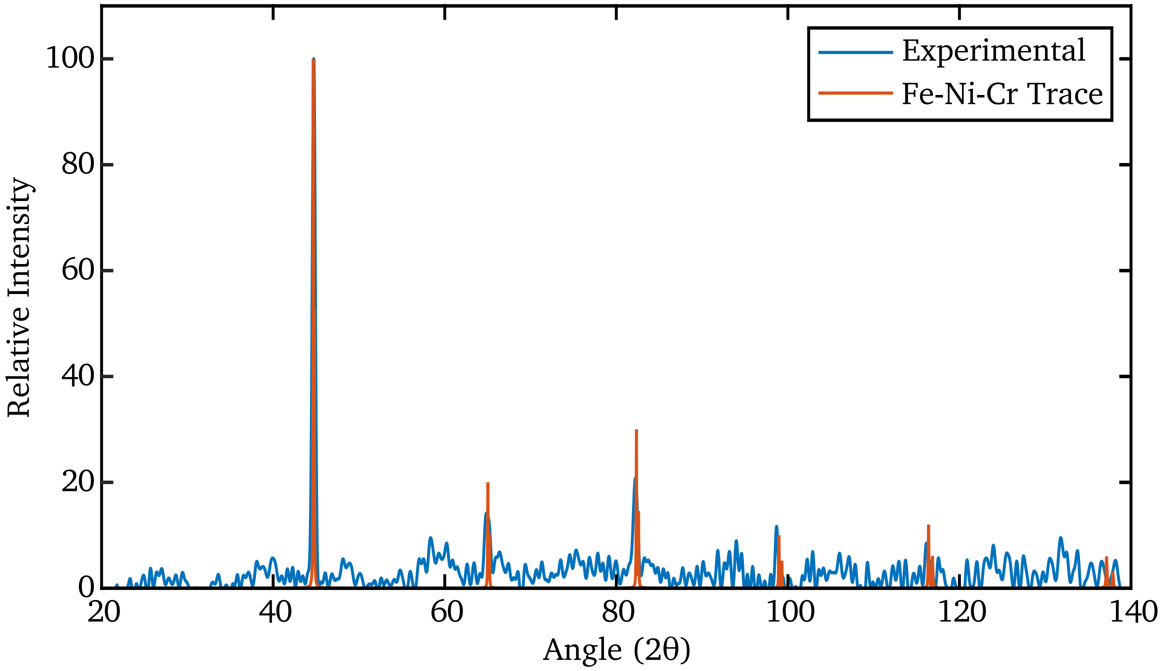

Figure 3.1: XRD pattern of experimental 4340 sample with standard Fe-Ni-Cr pattern

Hardness testing was done using the Rockwell B hardness (HRB) scale with a 1/16" WC-6wt% Co indenter which follows the Rockwell hardness equations as

$$HRB = 130 - \frac{h}{0.002} \tag{3.1}$$

where h is the height difference created by the residual deformation within the sample. Using this method produced an HRB value of 92.2. This is lower than the expected HRB value of 99.0 [71] for a standard AISI 4340 steel sample. A sample of the AISI 4340 steel was then split and magnetically ground to ensure the faces were parallel. One of the parallel surfaces was then polished using 400 and 600 grit SiC abrasive paper, and finished with 9μm, 3μm, and 1μm diamond polishing pastes. Microstructural analysis was completed using a 2% nital etchant composed of 2% HNO_3 and 98% ethanol.

The etchant revealed a tempered structure that contains a combination of ferrite and coarse pearlite shown in Figure 3.2. When compared to existing micrographs [73] this sample of AISI 4340 steel must have been normalized and subsequently annealed where the annealing temperature was held just below the austenizing temperature. Due to this annealing temperature the growth rate of pearlite was high which created large pearlite nodules [73]. The presence of coarse pearlite causes a reduced resistance to deformations and therefore accounts for the decreased HRB value. The mechanical properties of the AISI 4340 steel sample are shown in Table 3.1b.

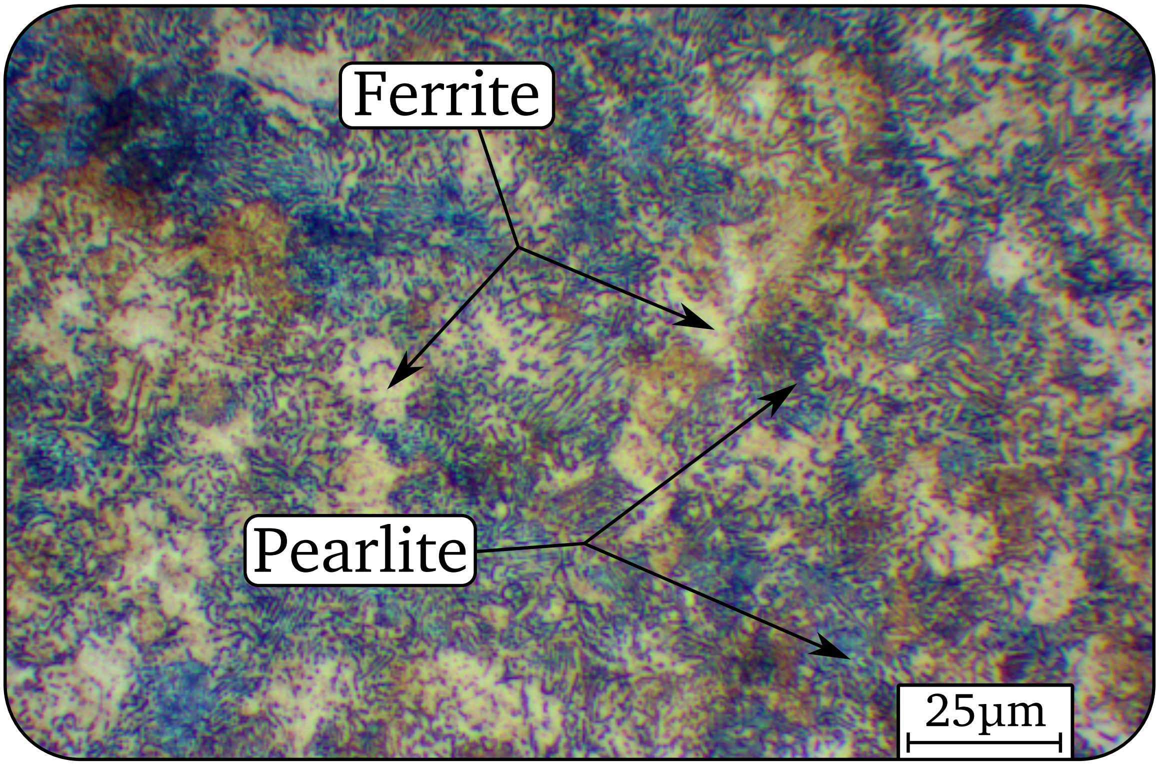

Figure 3.2: Microstructure of 4340 steel sample

Table 3.1: AISI 4340 chemical and mechanical properties

a) Chemical Composition (weight %)

Fe	C	Ni	Cr	Mn	Mo	Si
96.16	0.41	1.640	0.850	0.748	0.249	0.321

b) Mechanical Properties

Young's Modulus (GPa)	205	[74]
Hardness (HRB)	92.2	
Poisson's Ratio	0.29	[74]
Density (g/cc)	7.85	[74]

3.1.2 Sputtering Process

For standard sheet metal fabrication, the circle array that is used for residual strain analysis is relatively large and therefore can be created via several standard methods such as screen printing or photo emulsion [4]. The area of interest for strain analysis in the current work is much smaller than conventional circular grid analysis and therefore to create the circle array a Hitachi FB-2000A focused ion beam (FIB) was used. The FIB uses a high energy beam of gallium ions to sputter the surface of a substrate. This sputtering technique is able to precisely remove material at a desired location where the accuracy of material removal is dependent upon the beam spot size. Due to the existence of the beam spot, a raster image can be imported into the FIB and used as a template for material removal where a pixel from the raster image is translated into a single beam spot location [75]. The beam current for this process is the main determining factor for material removal and therefore two separate beams were used in this process. A 0.029nA M-50 beam was used for surface observation and a 13.6 to 14.0nA M1-500 beam was used for material removal. The M-50 beam produces minimal material removal but allows for a secondary ion image to be safely viewed whereas the M1-500 beam will quickly sputter the surface which meant viewing from this beam directly sputtered the sample. Aside from the beam current, several other parameters can be adjusted such as the dwell time, frame count, and magnification. The dwell time is the amount of time the ion beam is active at a single beam spot location, the frame count is the number of times the ion beam repeats the desired raster pattern, and the magnification is used to change the resolution of the beam spot. For the current system, the dwell time is statically defined as 128µs and therefore the frame count and beam spot magnification are the two different parameters that can be adjusted to achieve a desired pattern.

These two parameters are important as adjusting the magnification causes a change in the beam spot size, while adjusting the frame count causes a change in the amount of material removal. This can be seen more clearly in Figure 3.3. This figure shows that even though the width of the sputtered line is identical at 2µm between the two images, the smaller spot size of 0.248µm/px seen on the right can more accurately reproduce the desired line. This increased accuracy does come at a cost in terms of increased fabrication time of the circle array. This is because as accuracy increases, the amount of beam spot locations required increases as well. Therefore, since the current system uses a static dwell time, the required fabrication time significantly increases. Fabrication time can then be reduced by reducing the frame count, however the increase in fabrication time due to the smaller beam spot size exceeds the decrease in fabrication time from the reduced frame counts. Therefore, the fabrication time is still typically higher. In order to get the best results for this work, the optimal values for these two parameters must be determined.

To determine the optimal parameters several different circles were created using the system dwell time of 128µs with a range of frame counts from 75 to 300 and a range of beam spot sizes from 0.496µm/px to 0.062µm/px. The circles created using a frame count of 150 with the 0.496µm/px beam spot size are shown in Figure 3.4 a and b. These parameters produced circles whose edges were not easily identifiable due to the large spot size however the fabrication time per circle is approximately 1min. Figure 3.4

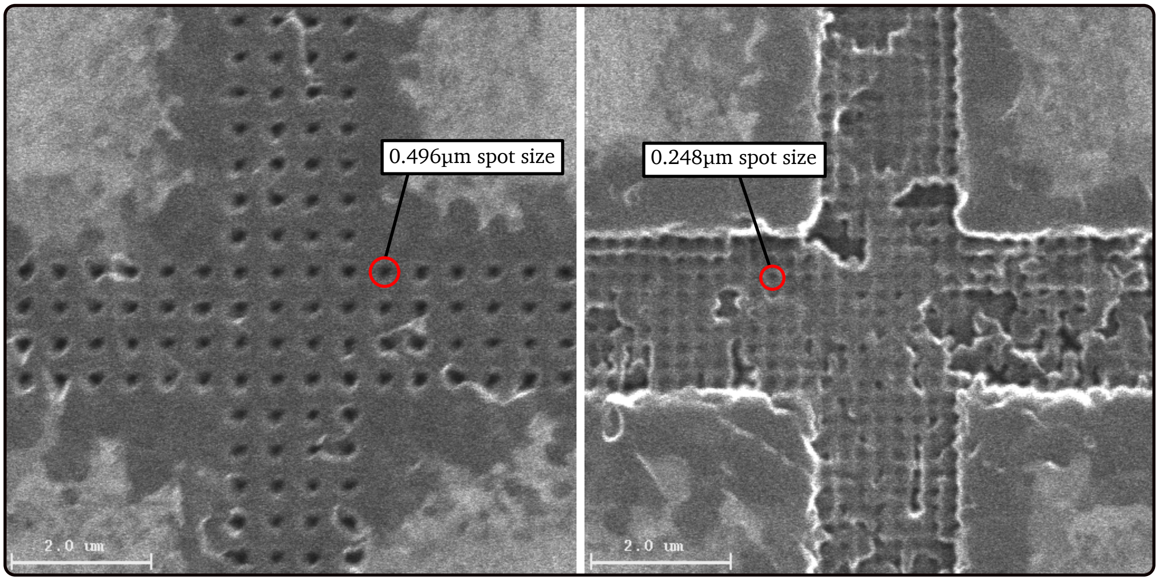

Figure 3.3: Close up SIM images of the center cross within the FIB circles showing difference in beam spot size of 0.496µm/px (left) and 0.248µm/px (right)

c and d used a lower frame count and an increased resolution of 75 and 0.062µm/px respectively. The increase in resolution means the beam spot size is concentrated onto a smaller portion of the sample and therefore can mill out material significantly faster. Even with a lower frame count this sample shows a significant increase in material removed and the circles edges from the SIM image are well defined however the edges seen from the optical image are less defined due to increase in roughness within the raster area. As discussed previously, the increase in accuracy requires an increase in fabrication time where this single circle required approximately 6.2min to complete. By ranging values between the two circles discussed, the parameters of 150 frame count with a beam spot of 0.248µm/px were used and are shown in Figure 3.4 e and f. These parameters show the circle edges slightly defined in the SIM image but much more easily identifiable using optical microscopy. This single circle required approximately 1.8min of fabrication time which is significantly less than the 0.062µm/px circle but not significantly more than the 0.496µm/px circle. Therefore, since the strain measurement from these samples will be conducted using optical microscopy, and the total desired number of circles per sample is 144, the optimal parameters were determined to be a frame count of 150, a system magnification of 128μm which creates a beam spot size of 0.248μm/px, and a dwell time of 128μs shown in Figures 3.4 e and f.

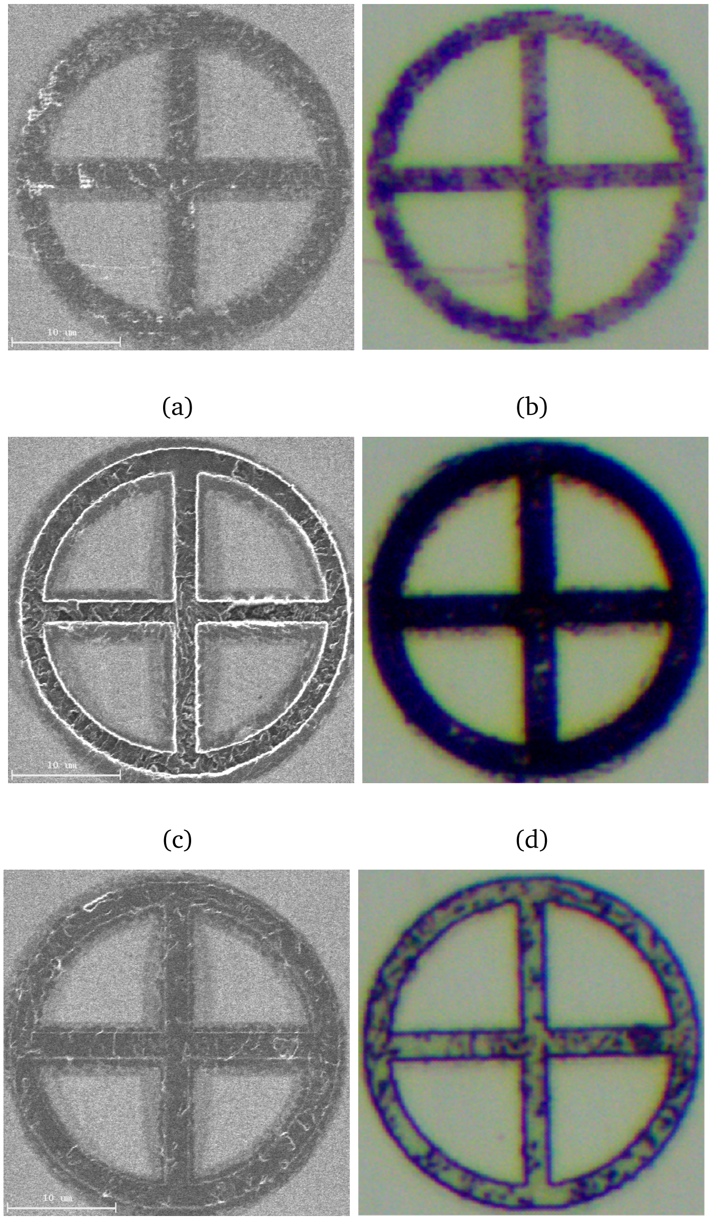

(a) (b)

(c) (d)

(e) (f)

Figure 3.4: Circles created via the FIB using 150 frame count with 0.496μm/px beam spot size from secondary ion microscopy (a) and optical microscopy (b), circles created using 75 frame count with 0.062μm/px from secondary ion microscopy (c) and optical microscopy (d), circles created with 150 frame count and 0.248μm/px beam spot size from secondary ion microscopy (e) and optical microscopy (f)

3.1.3 Experimental Set-up

The experimental process for this work can be split into two separate sections being normal indentation on a whole sample, and indentation on a split sample. For the whole samples, cubes of AISI 4340 steel were machined to have equal dimensions of 12mm. The top and bottom surfaces of these samples were also magnetically ground to ensure the faces were parallel. Once ground the samples were then polished using an auto polisher with 400 and 600 grit SiC paper. The samples were then finished off with 3μm and 1μm diamond polishing paste. A Buhler 574 hardness tester was then used which followed the load curve shown in Figure 3.5. The minimum load used is a constant at 98.1N (10kgf) however the maximum indentation force was set to either 588.6N (60kgf), 981.0N (100kgf), or 1471.5N (150kgf) depending on the desired outcome. The residual indentation diameter was measured for each test though, and the HRB value was also recorded from the 981.0N load.

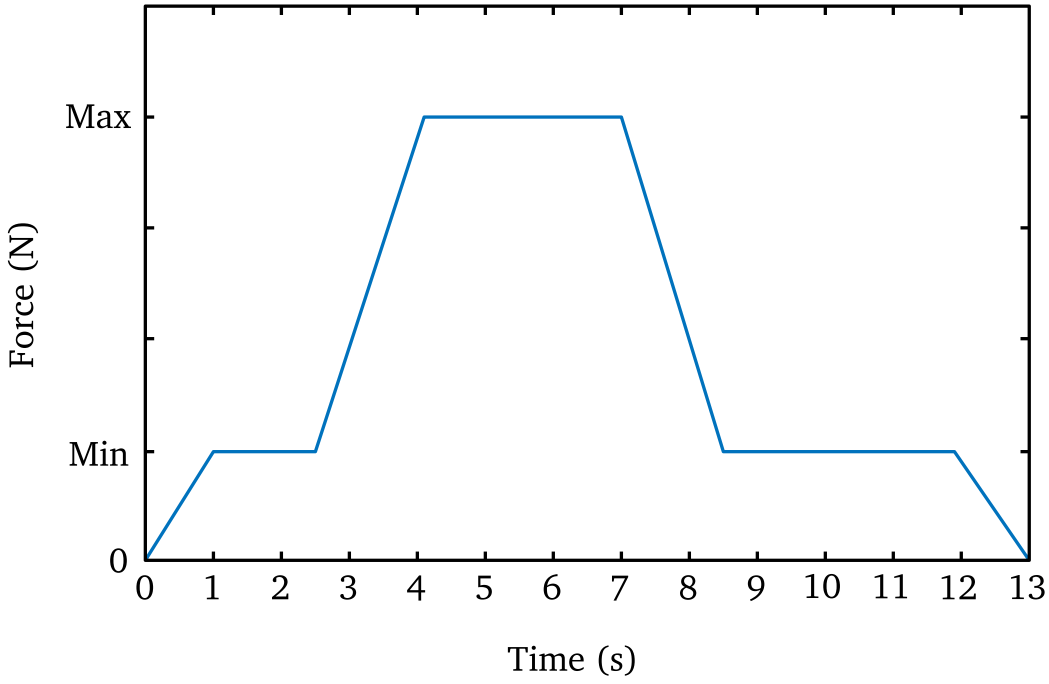

Figure 3.5: Standard load curve for Rockwell hardness tester

The split samples were created in a similar manner however they were machined to have dimensions of 12 x 6 x 12mm. The 12 x 12mm faces were magnetically ground and polished using the same procedure as the whole samples top surface. Once polished, one of the internal surfaces of the split sample had a circular grid sputtered onto it from the FIB. An example of the pattern input into the FIB as well as the resultant pattern on the internal surface is shown in Figure 3.6.

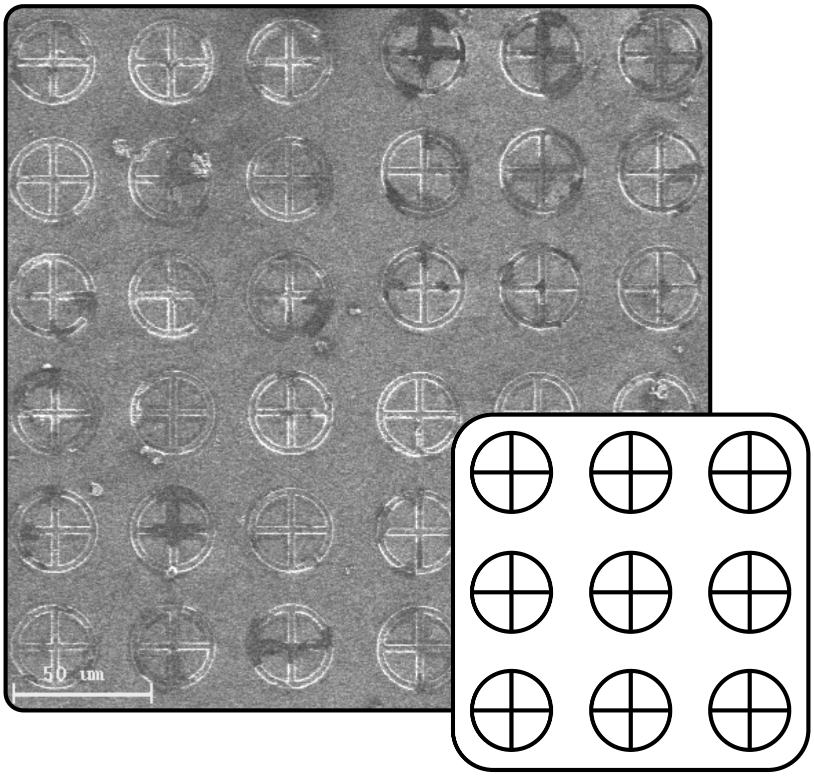

Figure 3.6: Circular grid from FIB on internal surface with raster input overlay

Once sputtered, two of the split samples were then clamped together to hand tight. After clamping two halves together it was found that the top surfaces of the clamped sample were typically not perfectly aligned. To ensure that the load from an indentation along the interface was transferred properly, the top surfaces required aligning. Prior to aligning however the exact location of the FIB array was marked on the outside of the sample. Once the location was marked the top surface alignment was completed by using 240 and 320 grit paper on a manual polishing table. The aligned surface was then polished using 400 and 600 grit SiC paper and finished with 3μm and 1μm diamond polishing paste. The clamping force from this procedure was recorded using a Phidget button load cell which produces a load dependent voltage ratio that is transformed into a calibrated force via a Python script. This load cell was able to record loads up to 1961.3N (200kgf) however due to the use of a vice, the force gauge could not be used if the top surface was to be aligned and polished. To be able to confidently compare the experimental and simulated results, a clamping force was required. Therefore, a set of 10 separate tests were completed where each test consisted of tightening the vice to "hand-tight" and recording the resultant clamping force. The results from this test are tabulated in Table 3.2. A t-test was used with the results from this normally distributed data set to produce a 99% confidence interval for the clamping force of 867.6 ± 86.7N.

Table 3.2: Force results from "hand-tight" clamping

Test	Force (N)
1	849.55
2	1026.13
3	933.91
4	806.38
5	811.23
6	984.92
7	679.34
8	856.41
9	730.84
10	996.70

Once the split sample is clamped and the top surface is aligned and polished, the existing marks were utilized to create a line on the surface perpendicular to the interface indicating the location of the FIB array. As the FIB array is approximately 0.75mm wide, the proper measurement of the FIB location is essential. After marking the top surface, the sample is then indented along the split interface using the same loads as the whole samples. This process is non-trivial because if the indenter is misaligned with the interface then the indentation load is not evenly distributed between the two samples and therefore will produce a non-symmetric indentation. Also, if the indenter is misaligned with the surface mark the FIB array will not produce meaningful results, hence a live USB microscope was used to align the indenter with the split interface and the marking along the surface. The experimental set-up for this split sample is shown in Figure 3.7.

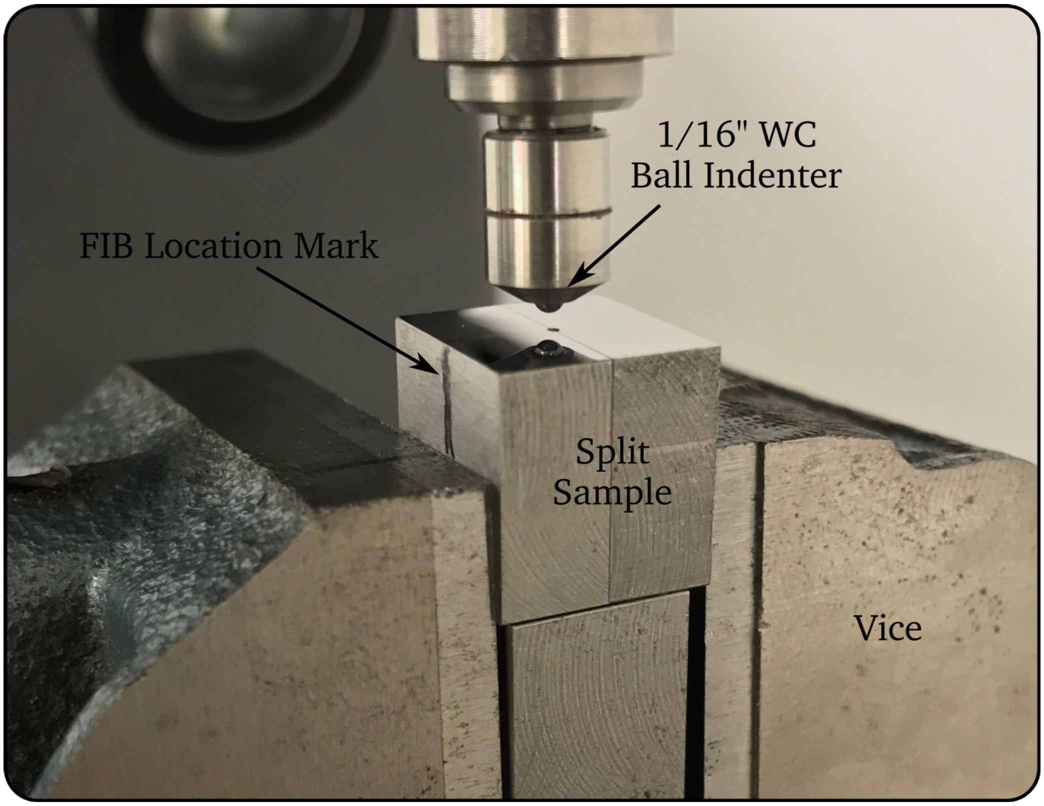

Figure 3.7: Experimental set-up of the non-bonded interface method

Once the indentation was completed the circles which sustained plastic deformation were transformed into ellipses. These ellipses can be used to determine the true principal strain by measuring the major and minor axes.

$$\epsilon_{Major} = \ln\left(\frac{L_{Major}}{L_0}\right) \tag{3.2}$$

$$\epsilon_{Minor} = \ln\left(\frac{L_{Minor}}{L_0}\right) \tag{3.3}$$

where L_{Major} is the length of the major axis, L_{Minor} is the length of the minor axis, and L_0 is the length of the original circle diameter which is known prior to testing.

3.2 Finite Element Model Development

3.2.1 Quarter Mesh Setup

The FE model for this work was created in three separate stages. First a quarter model without an indenter was created and used for determining the optimal element size and material model. Secondly, an indenter was then added to determine the proper contact algorithm and allow the adjustment of the material model parameters. Thirdly, a half model was then created using the optimal parameters determined from the quarter model.

Within the current field of simulating indentation testing, 2-dimensional axisymmetric elements are more commonly used to improve simulation time and simplify the modeling [76, 77, 45]. This is useful when analyzing the results for a homogeneous sample, however, the current work aims to simulate a split interface, hence a 3-dimensional model is required. Although not as common as the 2-dimensional model, 3-dimensional indentation models have been used as well. As 3-dimensional models are significantly more resource intensive than the 2-dimensional models, element transitions in the X and Y axis along with element biasing in the Z axis are commonly used to reduce computational requirements. This can cause issues as the area of interest beneath an indentation requires small elements to produce quality results, which means that a large Z axis bias is required. This produces small elements where desired beneath the indenter but also produces many elements sufficiently far from the indenter where they are not desired. Due to these undesired element sizes, significantly more computational resources are used than actually required. To improve this necessary bias in a 3-dimensional indentation model, a mesh was created for this work which uses transitions in the X, Y, and Z axis. An exploded view of these triaxial transitions is shown in Figure 3.8. This transitioned model uses 3-dimensional 8-node constant stress solid elements with hourglass control from the Belytschko-Bindeman assumed strain stiffness form for 3D elements as defined by LS-DYNA.

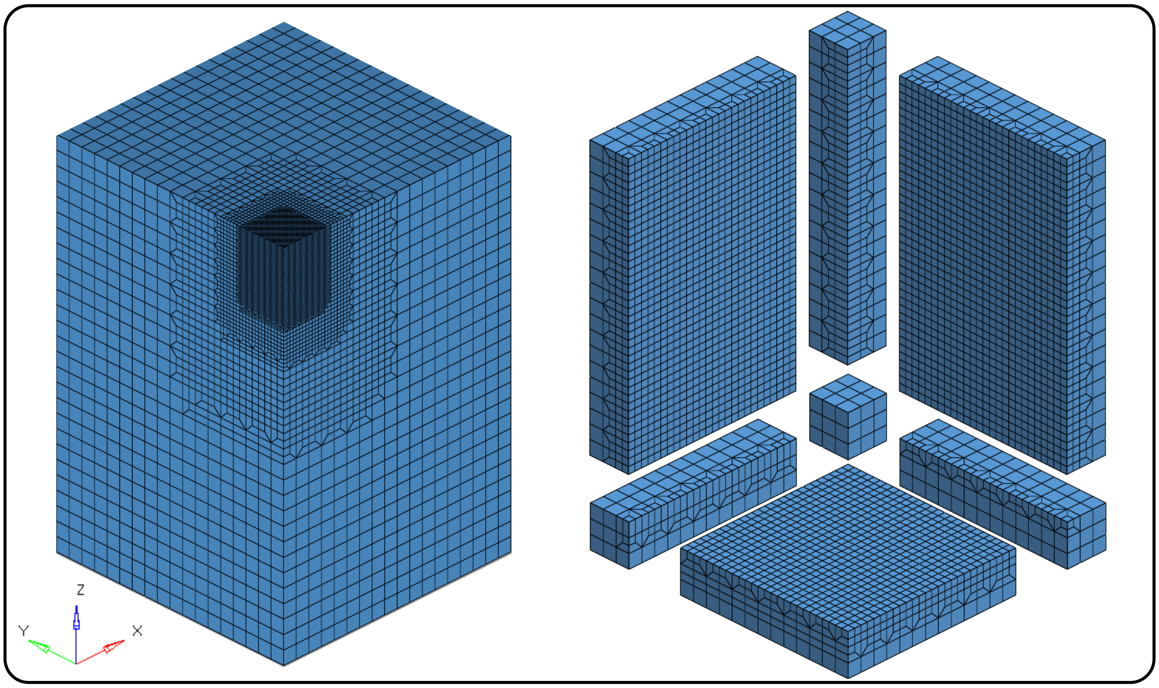

Figure 3.8: Exploded view of triaxial mesh transitions

By using these triaxial transitions the number of elements was able to be significantly reduced while also maintaining an optimal element size where desired. To determine the optimal mesh size within the area of interest beneath the applied load, a mesh convergence study was completed. This study used a parabolic pressure as the applied load as defined by Hertz seen in Equation 2.4. By using the parabolic pressure distribution, the contact radius and nodal forces are pre-defined. This allows for the nodal displacements to be the only deformation that is affected by the material properties and the mesh. For this work the quarter model used the -ZX and -ZY planes as symmetry boundary conditions. The outer nodes on the +ZX plane were constrained from displacements in the Y axis and rotation in the Z and X axes. The outer nodes on the +ZY plane were contained from displacements in the X axis and rotation in the Z and X axes. The bottom of the sample was constrained from displacements in Z axis and rotations in the X and Y axes.

By using mesh sizes ranging from 100µm to 6.25µm with a purely elastic material model using parameters defined in Table 3.1b with a contact radius of 0.1mm and a total force of 300N, the resultant FE model produced a converged displacement of 0.0101mm as shown in Figure 3.9. This figure shows that the mesh quickly converges to 10.1µm displacement for element sizes less than 50µm. To ensure proper convergence, the maximum internal stress was also analyzed as shown in Figure 3.10. This figure shows that the maximum internal stress does not converge until reaching element sizes equal or less than 12.5µm. From these results it is also shown that the simulation time of the 6.25µm element size model exhibits a 24-fold increase over the 12.5µm element size model. Therefore, the converged element size within the area of interest was determined to be 12.5µm.

Although the mesh size and purely elastic material model were verified, the actual use of the triaxial transitions were not. As it is known that elongated or distorted elements can be of bad quality and therefore cause inconsistent FE results [78], the triaxial transitions require verification as the transitions contain elongated elements. Therefore, by using

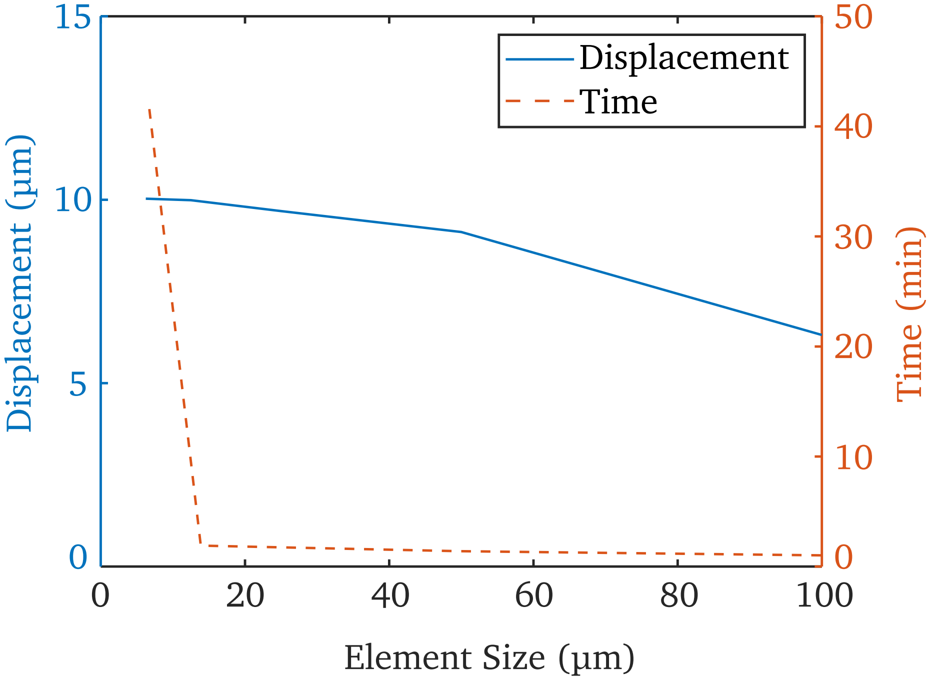

Figure 3.9: Mesh convergence for displacement

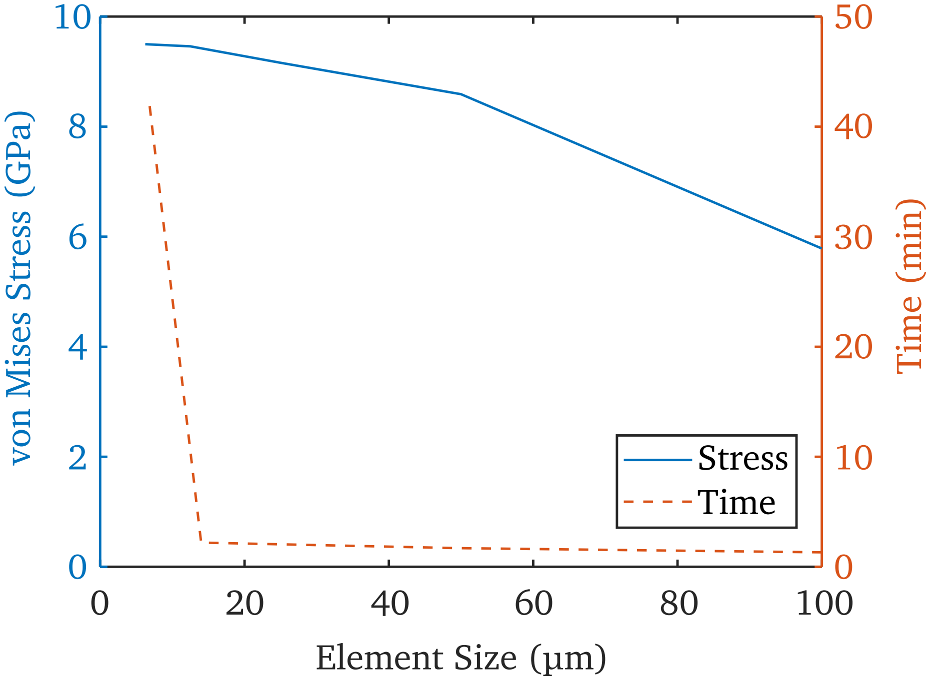

Figure 3.10: Mesh convergence for stress

the quarter model with the element size of 12.5µm within the area of interest along with a purely elastic material model, the results can be compared to the Hertzian elastic contact theory.

The Hertzian model allows for calculation of the load point displacement however the current comparison utilized a rigid indenter and therefore the load point displacement and the displacement of the node directly beneath the indenter will be equivalent. The Hertzian normal force was found by using Equation 2.9 with the same material parameters, contact radius, and the resultant load point displacement as the FE model. Using these parameters, the Hertzian model produced a required indentation force of 302.92N to displace 10.1μm of material. Comparing this to the FE model which required a 300N force to displace 10.1μm, this produces a 0.97% difference between the FE model and the Hertzian theory. Therefore, the triaxially transitioned mesh can be said to be verified. From this result, the element transitions, elements size, and elastic material model were verified. The next step for development is to add the indenter and determine the optimal contact algorithm.

The indenter for this work was initially modeled as a quarter of a half-sphere as seen in Figure 3.11 along with a purely elastic material model using coefficients seen in Table 3.1b. One of the most popular contact algorithms is the nodal contact scheme, hence it was initially chosen as the basis for the current work. Nodal contact however has a known vulnerability regarding a direct node on node contact. Therefore, the smallest element size for the indenter was initially chosen to be 20μm to avoid direct contact between the majority of the nodes. This direct contact is unavoidable on the center node though due to the use of the symmetry plane boundary conditions.

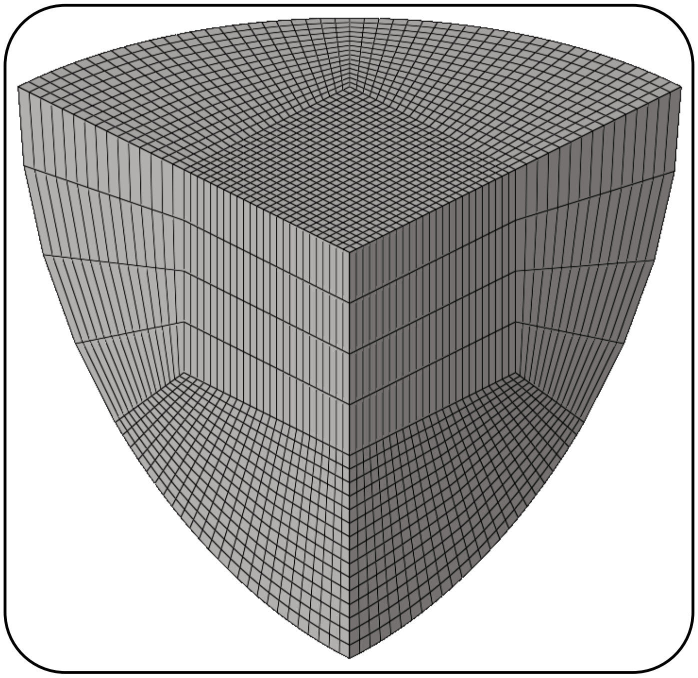

Figure 3.11: Finite element model of solid spherical indenter

3.2.2 Finite Element Model Refinements

Indenter Properties

As the goal of this work is to simulate a half-model, the solid indenter shown in Figure 3.11 was found to be sufficiently large to exceed the available computational resources of the current system. As this was determined early on in the current work, the experimental indenter and FE indenter were changed from hardened steel to WC - 6wt% Co. Therefore, as WC has a high elastic modulus as seen in Table 3.3, the indenter could be modeled using rigid elements. This allowed for a 2-dimensional indenter to be used which significantly reduced the number of elements as well as simplified the respective material model allowing for an additional relief in computational resources.

To ensure that the rigid indenter would properly compare to the non-rigid counterpart, an indentation was simulated using a 588.6N force. The material model for the substrate was also changed to the simplified Johnson-Cook model using the standard parameters

Table 3.3: Mechanical properties of 1/16" WC - 6wt% Co ball indenter

Young's Modulus (GPa)	633
Poisson's Ratio	0.20
Density (g/cc)	14.8

defined by Johnson and Cook [58] in order to simulate plastic deformation, and be able to record the residual deformations from the indentation. For this analysis, the material model of the indenter was varied between fully rigid and non-rigid elastic. The solid indenter model shown in Figure 3.11 is using the elastic indenter model, while the shell indenter shown in Figure 3.12 is using the fully rigid material model.

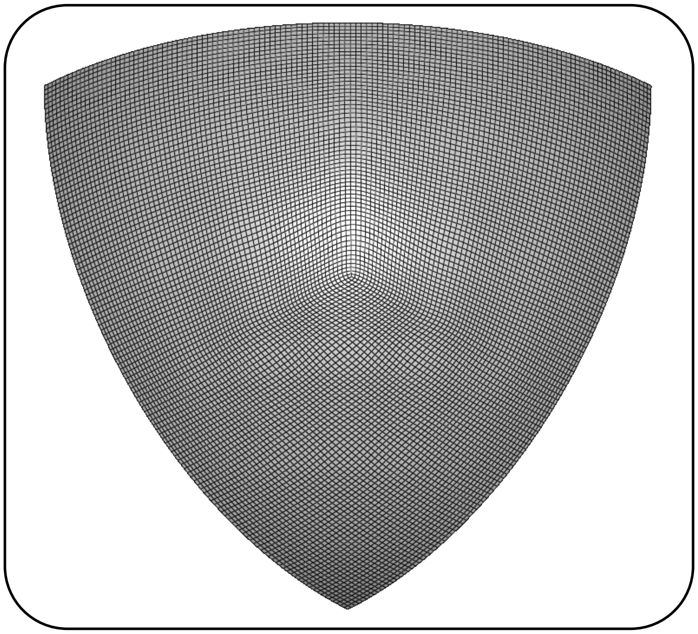

Figure 3.12: Finite element model of rigid shell spherical indenter

The resultant deformation curve of the center nodal point in the substrate from the indenter is seen in Figure 3.13. The results of this show a 5.0% difference in residual displacement. It is also shown in Figure 3.14 that the internal von Mises stress correspond well with each other. Therefore, even though the material model and contact algorithm are yet to be verified, the rigid indenter has proven to be a good approximation of the non-rigid indenter. From this comparison it was also found that the fully rigid shell indenter required approximately 35% less computational resources, as well as approximately 50% the amount of time required to complete the analysis. Therefore, using the rigid shell indenter for the subsequent simulations will significantly reduce the amount of time required for determining additional refinements.

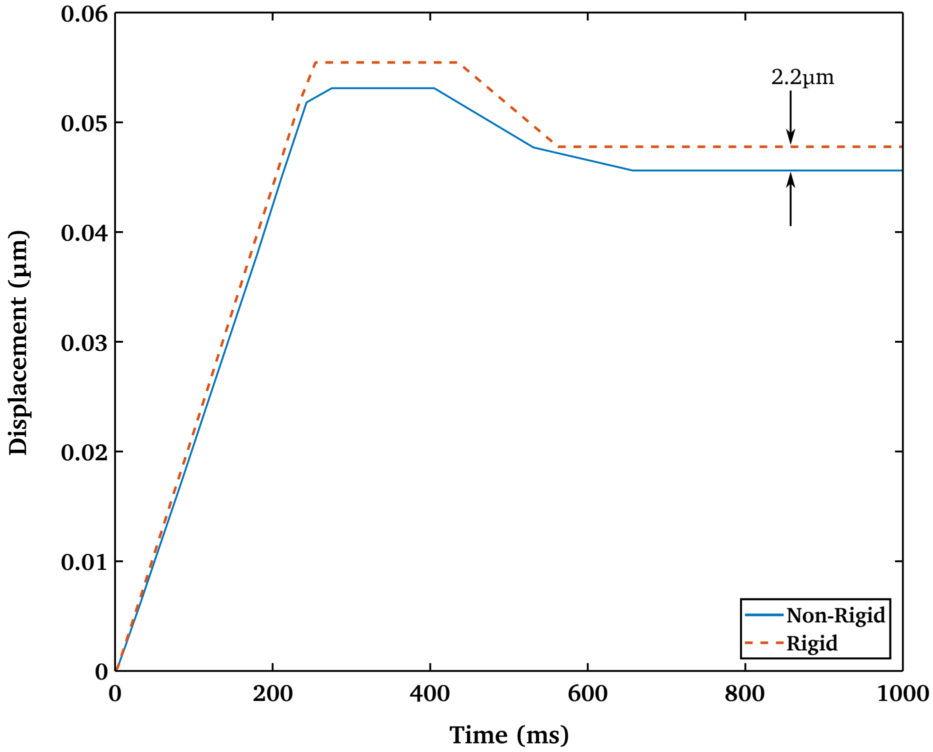

Figure 3.13: Center nodal displacement from rigid and non-rigid indenter

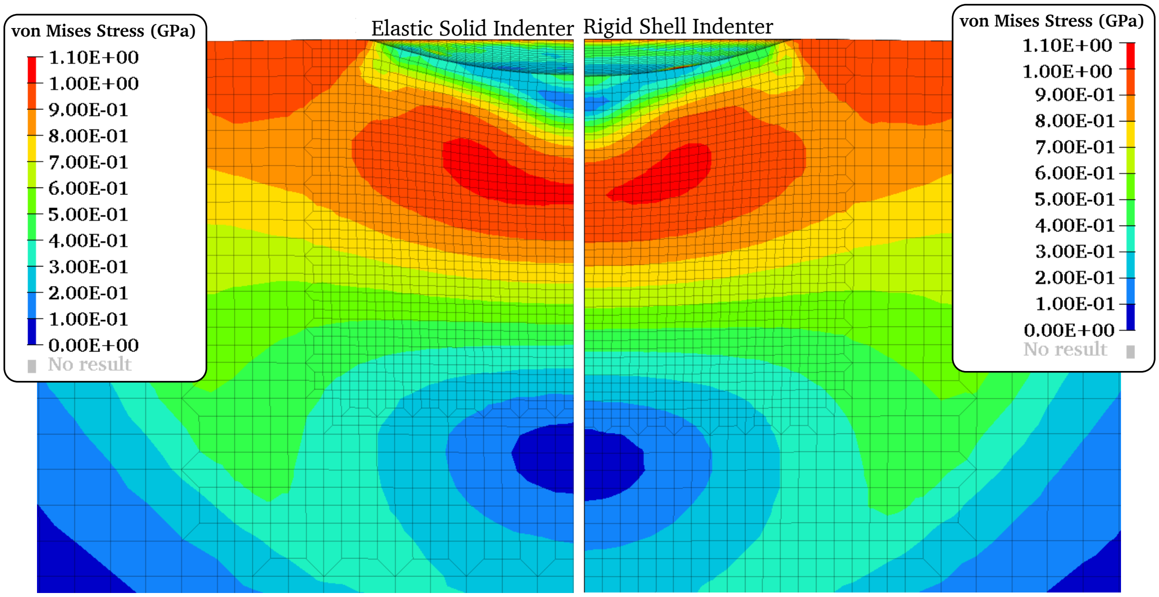

Figure 3.14: Internal surface of quarter model showing von Mises strain between the elastic model and the rigid model.

Contact Algorithm

To properly determine the correct contact algorithm for this work, the interpenetration between the indenter and sample was analyzed along with the stability of the contact.

The first algorithm chosen was the non-mortar nodal penalty stiffness contact which checks whether a node has penetrated a surface. This contact scheme allowed for large interpenetrations of 5μm between nodes at the center of contact due to the direct node-on-node contact. A wide variety of stiffness values were used with this method in an attempt to reduce the interpenetration however once the stiffness value exceeds a certain threshold, the stability of the contact significantly decreases which causes an increase in simulation time and produces significant noise in the force vs displacement curves. Therefore, while maintaining the penalty stiffness formulation, the contact scheme was changed to surface to surface contact. This contact scheme checks to see if a surface has penetrated another surface and therefore the nodal interpenetration was not as significant. This contact scheme allowed for a maximum interpenetration of 1μm and therefore is the superior choice compared to the alternative. Along with this surface to surface contact was the option of using mortar designation. Mortar contact is an LS-DYNA option which is recommended for use in implicit analysis. This option is a penalty-based surface to surface contact algorithm which when activated allowed for a maximum interpenetration of 0.38μm. As the penalty stiffness requires some interpenetration in order for contact to be detected, this value was accepted without further stiffness value alterations. Therefore, for the current work, the use of the surface to surface mortar contact scheme was chosen.

Time Step

As the current work utilizes an implicit solver, the time step is able to be manually adjusted. As previously discussed, the timestep can have a large effect on the deformation results from the contact algorithm, especially when contact is first occurring. Therefore, a small timestep is initially desired in order to best suite the contact algorithm, where the timestep can then increase as the stability increases as well. To determine the optimal minimum timestep, four identical FE simulations were conducted which utilize a minimum timestep of 0.01, 0.1, 1.0, and 10.0ms respectively. As the timestep increases after a stable contact iteration, the overall simulation time did not significantly change. To analyze these results though, the interpenetration of the indenter and the substrate was measured. The results from this analysis are shown in Figure 3.15 which shows that as the minimum timestep increases, the contact becomes less stable however the difference appears to be negligible. These results also only show the minimum timesteps from 0.01, 0.1, and 1.0ms. This is because the 10ms minimum timestep was unable to detect the initial contact and therefore the indentation did not even occur.

Therefore, as the difference in interpenetration caused by the timestep is determined to

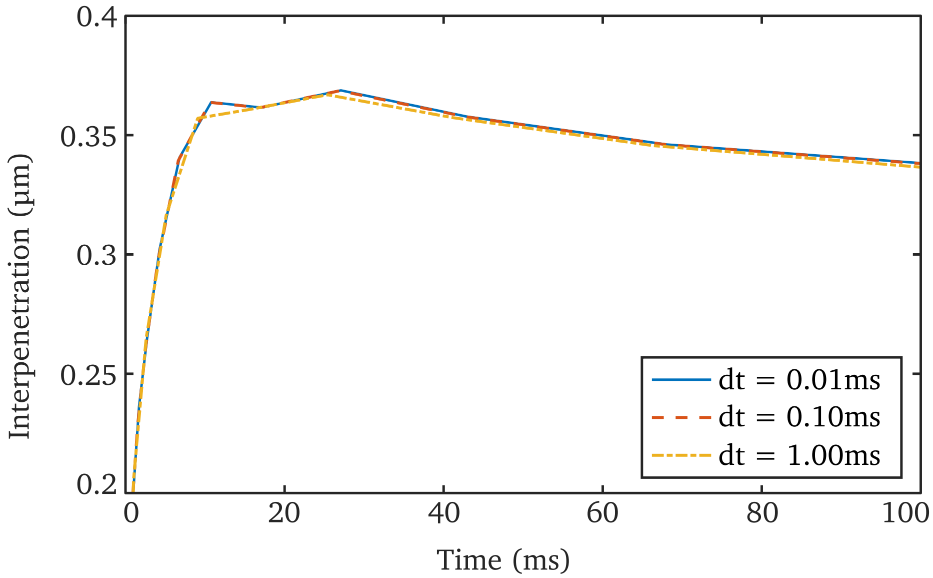

Figure 3.15: Interpenetration of indenter and substrate using increasing initial timesteps

be negligible, the 1ms minimum time was chosen. As the minimum time is important for properly simulating first contact, the maximum timestep is also important as it maintains the boundary at which the solution is computed. If the maximum timestep is small, then the solution will be more accurate as more data points will be computed. The downside to this is that the amount of data points can be excessive and therefore be computationally excessive. If the timestep is too large, then significant events such as an indenter reaching its maximum displacement may be completely missed due to it occurring between the timestep iterations. Therefore, to optimize the maximum timestep in order to maintain accurate results while not producing excessive data points, three identical simulations were created which utilize a maximum timestep of 100, 1000, and 2500ms respectively. The results from these simulations are shown in Figure 3.16. The figure displayed shows the displacement of the workpiece directly below the indenter through the simulation. These results show that the overall trend agrees between the timesteps however the 2500ms timestep misses several smaller points that the other timesteps account for.

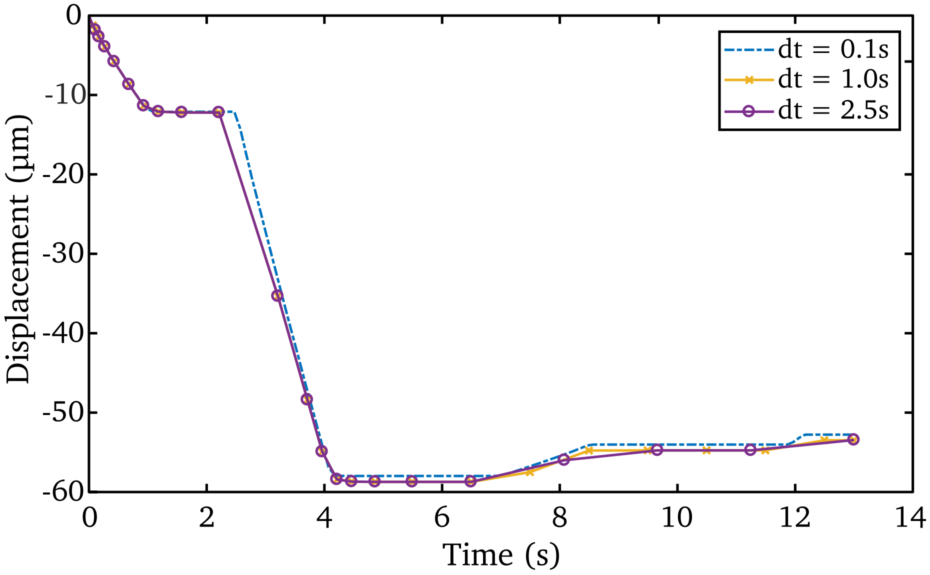

Figure 3.16: Maximum displacement curve of workpiece from changing max timestep

From this analysis, the overall simulation time was also compared. It was found that the 0.1, 1.0, and 2.5s maximum timestep required 250, 118, and 35 minutes of simulation time respectively. Although the displacement curves are similar and the 2.5s maximum timestep requires less overall time, the 1000ms maximum timestep was chosen as the increase in simulation time was fairly insignificant compared to the requirement of accurately simulating the experimental load curve.

Material Model

The material model used for verification of the mesh was the purely elastic model. The experimental sample however is AISI 4340 which undergoes elastic-plastic deformation. As discussed in Section 2.2.2 there are no analytical models for elastic-plastic deformation. Therefore, the material model must be an elastic-plastic model defined by LS-DYNA where the results can be compared to experimental indentations. LS-DYNA has a large number of material models able to deal with plasticity effects however current research shows that the Johnson-Cook material model is popular for AISI 4340 especially for use in indentation testing [53, 59, 60]. This current work began using the Johnson-Cook model however due to temperature effects being negligible for standard indentation testing, the simplified Johnson-Cook model was quickly adopted. This simplified model requires 50% less computational resources and removes the temperature dependency from the full model.

To properly determine the optimal Johnson-Cook material model parameters, a sample of AISI 4340 was used to produce a set of ten indentations using a maximum load of 588.6N. This experiment allowed for the residual radius of the indentation as well as the difference in indentation depths (h) value from the hardness equation seen in Equation 3.1 to be determined. From these results, the difference in indentation depths produced a sample mean of 43.5μm with a standard deviation of 0.49μm and sample mean of the indentation radius of 301.6μm with a standard deviation of 3.4μm. Using these values, a t-test can be used to produce confidence intervals using

$$CI = \bar{x} \pm t_{n-1,\alpha/2} \frac{s}{\sqrt{n}} \tag{3.4}$$

where $\bar{x}$ is the sample mean, α is the significance level, n is the sample size, and s is the sample standard deviation. Therefore, with sample means and standard deviations from these results, and using $t_{9,0.01} = 2.82$, the confidence intervals for the h value and radius are found to be

$$CI_h = 43.5 \pm 0.44 \mu m \tag{3.5}$$

$$CI_{radius} = 301.6 \pm 3.9 \mu m \tag{3.6}$$

As AISI 4340 steel has been used with the Johnson-Cook model, current research shows that the standard Johnson-Cook coefficients found initially by Johnson and Cook [58] produce quality results. When using the standard Johnson-Cook material coefficients

Table 3.4: Comparison of coefficients for the Johnson-Cook material model

JC Parameter	Rule Values [79]	Standard Values [58]
A	396 MPa	792 MPa
B	820 MPa	510 MPa
n	0.397	0.260
C	0.014	0.014

on the current FE model, the resultant *h* value and residual radius were found to be 28.1μm and 252μm respectively. This produced a 35.4% error in the *h* value and a 16.4% error in the residual radius. Therefore, the standard Johnson-Cook coefficients would be insufficient at producing quality results compared to the experimental samples. After further research it was found that Rule [79] determined that the Johnson-Cook coefficients for a material can differ significantly if the preprocessing of the material is varied. Rule [79] produced different Johnson-Cook coefficients found through Taylor testing AISI 4340 steel where they can be seen compared to the standard coefficients in Table 3.4.

By using the Rule coefficients for the Johnson-Cook model, the FE results produced an *h* value of 42.6μm and a residual radius of 305μm. This produced a 2.1% error in the *h* value and a 1.1% error in the residual radius. Therefore, the Rule coefficients produce quality results. Although these coefficients work well using the 588.6N indentation force, higher forces will be used as well. Therefore, testing was also conducted using the 981.0N indentation load. This testing used a single indentation and compared the residual depth, radius, and HRB value between the experimental and FE results using the standard Johnson-Cook model coefficients and the Rule coefficients. The results from this testing can be found in Table 3.5. These results show that even at the higher indentation forces, the Rule coefficients maintained close agreement to the experimental results, while the Johnson-Cook standard coefficients do not. Therefore, the Rule coefficients were determined to be the optimal coefficients to compare this

Table 3.5: Experimental and FE results from HRB test using various Johnson-Cook coefficients

Parameter	Experimental	Results using Rule	Results using Standard
Hardness (HRB)	92.2	92.0	104.7
Depth (μm)	87.7	87.0	58.1
Radius (μm)	377.7	384.0	320.0

model to the experimental results.

3.2.3 Split Finite Element Model

The split FE model was created by using the optimized quarter model mesh and mirroring it about the ZX plane. This created a free interface between two separate specimens. As the split model uses the optimal parameters from the quarter model, this mesh was created using the same 3-dimensional 8-node constant stress solid elements with hourglass control from the Belytschko-Bindeman assumed strain stiffness formulation. The material model is the simplified Johnson-Cook model using coefficients determined by Rule [79]. The contact algorithm is the mortar contact which uses a soft surface to surface contact scheme. It should be noted that because of the various indentation forces that will be used, the resultant deformation will increase with increasing force. Therefore, three separate split models were created to accommodate for the increased deformation so as to not have direct contact with mesh transitions. This means that the deformation of the mesh was contained within the small element area around the indentation. The mesh configuration for the 588.6N indentation force can be seen in Figure 3.17.

Even though there are three separate models, all of the models have identical boundary conditions. Each half model exploits the half symmetry of the experimental model by using the ZY plane as a symmetry plane. This symmetry plane constrains the surface nodes from displacements in the X axis and rotations in the Z and Y axes. The bottom

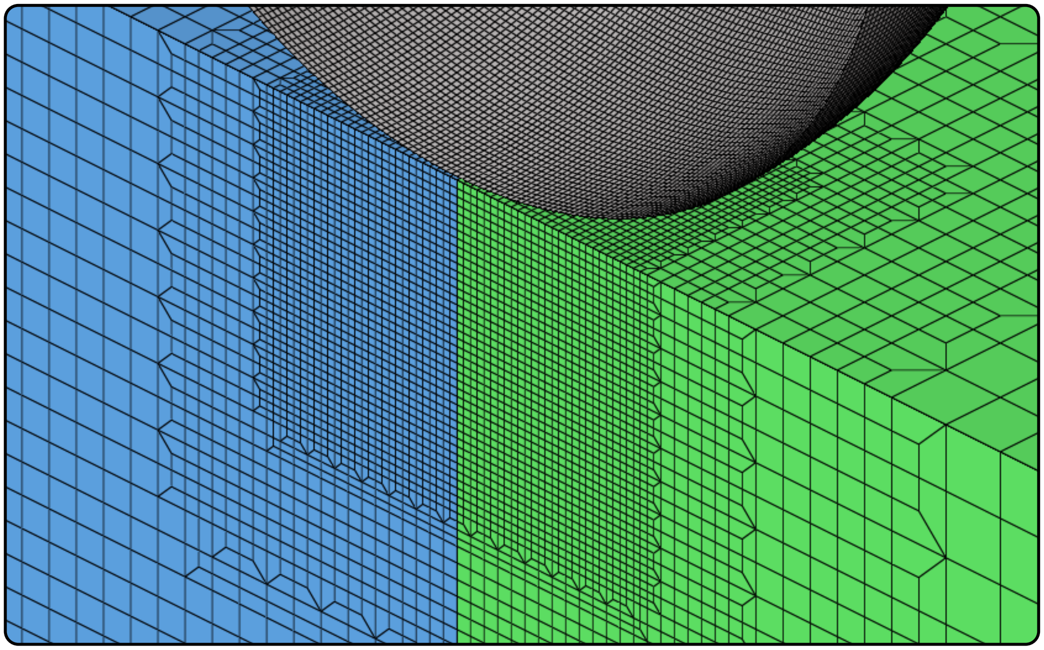

Figure 3.17: Close up of split mesh showing continuous indenter and discontinuous substrate

of the samples is constrained from displacements in the Z axis and rotations in the X and Y axes. The ZX plane was then used to produce the clamping boundary conditions. One of the outer surfaces in the ZX plane was constrained from displacements in the Y axis and rotations in the Z and X axes. The other outer surface in the ZX plane was then used to produce the 833.9N clamping force by applying a nodal force in the +Y direction on each of the surface nodes. This can be seen schematically in Figure 3.18.

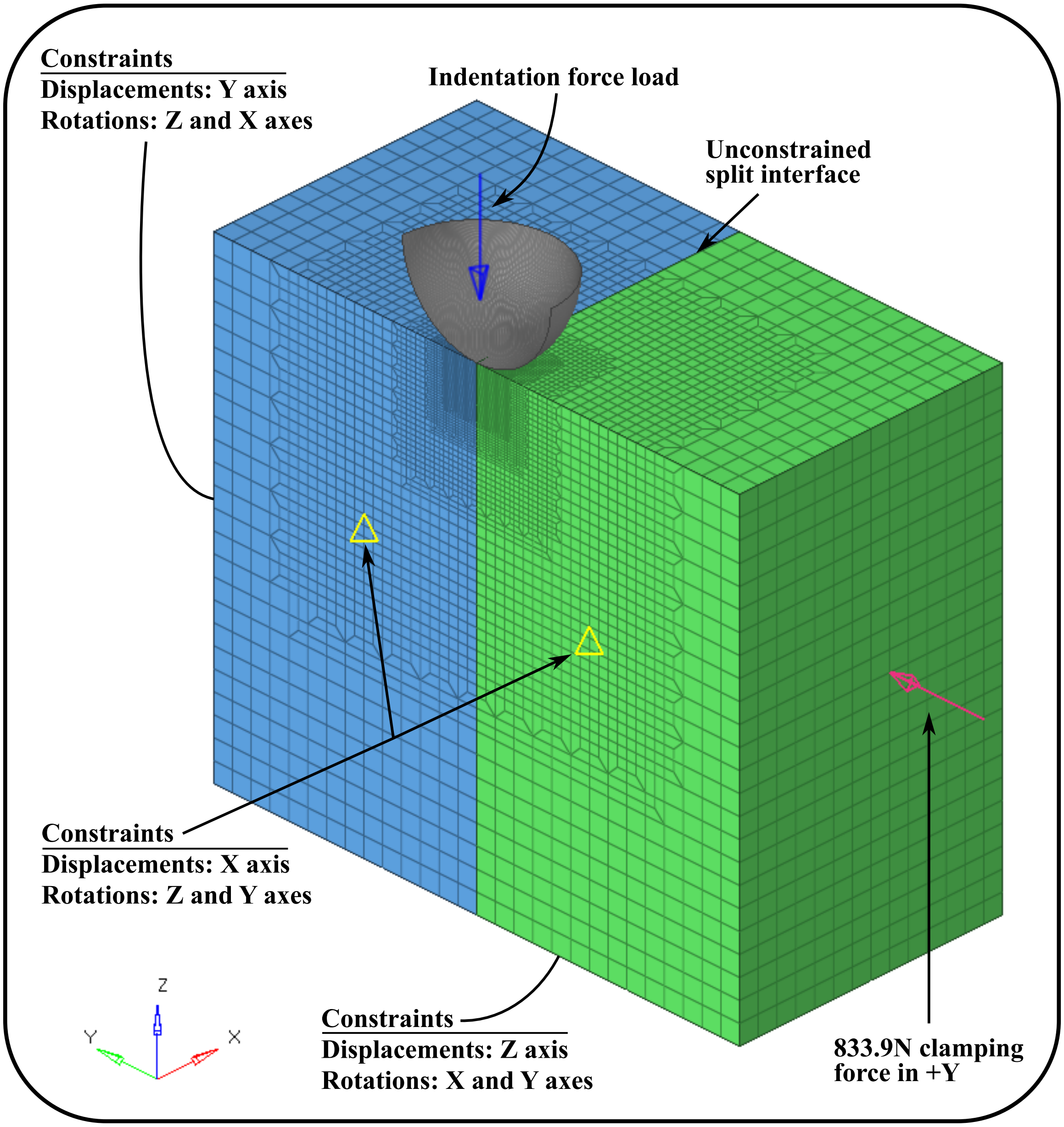

Figure 3.18: Boundary conditions of split mesh

Chapter 4

Results and Discussion

As the circular grid analysis method has been historically used on the surface for sheet metal fabrication, it has proven reliability in terms of residual principal strain measurements. Its current use within NBIT is different however due to the required change in circle array fabrication as well as the circles being on an internal surface which is in continuous contact with an opposing surface during the indentation process. Therefore, a preliminary study on the measurement accuracy of the circles as well as the integrity of the circles from an indentation can be conducted, for which a sample of AISI 4340 steel was created. This sample was a standard homogeneous sample where the top surface was polished. A FIB array was placed on the polished surface and a 981.0N indentation was conducted on the array. This experiment was to test the quality of the FIB results without the use of the vice, or split interface interfering with the material response. The top surface after indentation is shown in Figure 4.1 which shows the FIB arrays and how the major and minor axes were measured. These measurements were used for producing the residual principal strains however the center position of each circle or ellipse in relation to the center of the indentation was also measured.

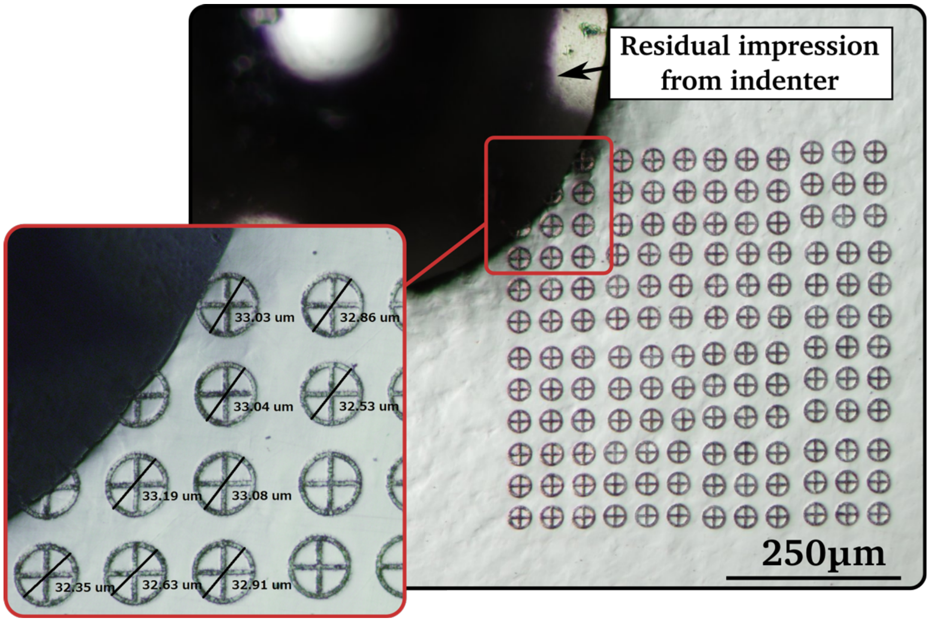

Figure 4.1: Top surface residual strain analysis showing radial distance as well as major and minor measurements

The major and minor axes were manually measured with the aid of Image-Pro software. The use of manual measurement imposes two potential sources of error. The first is that the software directly measures pixel length and then translates it to microns through certified calibrations. Therefore, there is a measurement limitation which is dependent upon the pixel density of the initial image. The average measurement error was approximately 0.3µm which translates to a strain error of ±0.02µm/µm. The second source of measurement error is that the current manual measurement of the major and minor axes rely on the ability of the researcher to determine exactly where the true major and minor axes are positioned. Therefore, due to human error the true length cannot be guaranteed to be the quantity measured. The strain error imposed from this human measurement is approximately ±0.02µm/µm as well. Therefore, the total estimated error caused by the manual measurement is about ±0.04µm/µm.

The reported measurement error could likely be greatly improved by using an automated system such as a digital image correlation method. As the circular grid analysis technique is an existing method used in industry, there exist such image correlation methods however, the small scale of the circles used in this work may be the limiting factor. If such methods are implemented however then this improved method could automatically detect the true major and minor axes and give their respective dimensions which could significantly reduce the imposed error caused by human involvement and reduce image processing time significantly. For the current work it should also be noted that because the strain is calculated via the natural logarithm, the smaller the calculated strain values correlate to a larger potential error.

To compare the results from this experiment, a quarter homogeneous FE model was used to simulate a 981.0N indentation. The resultant top surface can be seen in Figure 4.2. This figure shows large residual strains within the indentation however once outside of the contact area, the residual strains are small in comparison where they range from 0.025 at a radial distance of 400µm to zero as the radial distance approaches 1000µm.

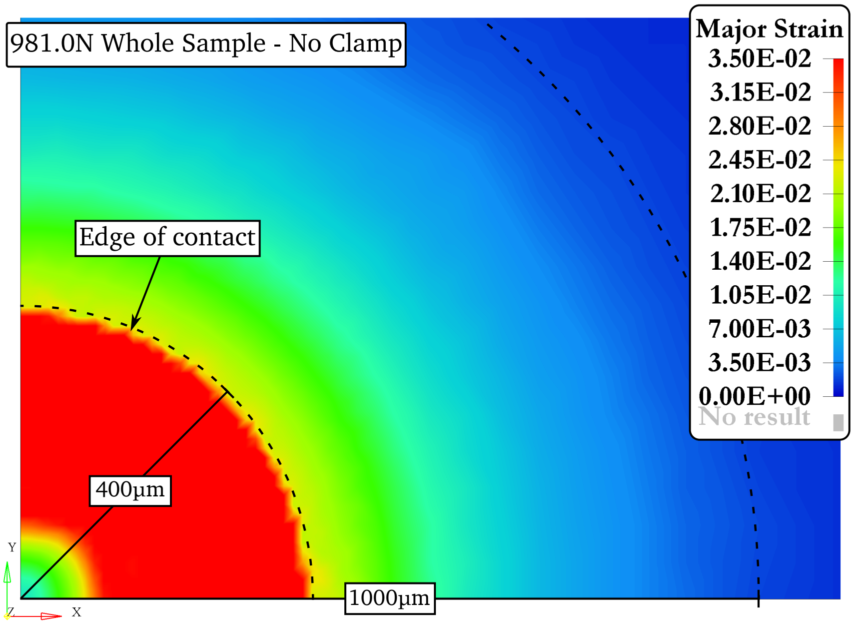

Figure 4.2: FE result showing residual major strain of top surface from a 981.0N indentation

Due to the axisymmetric nature of an indentation test on a homogeneous sample, all the elements on the surface can be used for analysis by determining their radial distance from the center of the indentation and recording the corresponding major residual strain at each location. This was also completed for the experimental results where the radial distance was measured from the center of each ellipse to the center of the indentation. At each location the residual principal major strain was recorded. The comparison between the experimental and FE results are shown in Figure 4.3. This figure starts from the edge of contact at 400µm and shows that the residual principal major strain decreases as the distance increases. From this figure it was determined that the average difference in major strain between the experimental and FE results is 0.0035 which is 54.8%. As discussed previously, the errors imposed by the manual measurements are relatively large due to the small strain values on the surface, this combined with the fact that the FE does not account for microstructural variations is why even though the percent difference is relatively large, most of the experimental data points are within the expected error range from the FE results. It should also be noted that for this top surface analysis, the pile-up effect around the indentation is not accounted for in the measurement of the ellipses. Therefore, it is possible that the first few data points true strain values could be slightly different, however the effects are expected to be negligible in comparison to the measurement error. Even so, it can be seen in Figure 4.3 that the trend of the experimental data correlates well with the FE model.

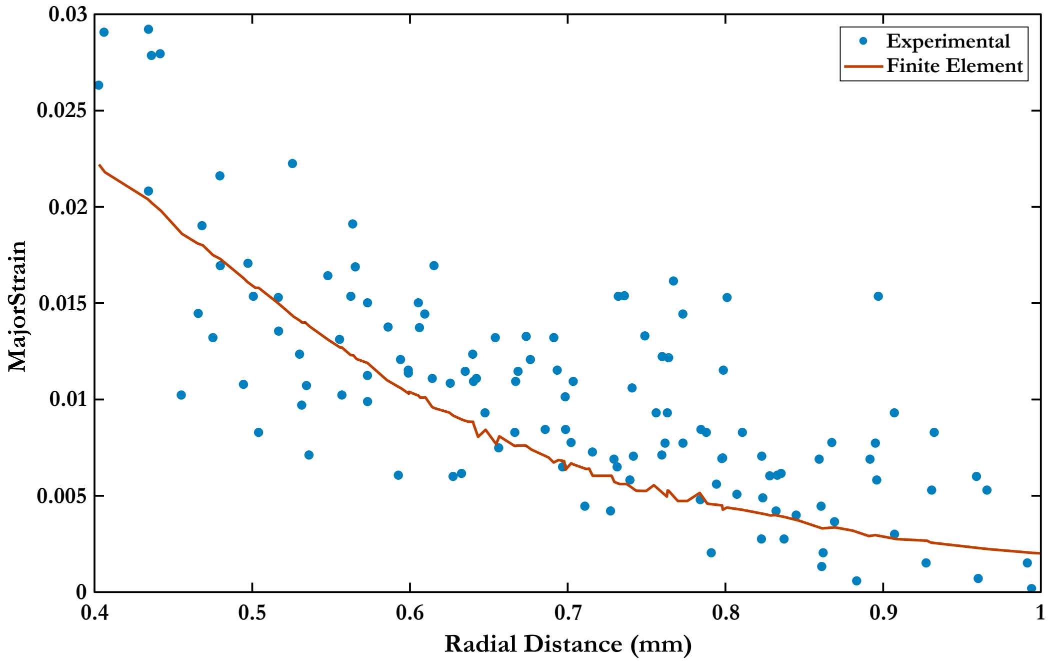

Figure 4.3: Experimental and FE major residual strain results from top surface analysis

4.1 Effect of Split Interface

The use of the split interface is one of the novel components of NBIT. To examine the effects of the split interface it is first necessary to experimentally examine the effect of the vice. For this analysis, several indentation experiments were conducted using a 588.6N normal force on a whole sample of 4340 steel with and without applied force from the vice. This is necessary as research has yet to show whether the vice itself produces any significant differences in indentation response. When comparing a homogeneous steel sample with no external force from the vice to a homogeneous steel sample clamped with a force measured to be 834N via an external force gauge, the results indicate a negligible difference in deformation. The homogeneous steel sample without an external force from the vice produced a residual indentation radius of 304.2µm. The homogeneous steel sample which had a vice force of 834N produced a residual radius of 304.5µm. This difference in residual radius is within the measurement error of ± 0.3µm. A quarter

3-dimensional model was used to replicate this whole homogeneous sample and using the experimental parameters as inputs resulted in a residual radius of 305µm. The residual indentations for these samples are shown in Figure 4.4. Therefore, since the radius of the residual indentations with or without a clamping force are within error of each other, the clamping force does not have a significant impact on the residual deformation. This can be attributed to the fact that the stress caused by the clamping force is approximately 5-6MPa which is significantly lower than the stress caused by the indentation itself.

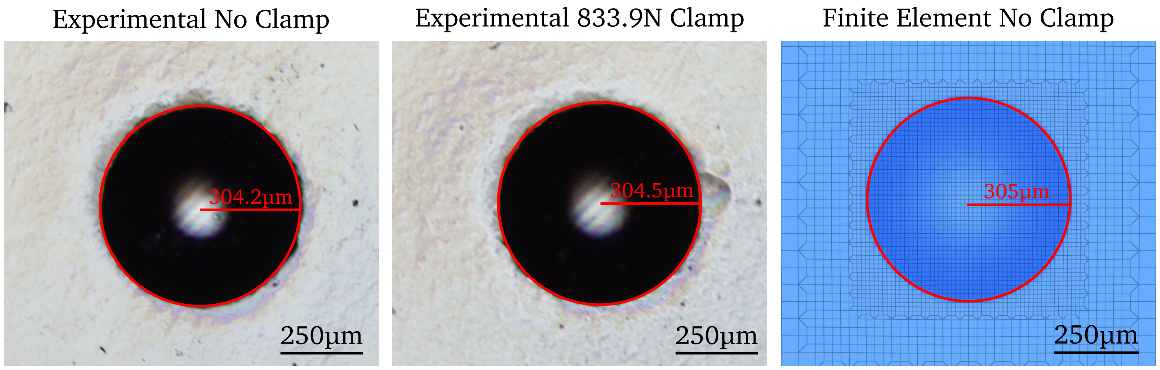
Experimental No Clamp
Experimental 833.9N Clamp
Finite Element No Clamp

Figure 4.4: Residual indentation radii comparison of experimental sample with and without a clamping force and FE sample without a clamping force

To continue the analysis on the split interface, six experimental split samples of AISI 4340 steel were created. A 588.6N indentation test using a hand tight clamping force to hold the two half specimens together was then completed. The resultant residual indentation radii were measured and by using Equation 3.4 with $t_{5,0.01} = 3.36$, a confidence interval of 304.6 ± 1.5µm was determined. By comparing the split samples to the whole samples from section 3.2.2, the null hypothesis that the population means of both experimental indentation radii were identical could not be rejected with a 0.01 significance level. This potentially means that the split and whole samples residual radii are identical.

For further comparison a quarter homogeneous FE model was used with a 588.6N indentation. This FE model produced a residual indentation radius of 305µm. This is the same value produced from the experimental samples. As the FE model and the experimental results match, this comparison indicates the split interface has little effect on the response of material deformation. To better analyze these results a quarter homogeneous FE model is compared to a clamped half non-homogeneous FE model. The residual von Mises strain within the homogeneous unclamped sample and the split clamped sample are compared and shown in Figure 4.5. From this comparison it is shown that the residual strain differs slightly in terms of the contour shape however the average difference between the split and unsplit von Mises strain below the indentation is 0.0076 or 8.97% on the split interface. The split and unsplit samples are in good agreement in terms of the residual strain however the difference in strain between the two does increase along the top surface just inside of the indentation radius.

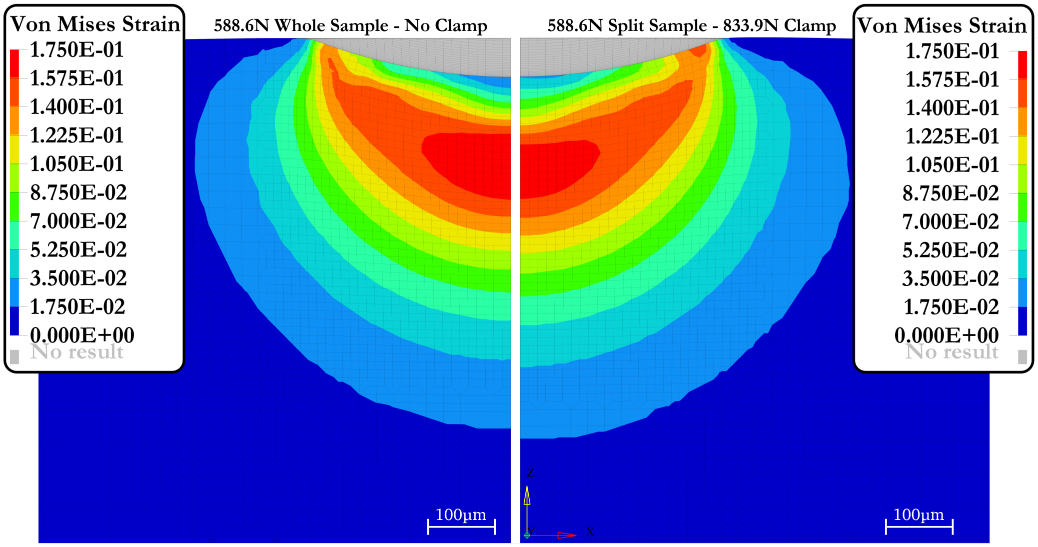

Figure 4.5: Internal von Mises strain between whole unclamped sample (left) and split clamped sample (right)

This difference in von Mises strain inside of the indentation radius along the top edge can be better understood by examining the perpendicular displacements of the split interface. As shown in Figure 4.6, there are positive displacements going into the material sample which allow for the interface to separate. This separation is small with a maximum separation distance of 1.92μm, and as also shown in the figure, the separation is localized in that one region. The majority of the interface exhibits a displacement of -0.14μm which is a displacement towards the interface causing the two internal surfaces to come into contact, allowing for good energy transfer across the interface.

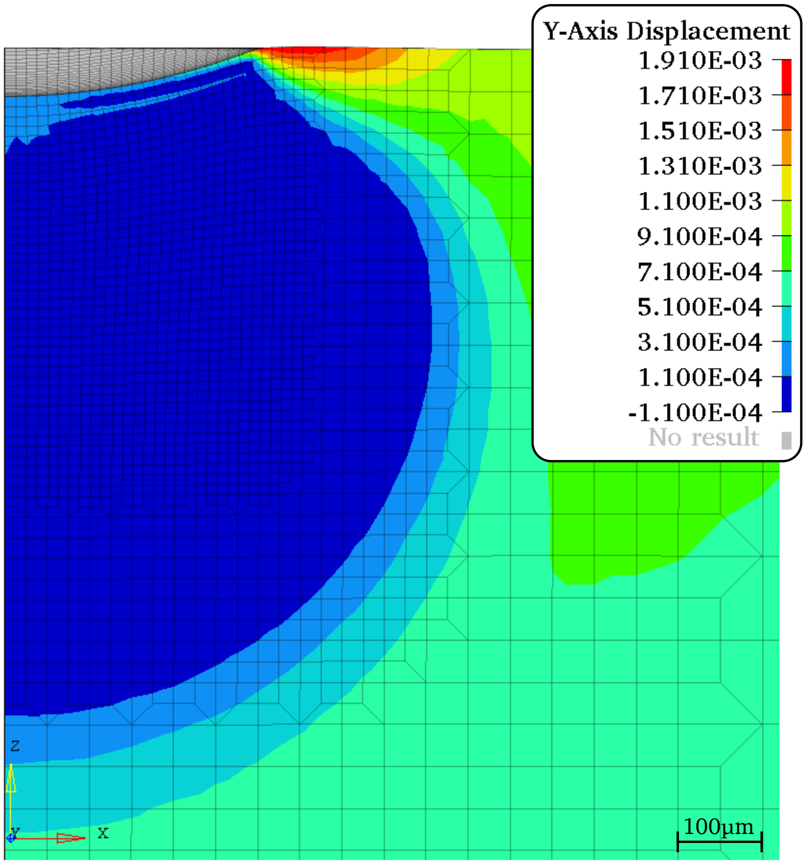

Figure 4.6: Perpendicular displacement of split interface

For further examination, the perpendicular strains can also be examined from the interface as it is expected to show the largest difference compared to a whole sample due to the free surface attracting dislocation movement [29]. Therefore, as shown in Figure 4.7 the overall strain contours are similar however the consistent difference is present shown along the top edge inside the contact zone due to the +Y axis displacements.

Even so, when analyzing the area of interest below the indentation, the average difference

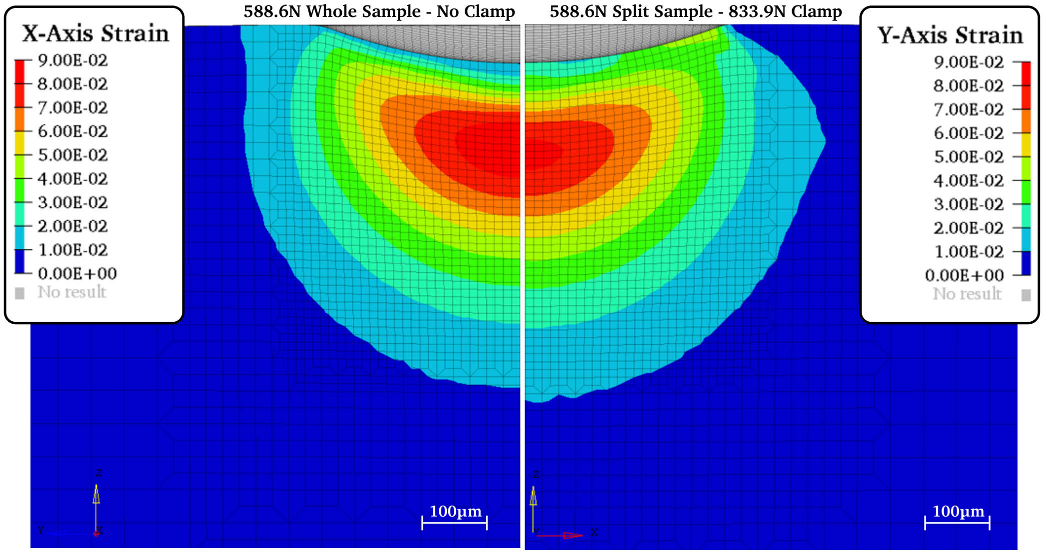

Figure 4.7: Perpendicular strain comparison between whole and split samples interface

between the whole and split in terms of strain is 0.0066µm/µm or 15.1 %. This indicates that the maximum difference caused by the split interface in terms of residual strain is 15.1%. That is however, for the strain perpendicular to the interface. A more important analysis is that of the difference in the major and minor residual strain results due to the split interface, as these results are what will be determined experimentally.

As shown in Figures 4.8 and 4.9, the overall strain contours are highly comparable with small differences such as the expected difference near where the interface separates in the split samples, as well as a slight reduction in the maximum principal strain zone below the indentation. When examining the average differences between the split and whole samples, the principal major strain has an average strain difference of 0.0031 µm/µm or 9.24 %, whereas the principal minor strain has an average difference of 0.0054 µm/µm or 7.71%.

Therefore, these comparisons show that when analyzing the experimental principal major and minor strain results, the split interface is expected to introduced a less than 10% difference when compared to a whole sample. Further confidence in this technique

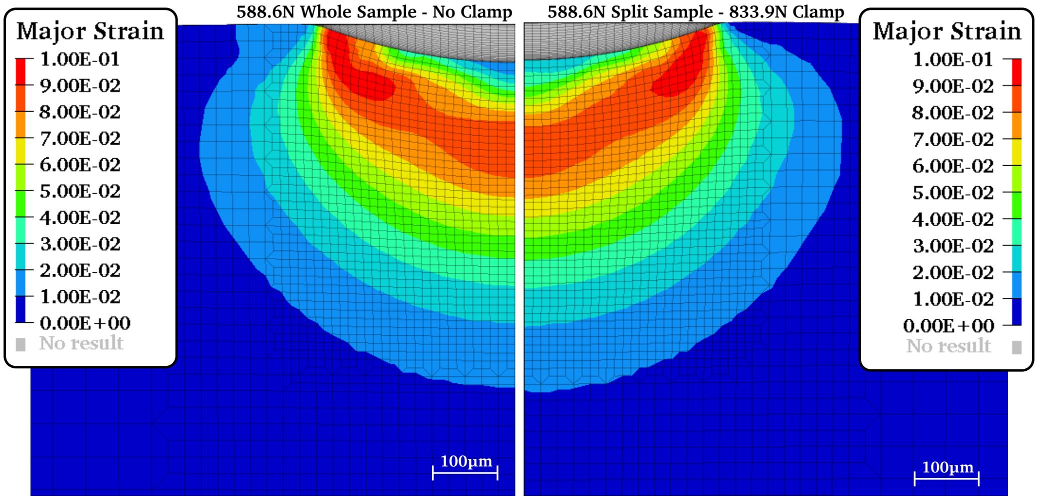

Figure 4.8: Principal major strain comparison between whole and split samples interface

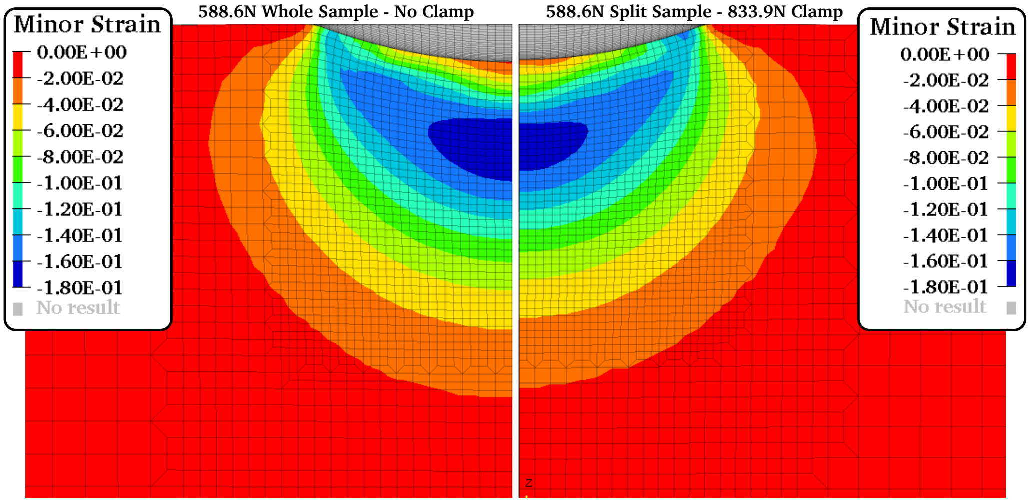

Figure 4.9: Principal minor strain comparison between whole and split samples interface

can also be achieved from analyzing the experimental displacements on the internal surface after an indentation occurs, and using a quarter homogeneous FE model as a comparison. To achieve this analysis an experimental split sample was subjected to a 588.6N indentation along the split interface. After indenting the vice pressure was removed, and the two halves were then separated. The internal surface before and after deformation is shown in Figure 4.10. This figure shows the FIB array before and after indentation and contains an outline of an undeformed circle before indentation on the left and the same circle after indentation where it becomes an ellipse on the right. Prior to indentation the surface on the left is shown to be smooth with undeformed circles created via the FIB. After the indentation was completed the circles within the plastic boundary become deformed into ellipses.

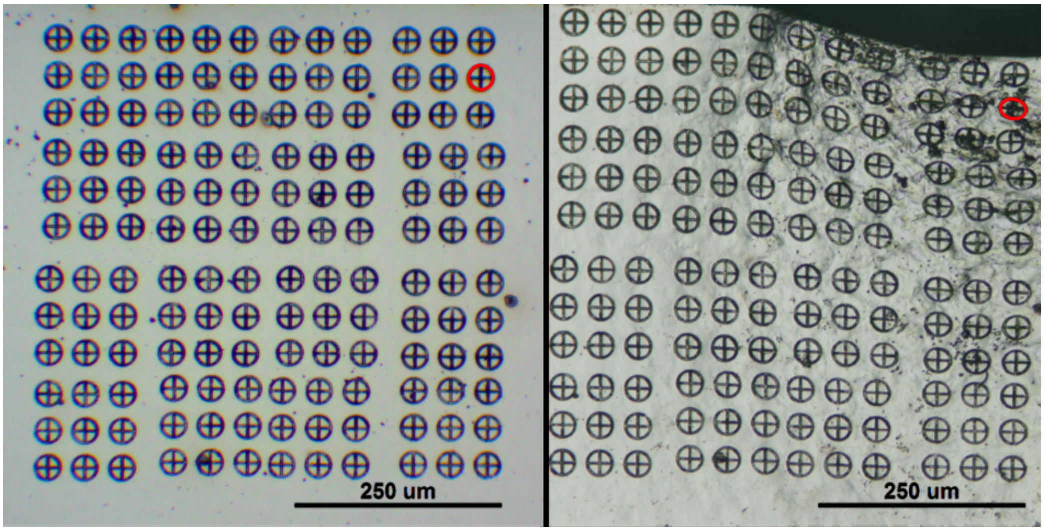

Figure 4.10: Optical micrograph of the FIB array before (left) and after (right) a 588.6N indentation load

Due to the relatively small plastically deformed area from the 588.6N indentation, several circles remained undeformed as well as maintained their original positions. Using these circles as reference points, the center positions of all the circles before and after the indentation can be determined and used for creating a displacement field. This experimental displacement field can then be compared to the simulated results as shown in Figure 4.11. This figure is a composite image with three separate layers. The optical micrograph from after the indentation shown in Figure 4.10 is used as the base layer on the left. The experimental displacement point data results are used as a top layer over the base circular layer indicating the physical relationship between the point data to the experiment. The final layer is the FE displacement results on the right side where the color of the FE and experimental point data use the same color mapping. This comparison between the experimental and FE model produced an average difference in displacement of 3.92μm.

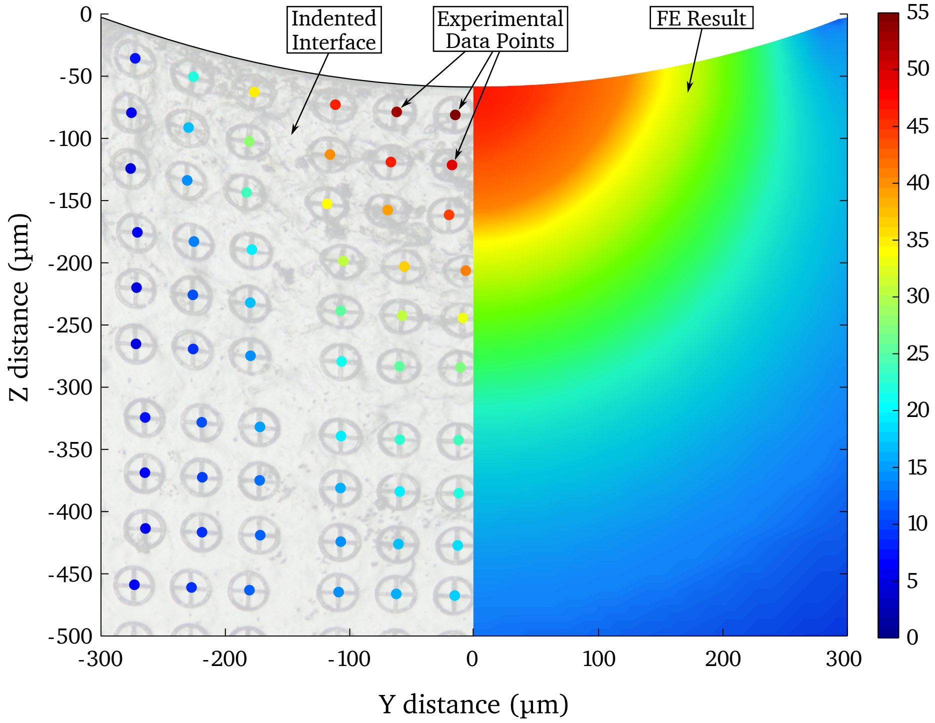

Figure 4.11: Internal surface composition of experimental displacement point data with FE results

The average displacement difference can be better examined by looking at the circular gird and analyzing the percent difference between each individual circle as shown in Figure 4.12. This figure contains two plots where the plot on the left measures the percent difference between each experimentally displaced circle and the corresponding location from the FE results. The percent difference results are then color mapped where a difference of less than 25% is blue, less than 100% is orange, and greater than 100% is red. The percent difference is then plotted against the circles distance from the indentation center. The plot on the right is simply the center point locations of each circle within the deformed array however the circles maintain their respective color map from the plot on the left. From this figure it is shown that the percent difference between individual circles can be higher than 200% however when isolating specific difference groups the circles which maintained the smallest percent difference are within the area of interest beneath the indentation giving rise to an increase in confidence for this method.

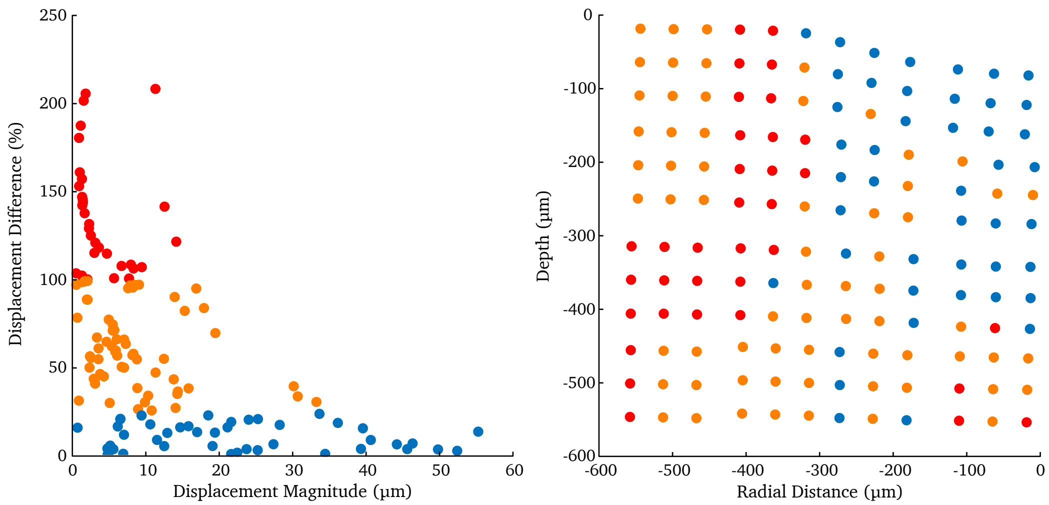

Figure 4.12: Internal surface composition of experimental displacement point data with FE results

4.2 Internal Residual Strain

In this section the internal strains using the FIB circles will be analyzed and compared to the FE results using loads of 588.6N, 981.0N, and 1471.5N. The basic results of these simulations are shown in Table 4.1 to show the non-constant difference between the experimental and FE results from the various indentation loads.

From the indentation load however, the resultant major and minor principal strains were

Table 4.1: Summary of experimental and FE results for residual diameter and depth

Force	Radius (μm)			Depth (μm)		
	FE Model	Experimental	% Diff.	FE Model	Experimental	% Diff.
581.6N	305	304.7	0.1	53.5	60.7	11.8
981.0N	384	377.7	1.7	86.9	87.7	0.9
1471.5N	462	465.2	0.7	128.4	153.8	16.5

determined by measuring the major and minor axis. A MATLAB script was created which used the center point Y and Z value of the FIB circles and found the closest element centroid location from the FE results. Once the identical location was determined between the experimental surface and the FE surface, the major and minor strain values at that location were compared.

4.2.1 Low Indentation Force (588.6N)

By using optical microscopy, the major and minor axes of each circle were measured. These values were compared to the FE results as shown in Figures 4.13 and 4.14. These figures are comparable to Figure 4.11 however instead of comparing displacement data, they are comparing residual principal major and minor strains. Figure 4.13 shows the shape of the FE and experimental strain contours are similar. There is low strain directly beneath the indenter, which eventually increases and then decreases again as the depth increases. For the major strain, Figure 4.14 shows that both the FE and experimental results have the maximum major strain occurring near the residual contact edge as well as a low residual major strain directly beneath the center of indentation. As both the major and minor residual strain data in general correspond well with each other, indicating that the use of the vice and split interface can be used as a representative for a whole unsplit specimen.

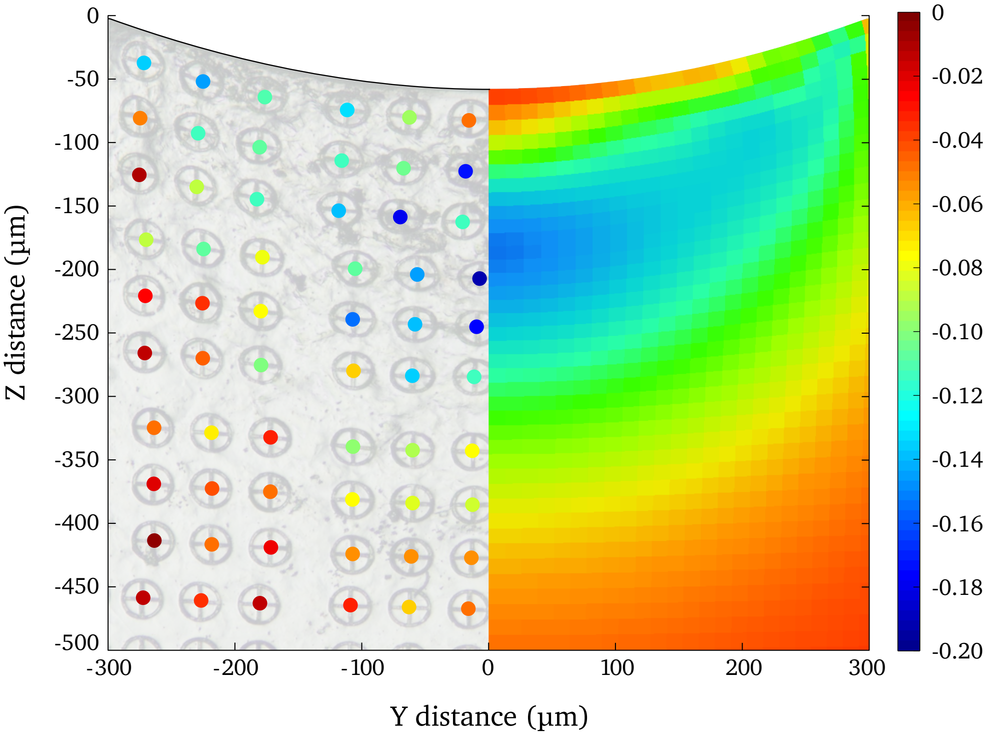

Figure 4.13: Experimental minor strain point data compared to FE minor strain results from a 588.6N indentation

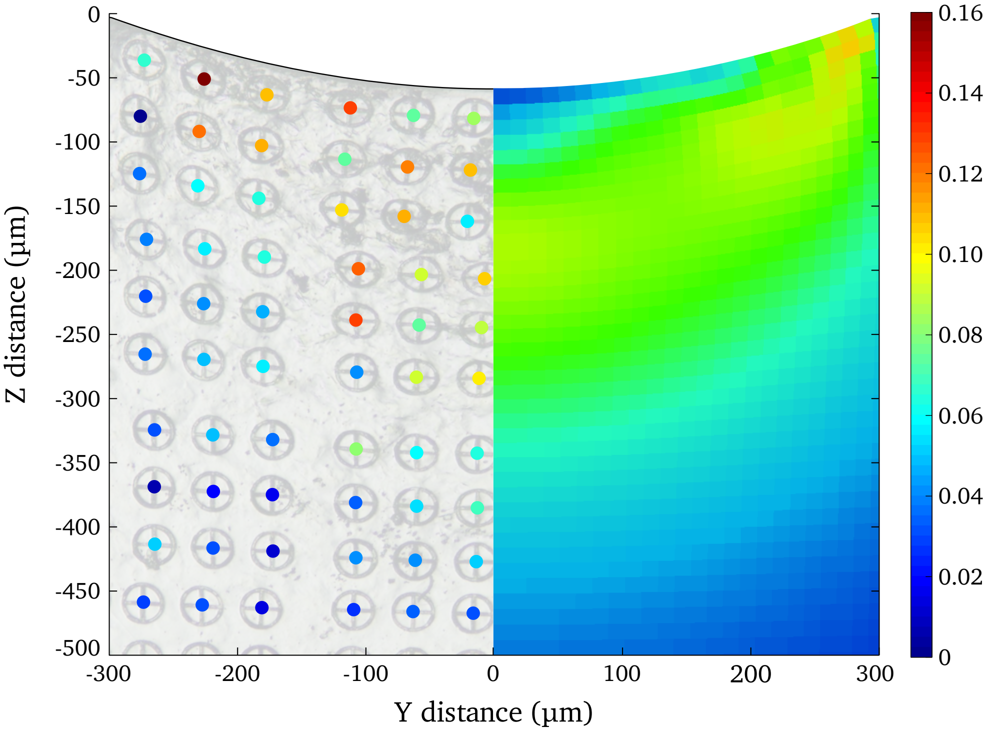

Figure 4.14: Experimental major strain point data compared to FE major strain results from a 588.6N indentation

Although the shape of internal strain fields show good agreement, the exact values are difficult to compare when viewing the entire surface. An analysis of the data points that lie along the Z axis can be examined as well to show how strain changes with increasing depth as shown in Figures 4.15 and 4.16. These figures show the major and minor strains respectively for the FE split, FE whole homogeneous, and experimental samples. The FE split and FE homogeneous trends from both residual major and minor strain show good agreement. The experimental results follow similar trends, however some individual data points show large variations. The average difference between the experimental and simulated results were 0.015 or 53.72% for the major strain and 0.017 or 28.5% for the minor strain.

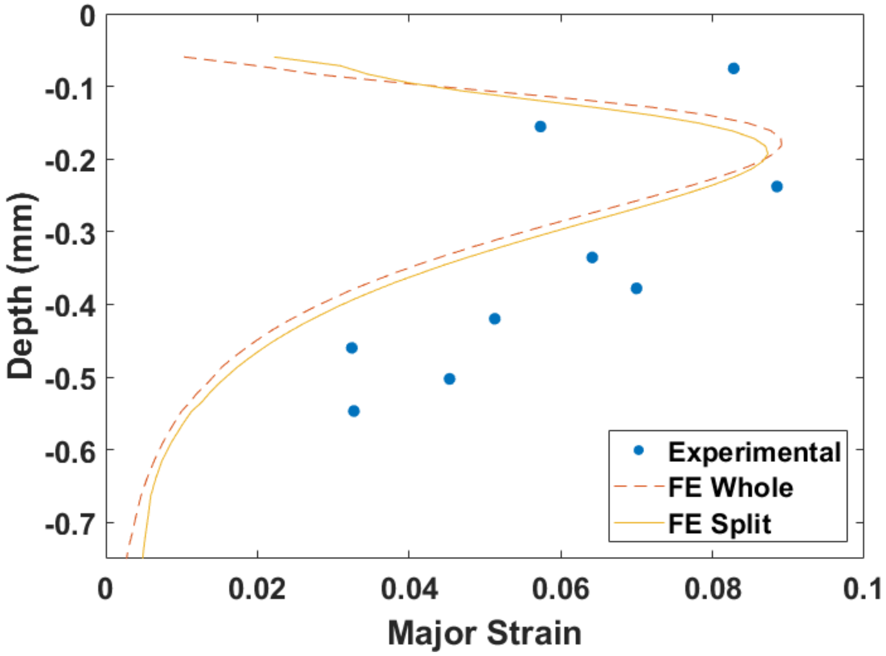

Figure 4.15: Residual major strain as function of depth for experimental and FE results from a 588.6N indentation

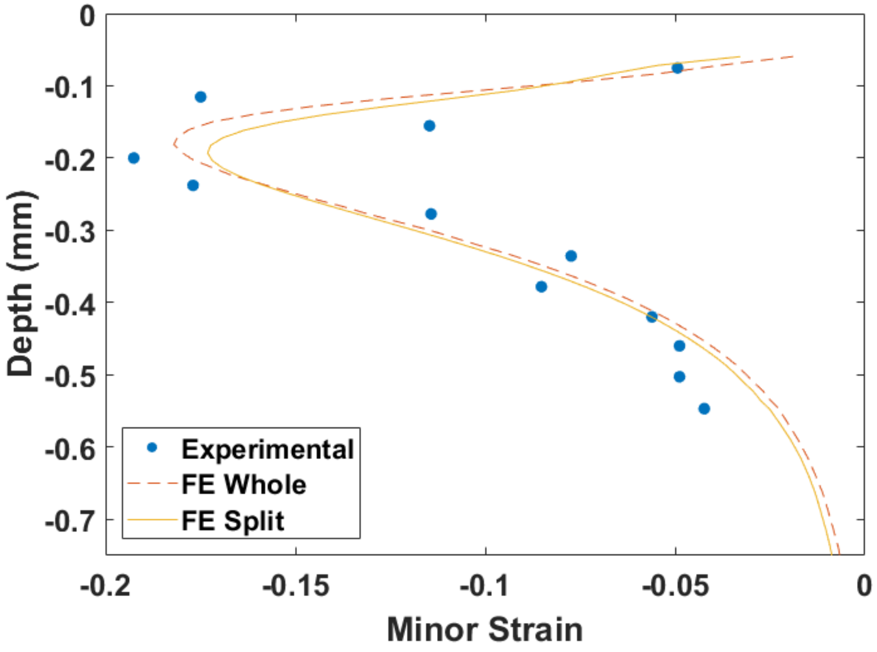

Figure 4.16: Residual minor strain as function of depth for experimental and FE results from a 588.6N indentation

From Figures 4.13 - 4.16 there are some outlying experimental data points that do not correspond well when compared to the FE results. Some of these discrepancies heavily attribute to the large difference in the major and minor strain results. To investigate these large discrepancies in strain values the 588.6N experimental sample was etched with a 2% nital solution to examine its microstructure as shown in Figure 4.17. This micrograph shows the deformed ellipse is mainly in a pearlite grain however there are sections of the ellipse which are irregularly deformed and are within ferrite grains. The irregular deformation is shown to be attributed to the non-homogeneous material response between the two compositions. This irregular deformation causes the manual measurements of the major and minor axes to become skewed and is believed to be the main reason for the large discrepancies between the experimental micro and FE macro strain results. For further examination, a similar analysis was completed using a 981.0N indentation force.

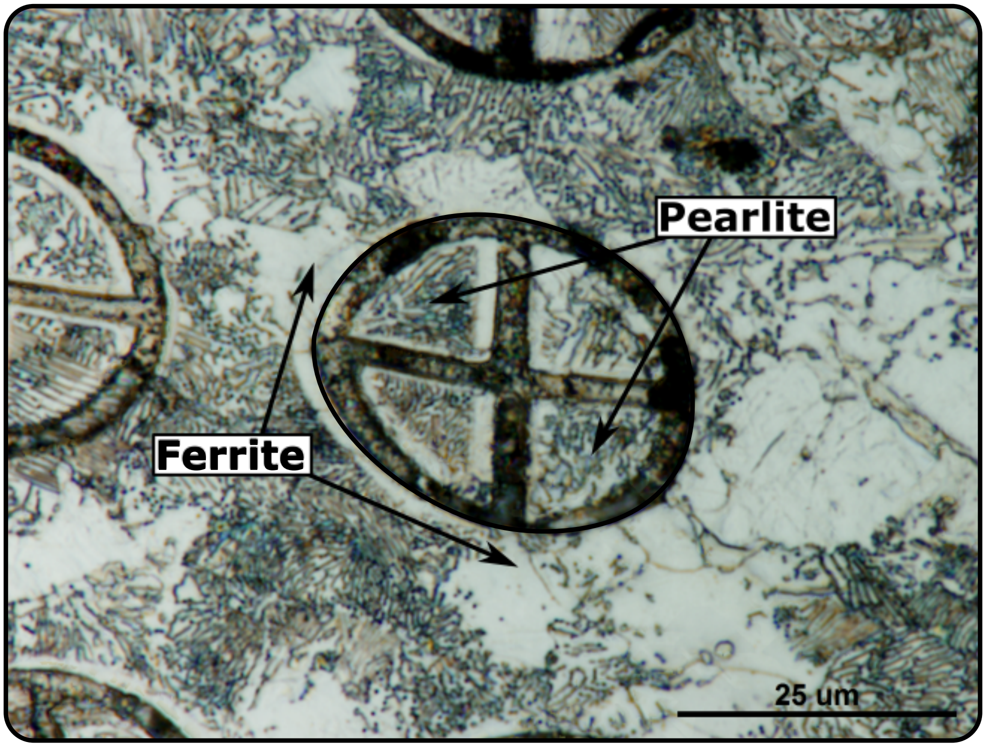

Figure 4.17: Microstructure of substrate showing non-uniform deformation of ellipse in 588.6N sample

4.2.2 Medium Indentation Force (981.0N)

By increasing the indentation force to 981.0N, the amount of internal deformation will increase as well. This increase in internal deformations should give rise to an increase in recorded residual total strain values. By following the same analysis as the 588.6N sample, the residual total strain comparison between the experimental and FE results are shown in Figures 4.18 and 4.19, which show the residual principal minor and principal major strain comparison respectively. From Figure 4.18 it is shown that the areas of highest strain are similar between the experimental and FE where they decrease at approximately the same rate with increasing distance from the indentation. Figure 4.19 did not produce as good a comparison as the 588.6N load case. The color mapping appears to be fairly sporadic showing large major strain values which do not correlate well with the FE model. In terms of exact comparisons, the residual minor strain produces a difference of 0.0427 or 34.81% whereas as the residual major strain produces a difference of 0.0264 or 69.94%.

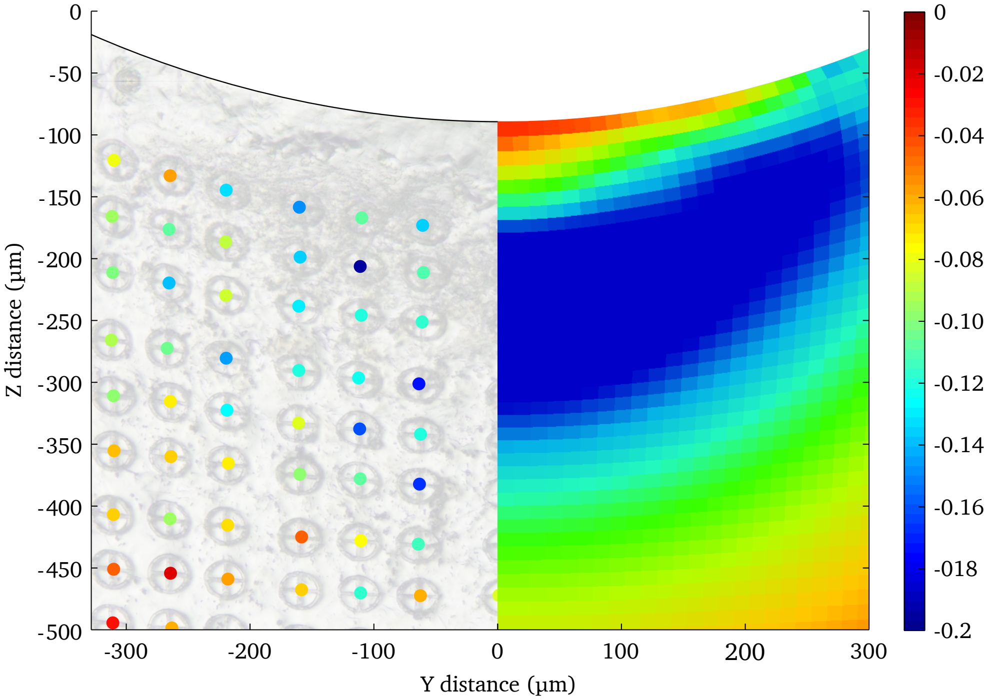

Figure 4.18: Experimental minor strain point data compared to FE minor strain results from a 981.0N indentation

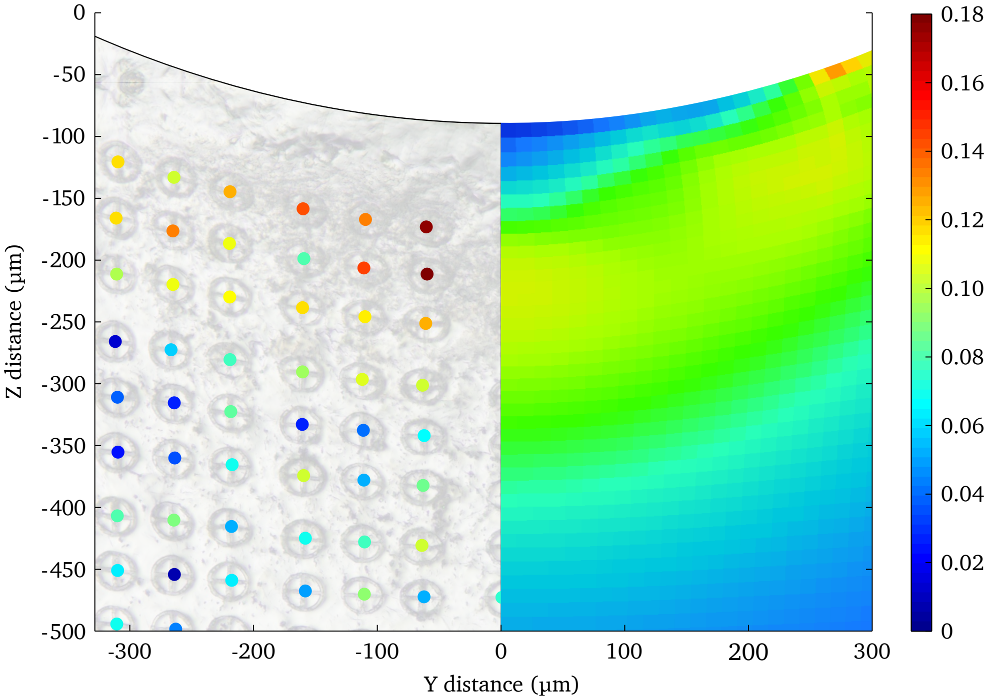

Figure 4.19: Experimental major strain point data compared to FE major strain results from a 981.0N indentation

These differences between the experimental and FE analysis are larger than the differences seen from the 588.6N indentation. The reasoning for this increase in difference can be attributed to the increase in deformations caused by the increase in indentation force. As seen in Figure 4.17 the 588.6N indentation caused variances in the thickness of the ellipse lines as well as variances in the uniformity of the ellipses. Therefore, it can be said that by increasing the deformations, the residual strains within the softer ferrite grains will be even higher and therefore cause even further non-uniformity within the measured ellipse. This can be examined much like Figure 4.17 where the surface of the 981.0N indentation was etched using the nital solution and the resultant microstructure around the deformed ellipse is shown in Figure 4.20.

From this micrograph, the resultant deformation is as expected such that the portion of the ellipse which is in the ferrite grain is exhibiting an increase in deformation as compared to the pearlite section of the same ellipse. This non-uniformity between the

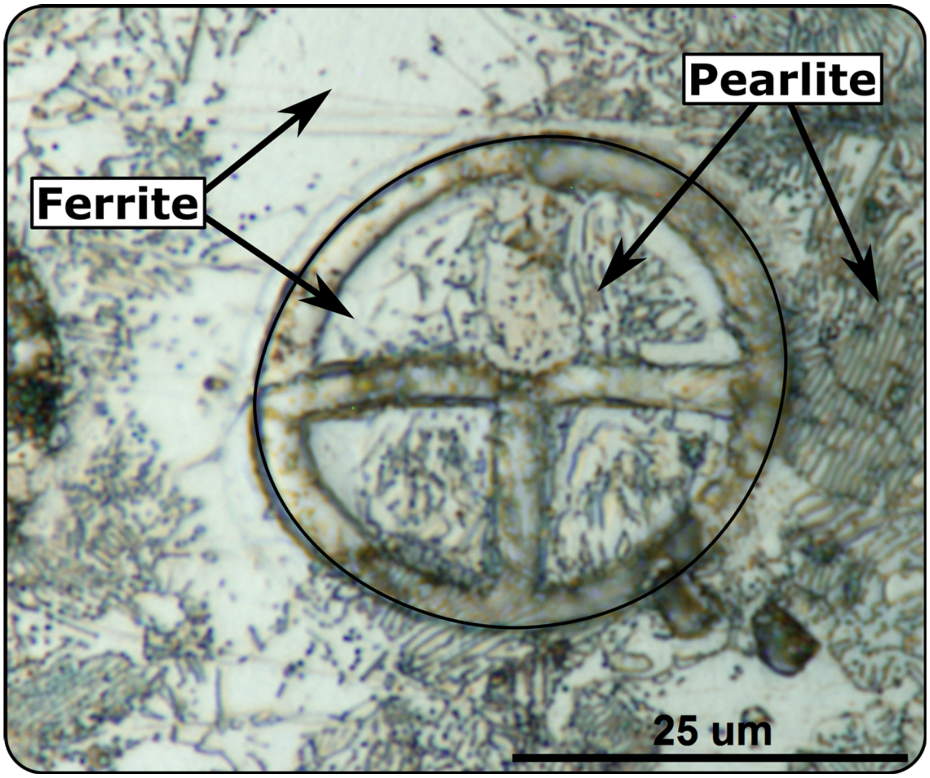

Figure 4.20: Microstructure of substrate showing non-uniform deformation of ellipse in 981.0N sample

microstructural phases is the cause of these large discrepancies and as such, it is expected that they will increase by using additional force during the indentation process.

4.2.3 High Indentation Force (1471.5N)

As the Buhler hardness tester is limited to a maximum indentation force of 1471.5N, this is the highest force able to be utilized for this current work. Based on the previous experimental results, the 1471.5N indentation should produce even greater internal deformations which should result in an even greater difference between the experimental and FE results. These comparisons are shown in Figures 4.21 and 4.22 which show the comparisons between the experimental and FE principal minor and principal major strains respectively. From these figures an area absent of data is present which is due to the measurements not being taken promptly, which allowed for 7 circles to be lost due to corrosion. The remaining 137 circles were able to be measured however and used for the comparisons. From these comparisons, the average difference from the minor comparison is 0.0370 or 25.99% and the difference from the major comparison is 0.0301 or 38.83%.

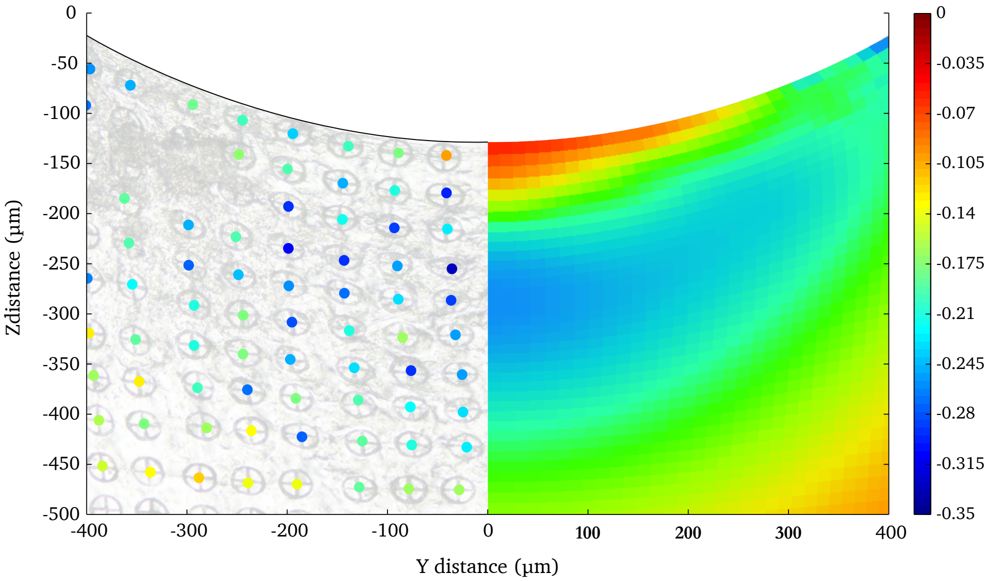

Figure 4.21: Experimental minor strain point data compared to FE minor strain results from a 1471.5N indentation

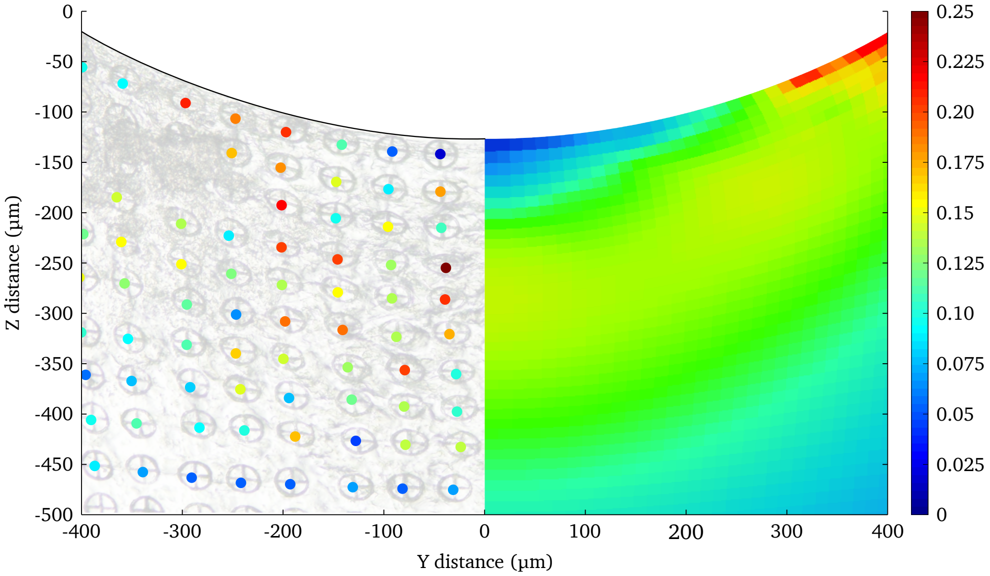

Figure 4.22: Experimental major strain point data compared to FE major strain results from a 1471.5N indentation

Table 4.2: Summary of experimental and FE differences for major and minor strain

Force	Minor		Major	
	Difference	% Difference	Difference	% Difference
581.6N	0.0167	28.51	0.0153	53.72
981.0N	0.0427	34.81	0.0264	69.94
1471.5N	0.0370	25.99	0.0301	38.83

Comparing these results to the 588.6N and 981.0N indentation results all summarized in Table 4.2, the largest indentation force shows a high strain difference, but the lowest percent difference between the experimental and FE results. The reasoning for this is thought to be because of several different factors. First, there is little to no repeatability done with this study on the internal strain, and therefore the average results may vary. Secondly, the error from the manual measurement method can cause large variations in the recorded value as seen in Figure 4.23. The curves shown in Figure 4.23 show the minor and major strain values below the center of the indentation, where they would ideally be a smooth line. This is not the case however due to the measurement error, where it is clear that the curves have significant noise. Thirdly, the difference in mechanical properties between the ferrite and pearlite would also become much more apparent under an increasing indentation force. As the indentation forces increase, the deformation of the ferrite is significantly higher compared to the pearlite which is why the ellipses become non-uniformly deformed. The resultant deformation of an ellipse from the 1471.5N indentation is shown in Figure 4.24. This increasing deformation of the ferrite grains appears to be the case up to and including the 1471.5N indentation, however, from the 1471.5N results, the pearlite could also now be deforming sufficiently to reduce the phase dependent deformations. The use of the FE model as a comparison also causes some issues especially with the difference in displacement being 25.4μm for the 1471.5N indentation. As the FE strain results are first dependent upon the resultant displacements, the difference could be because of the chosen material model parameters.

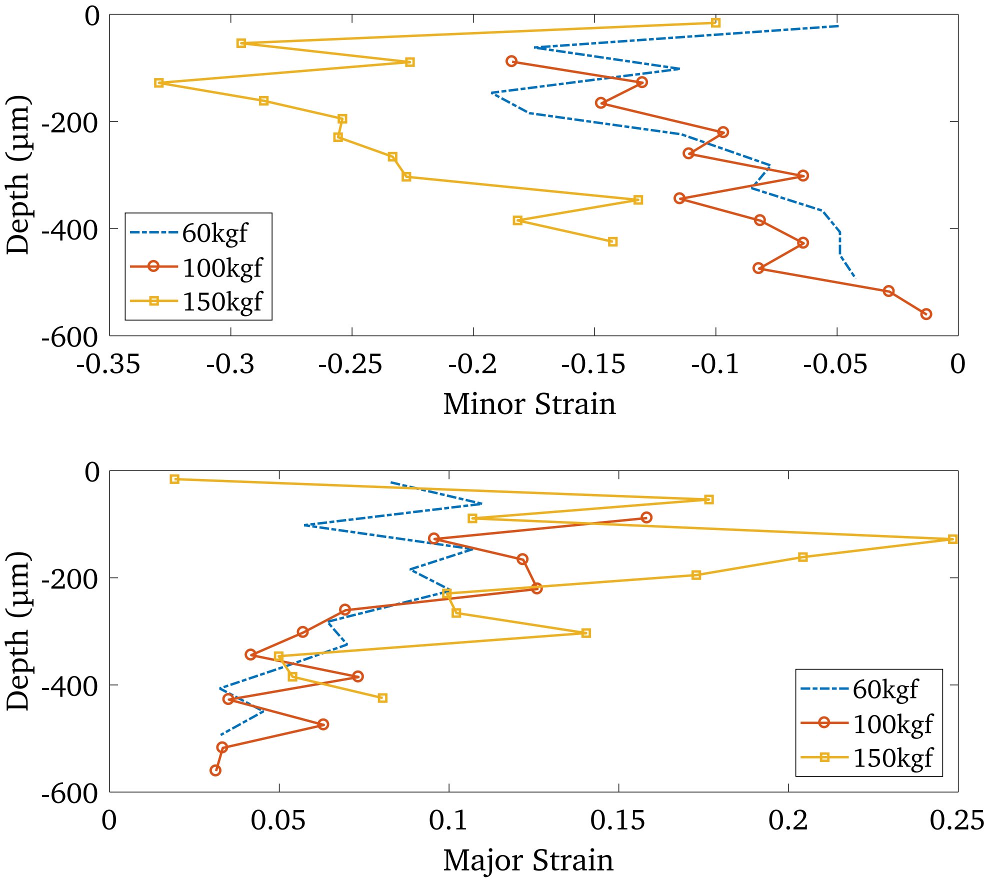

Figure 4.23: Centerline residual major and minor strain results for separate indentation forces

Even with all of these potential differences between the experimental and FE model the percent difference is continually decreasing with increasing force and is explained simply by the fact that the strain difference is not increasing linearly with the amount of strain in the sample. Therefore, when determining the percent difference between the experimental and FE analysis, the amount of influence that the strain difference has on the recorded strain value is decreasing with increasing indentation force. It should also be noted that from Table 4.2, the strain difference between the experimental and FE results stay within the approximate measurement error of ±0.04 with the exception being the minor strain difference from the 981.0N sample. From this result the 981.0N

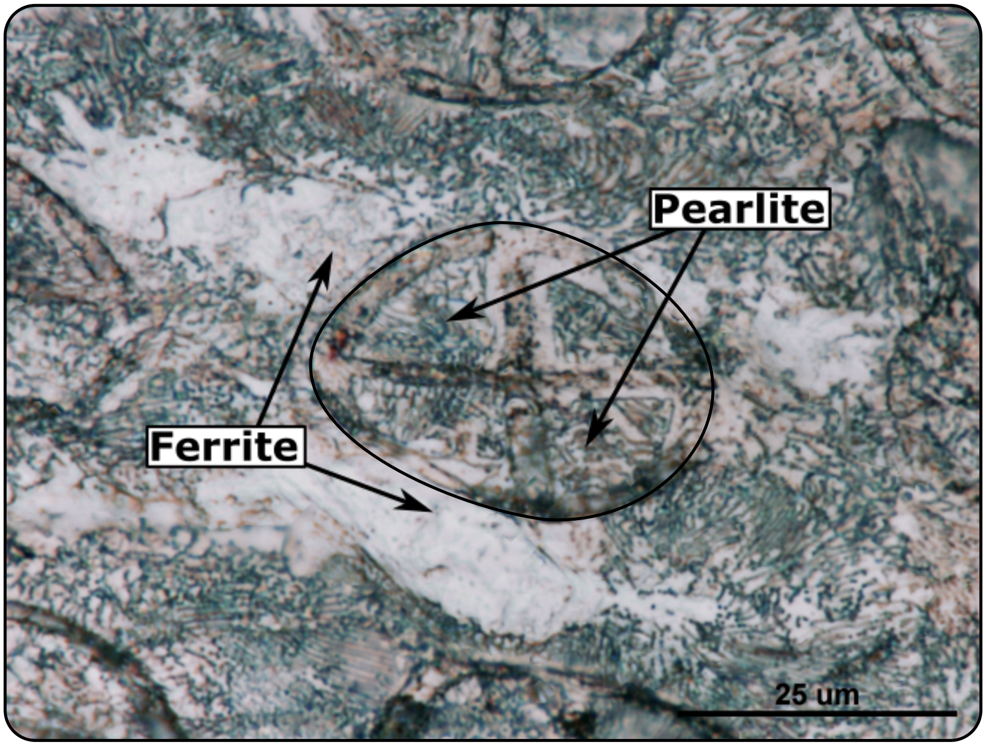

Figure 4.24: Microstructure of substrate showing non-uniform deformation of ellipse in 1471.5N sample

sample was reviewed further where it was found that several individual circles from that sample were measured to have vastly differing strain values and therefore the large difference was found to be a combination of the microstructural differences as well as the differences caused by manual measurement.

Although the focus from these comparisons has been on the strain and percent differences between the experimental and FE results, they are not the sole determining factor of the effectiveness of this method. As it has been shown that the split interface causes minimal difference in the residual strain along the split surface, the comparisons serve as a rough affirmation towards the confidence in the experimental results. This is because as previously discussed, the FE model is useful for determining the macro strain results that are not dependent upon any form of microstructural inhomogeneity. Therefore, NBIT results are expected to not compare well especially with the use of a multi-phase material where the mechanical properties of the separate phases will heavily influence the local micro strains within the sample.

Chapter 5

Conclusions

The measurement of residual strain is an important analysis technique for determining the amount of deformation and where failure may occur within a material. There are currently a diverse number of measurement techniques; however, as the technology in materials science improves, the requirements for even finer residual measurements will be imperative. Therefore, the purpose of this work was to use the novel method of NBIT for determining residual microstructural deformations and residual strain distributions, create a non-linear validated FE model to determine the effects of the split interface, and compare the analytical and experimental results to the FE model for three separate indentation loads.

As the first objective of this work was to investigate the novel method of NBIT, several experiments were conducted using the focused ion beam (FIB). These experiments were conducted in order to determine the optimum process parameters for analyzing the resultant residual strain along the free interface. The optimum process parameters were determined to be a beam spot size of 0.248μm/px, a dwell time of 128μs, and a frame count of 150. Using these process parameters allowed for the comparison between the top surface experimental and FE results. From this comparison it was determined that the circles created via the FIB could be utilized for determining the major and minor residual strains from an indentation test. This comparison also gave rise to the issue of measurement accuracy where the small strain values outside of an indentation along the top surface are small enough to become significantly effected by the measurement accuracy. It was still determined however that the general trend of the residual top surface strain compares well between the experimental and FE model. Therefore, the general use of the FIB circles for use in residual strain analysis was investigated.

The second objective of this work was to create an accurate and experimentally validated FE model which can be used for the analysis of the split interface. To be able to complete this final analysis of the split interface, the FE model had to go through several development stages. The finite element model was first created as a whole homogeneous model which was quartered and simplified using symmetry boundary conditions. Proper element size was determined through an analytical comparison to the Hertzian model, using the parabolic pressure distribution in place of an indenter. An indenter was then added to determine the proper contact algorithm to reduce the amount of indenter-substrate interpenetration. After the contact algorithm was determined, the model was then changed to the use of the Johnson-Cook elastic-plastic material model. The parameters for which were determined through experimental comparisons and were determined to be the parameters first determined by Rule [79]. Once the optimal parameters were determined and the quarter model was validated via the experimental results, a half model was then created.

Prior to analyzing the split interface, the effect of the vice had to be examined. To do so, two whole samples of AISI 4340 steel were indented using a 588.6N indentation load. One sample was clamped with a force measured to be 833.9N, while the other sample was not clamped. The residual indentation radii of which were examined and produced values of 304.7μm and 304.2μm for the clamped and unclamped samples respectively. These results were also then compared to a homogeneous FE model using a 588.6N indentation load without any clamping force where the FE model had a residual indentation radius of 305μm. From this it was determined that the clamping force from the vice produced an approximately 5-6MPa which is significantly less than stress caused by the indentation itself, and therefore the vice produces negligible difference in the results.

For analysis on the split interface the results from the FE half model were compared to the FE quarter model. The comparison of the internal von Mises residual strain found a difference of 8.76%. The internal residual Y-axis perpendicular strain was also compared for examining the differences caused by the free interface. The perpendicular analysis found that the overall trend was fairly similar however the half model produced slightly lower values with an average difference of 0.0066μm/μm or 15.1%. The effect of the interface on the residual principle major and minor strain was also examined and found that the split interface caused a difference of 0.0031μm/μm or 9.24%, and 0.0054μm/μm or 7.71% for the major and minor strain respectively. As the strain difference is relatively low at less than 10% especially for what will be measured experimentally, and the overall trend within the split interface is a good comparison to the whole model, the interface can be said to produce little difference in the material response.

The third and fourth objectives were to compare these FE results with the experimental results using the FIB at three separate loadings. The experimental samples used for this analysis were composed of AISI 4340 steel and were created with two separate dimensions. The first set of samples were perfectly cube and used as a homogeneous sample. The second set of samples initially had the same dimensions as the first except that they were then split in half. Circular arrays were placed on the internal surface of the split samples. This array was created via a focused ion beam for which the optimal parameters were also determined. One parameter which was kept constant was the diameter of the individual circles. This was kept constant to have a consistent resolution as well as simplify the overall experimental method. If desired however, this circular placement method has the capability of placing circles on the single or sub micron scale and therefore, allows NBIT to have one of the most diversified measurement resolutions compared to other methods.

The first experiment conducted was a continuation of the split interface analysis where the experimental homogeneous and split samples were compared in terms of their residual indentation radius. Six split samples were analyzed, and a hypothesis test was conducted at a 0.01% significance level and determined that the population means of the homogeneous and split samples residual radii could be the same, further continuing the conclusion that the split interface causes minimal change in the material deformation.

The second set of experiments conducted for this work utilized the circles which were used for measuring the amount of residual total strain. The use of circles allowed for the measurement of both the principal major and principal minor strain values. The measurements of which were completed via an optical microscope with an approximate strain error of ±0.04μm/μm. This experimental indentation was done via a hardness tester with various loadings of 588.6N, 981.0N, and 1471.5N. The experimental split samples were compared to the homogeneous finite element model in order to compare the effect of the split interface on the residual strain values. Indentation forces of 588.6, 981.0, and 1471.5N were used and the standard circular grid analysis method was used to present the internal residual strain from each of the indentation forces. The 588.6N experimental split sample was used to create a displacement field which produced an average difference of 3.92μm when compared to the FE homogeneous sample. The residual strain results from this work compared the micro scale experimental strain results from a split sample to the FE macro scale strain results from a homogeneous sample. This comparison showed a difference in internal residual minor and major strain of 28.5% and 53.7% respectively for the 588.6N sample. The 981.0N sample produced differences of 34.8% and 69.9% for the minor and major strain respectively. The 1471.5N sample produced differences of 26.0% and 38.8% for the minor and major strain respectively.

Although it was found that these differences are fairly large when analyzing the percentages, the difference in strain values are still typically within the measurement error of ±0.04µm/µm. Along with the differences, it was also found that there are several possible explanations as to why some of the data points exhibited a larger difference in comparison. These reasons could be due to the multiphase nature of AISI 4340 steel causing a micro scale non-homogeneous material response between the pearlite and ferrite grains. This would cause an increase in difference when compared to the macro scale response from the FE model. It is for this reason that caution should be taken when attempting to apply FE results to microscale non-homogeneous materials. Aside from the material itself, differences between the experimental and FE results could arise due to the manual measurement used within this work. Although an error of ±0.04µm/µm strain was determined, it is not a set constant value due to human involvement in the measurements and therefore could allow for large variations in what the value should be.

The results from this work show that the free interface within NBIT causes a small difference in the material response from an indentation, as well as a small difference in residual strain when compared to a FE model. From these results, NBIT can be utilized in future research as it has a large range of possible spatial resolutions from a gauge size of 256µm to potentially sub-micron level depending on the power and accuracy of the FIB as well as the accuracy of the microscope used for the measurements.

5.1 Future Recommendations

For future work, if further comparison is desired between NBIT and a finite element model, the use of a single phase material should show a better comparison. Also, upon further review, the Johnson-Cook material model could also be replaced with a newer, more advanced plasticity model which would be able to better represent an experimental sample. Aside from those two recommendations, the development towards an accurate ellipse detection or some form of image correlation which would allow for automatic detection of the residual major and minor axes would increase the efficiency and accuracy of this method significantly and allow for continued testing for better reliability.

Publications generated from this work:

1. Journal of Engineering Materials and Technology
    - A Novel Method of Residual Strain Analysis via a Non-Bonded Interface Technique in Combination with the Circular Grid Analysis Method
2. Canadian Congress of Applied Mechanics 2019 Conference Proceedings
    - Comparison Between a Novel Residual Strain Analysis Method and a Finite Element Model

Bibliography

[1] F. Guiberteau, N. P. Padture, and B. R. Lawn, "Effect of Grain Size on Hertzian Contact Damage in Alumina," *Journal of the American Ceramic Society*, vol. 77, pp. 1825–1831, jul 1994.

[2] H. Helbawi, L. Zhang, and I. Zarudi, "Difference in subsurface damage in indented specimens with and without bonding layer," *International Journal of Mechanical Sciences*, vol. 43, no. 4, pp. 1107–1121, 2001.

[3] A. Almotairi, *Mechanical and Thermal Damage of Hard Chromium Coatings on 416 Stainless Steel*. PhD thesis, Dalhousie University, Halifax, Nova Scotia, 2016.

[4] K. Hariharan and S. Suresh, "Comparison of Optical Strain Analysis and Circular Grid Analysis in Sheet Metal Forming," *SAE Technical Papers*, no. 724, 2007.

[5] W. H. Bragg and W. L. Bragg, "The Reflection of X-rays by Crystals," *Proceedings of the Royal Society A: Mathematical, Physical and Engineering Sciences*, vol. 88, pp. 428–438, jul 1913.

[6] I. C. Noyan and J. B. Cohen, *Residual Stress: Measurement by Diffraction and Interpretation*. Springer, 1987.

[7] P. J. Withers, M. Turski, L. Edwards, P. J. Bouchard, and D. J. Buttle, "Recent advances in residual stress measurement," *International Journal of Pressure Vessels and Piping*, vol. 85, no. 3, pp. 118–127, 2008.

[8] S. Ganguly, V. Stelmukh, M. E. Fitzpatrick, and L. Edwards, "Use of neutron and synchrotron X-ray diffraction for non-destructive evaluation of weld residual stresses in aluminium alloys," *Journal of Neutron Research*, vol. 12, no. 1-3, pp. 225–231, 2004.

[9] T. S. Jun, F. Hofmann, J. Belnoue, X. Song, M. Hofmann, and A. M. Korsunsky, "Triaxial residual strains in a railway rail measured by neutron diffraction," *Journal of Strain Analysis for Engineering Design*, vol. 44, no. 7, pp. 563–568, 2009.

[10] D. C. Harris, *Symmetry and spectroscopy : an introduction to vibrational and electronic spectroscopy*. New York: New York : Dover Publications, 1989.

[11] L. S. Schadler and C. Galiotis, “Fundamentals and applications of micro Raman spectroscopy to strain measurements in fibre reinforced composites,” *International Materials Reviews*, vol. 40, pp. 116–134, jan 1995.

[12] G. P. Xu, G. Xu, Z. M. Yin, and R. C. Jiang, “Micro-Raman Stress Investigation of Polycrystalline Diamond Compact (PDC),” *Advanced Materials Research*, vol. 76-78, pp. 690–695, 2009.

[13] C. A. Michaels and R. F. Cook, “Determination of residual stress distributions in polycrystalline alumina using fluorescence microscopy,” *Materials and Design*, vol. 107, no. June 2016, pp. 478–490, 2016.

[14] S. Sathish, T. J. Moran, R. W. Martin, and R. Reibel, “Residual stress measurement with focused acoustic waves and direct comparison with X-ray diffraction stress measurements,” *Materials Science and Engineering A*, vol. 399, no. 1-2, pp. 84–91, 2005.

[15] J. W. Wilson, G. Y. Tian, and S. Barrans, “Residual magnetic field sensing for stress measurement,” *Sensors and Actuators, A: Physical*, vol. 135, no. 2, pp. 381–387, 2007.

[16] S. P. Sagar, B. R. Kumar, G. Dobmann, and D. K. Bhattacharya, “Magnetic characterization of cold rolled and aged AISI 304 stainless steel,” *NDT and E International*, vol. 38, no. 8, pp. 674–681, 2005.

[17] G. Shui, C. Li, and K. Yao, “Non-destructive evaluation of the damage of ferromagnetic steel using metal magnetic memory and nonlinear ultrasonic method,” *International Journal of Applied Electromagnetics and Mechanics*, vol. 47, no. 4, pp. 1023–1038, 2015.

[18] S. Robert, S. Nadja, K. Marc, and S. Birgit, “Self-magnetic-leakage field detection using magneto-optical sensor technique,” *MATEC Web of Conferences*, vol. 12, p. 04010, 2014.

[19] S. Ferreira, D. Silva Júnior, T. Rodrigues Mansur, J. Ricardo, B. Cruz, and M. M. Neto, “the Use of Magnetic Barkhausen Noise Analysis for Nondestructive Determination of Stresses in Structural Elements,” in *International Nuclear Atlantic Conference*, no. December 2015, (Santos), ABEN, 2007.

[20] J. Mathar, “Determination of initial stresses by measuring the deformation around drilled holes,” *Transactions ASME*, vol. 56, no. 4, 1934.

[21] ASTM E837-13a, "Standard Test Method for Determining Residual Stresses by the Hole-Drilling Strain-Gage Method," *Standard Test Method E837-13a*, vol. i, pp. 1–16, 2013.

[22] H. Kitano, S. Okano, and M. Mochizuki, "A study for high accuracy measurement of residual stress by deep hole drilling technique," *Journal of Physics: Conference Series*, vol. 379, no. 1, 2012.

[23] M. B. Prime and G. A. R., "The Contour Method: Simple 2-D Mapping of Residual Stresses," vol. 836, pp. 1–4, 2001.

[24] H. Bueckner, "The propagation of cracks and the energy of elastic deformation," *Transactions of the American Society of Mechanical Engineers*, vol. 80, no. 6, pp. 1225–1230, 1958.

[25] M. E. Kartal, "Analytical solutions for determining residual stresses in two-dimensional domains using the contour method," *Proceedings of the Royal Society A: Mathematical, Physical and Engineering Sciences*, vol. 469, no. 2159, 2013.

[26] H. Yu, Z. Sun, H. Zhao, and M. H. Zhu, "Stress Analysis of Bonded-Interface Technique on Subsurface Damage Observations of Brittle Porcelains," *Key Engineering Materials*, vol. 353-358, pp. 864–867, 2007.

[27] Y. F. Gao, B. Yang, and T. G. Nieh, "Thermomechanical instability analysis of inhomogeneous deformation in amorphous alloys," *Acta Materialia*, vol. 55, no. 7, pp. 2319–2327, 2007.

[28] U. Ramamurty, S. Jana, Y. Kawamura, and K. Chattopadhyay, "Hardness and plastic deformation in a bulk metallic glass," *Acta Materialia*, vol. 53, no. 3, pp. 705–717, 2005.

[29] D. J. Green, *An introduction to the mechanical properties of ceramics*. Cambridge: Cambridge : Cambridge University Press, 1998.

[30] H. R. Hertz, "On the Contact of Elastic Solids," *Journal für die reine und angewandte Mathematik*, vol. 1882, no. 92, pp. 156–171, 1882.

[31] A. C. Fischer-Cripps, *Introduction to Contact Mechanics*. Springer, 2016.

[32] M. T. Huber, "Zur Theorie der Berührung fester elastischer Körper," *Annalen der Physik*, vol. 319, no. 6, pp. 153–163, 1904.

[33] S. Timoshenko, *Theory of Elasticity*. New York and London: McGraw-Hill, first ed., 1934.

[34] D. Tabor, *The Hardness of Metals*, vol. 24. Oxford: Claredon Press, 1951.

[35] R. M. Davies, “The Determination of Static and Dynamic Yield Stresses Using a Steel Ball,” *Proceedings of the Royal Society A: Mathematical, Physical and Engineering Sciences*, vol. 197, no. 1050, pp. 416–432, 1949.

[36] D. Tabor, “A Simple Theory of Static and Dynamic Hardness,” *Proceedings of the Royal Society A: Mathematical, Physical and Engineering Sciences*, vol. 192, no. 1029, pp. 247–274, 1948.

[37] L. Samuels and T. Mulhearn, “An experimental investigation of the deformed zone associated with indentation hardness impressions,” *Journal of the Mechanics and Physics of Solids*, vol. 5, no. 2, pp. 125–134, 1957.

[38] T. O. Mulhearn, “The deformation of metals by vickers-type pyramidal indenters,” *Journal of the Mechanics and Physics of Solids*, vol. 7, no. 2, pp. 85–88, 1959.

[39] K. L. Johnson, “The correlation of indentation experiments,” *Journal of the Mechanics and Physics of Solids*, vol. 18, no. 2, pp. 115–126, 1970.

[40] R. Hill, *The Mathmatical Theory of Plasticity*. Oxford: Oxford University Press, 1950.

[41] D. M. Marsh, “Plastic Flow in Glass,” *Proceedings of the Royal Society A: Mathematical, Physical and Engineering Sciences*, vol. 279, pp. 420–435, jun 1964.

[42] K. L. Johnson and L. M. Keer, “Contact Mechanics,” *Journal of Tribology*, vol. 108, no. 4, p. 659, 1986.

[43] X. L. Gao, X. N. Jing, and G. Subhash, “Two new expanding cavity models for indentation deformations of elastic strain-hardening materials,” *International Journal of Solids and Structures*, vol. 43, no. 7-8, pp. 2193–2208, 2006.

[44] I. D. Marinescu, W. B. Rowe, B. Dimitrov, and H. Ohmori, *Tribology of Abrasive Machining Processes*. Elsevier, 2012.

[45] R. L. Jackson, H. Ghaednia, and S. Pope, “A Solution of Rigid–Perfectly Plastic Deep Spherical Indentation Based on Slip-Line Theory,” *Hydrobiologia*, vol. 764, no. 1, pp. 1–7, 2016.

[46] A. D. Tomlenov, “Eindringen eines abgerundeten Stempels in ein Metall unter Vorhandensein von Reibung,” *Vestn. Mashinostr.*, vol. 40, pp. 56–58, 1960.

[47] R. Hill, E. Lee, and S. Tupper, “The Theory of Wedge Indentation of Ductile Materials,” *Proceedings of the Royal Society of London. Series A, Mathematical and Physical Sciences*, vol. 188, no. 1013, pp. 273–289, 1947.

[48] B. Szabó and I. Babuška, *Introduction to Finite Element Analysis*. Chichester, UK: John Wiley & Sons, Ltd, mar 2011.

[49] O. C. Zienkiewicz and R. L. Taylor, *The Finite Element Method Vol. 1 : The Basis*. Butterworth-Heinemann, 5 ed., 2000.

[50] M. A. Bhatti, *Advanced topics in finite element analysis of structures : with Mathematica and MATLAB computations*. Hoboken, N.J.: Hoboken, N.J. : Wiley, 2006.

[51] B. Zhu, *The finite element method : fundamentals and applications in civil, hydraulic, mechanical and aeronautical engineering*. 2018.

[52] M. Crisfield, *Nonlinear Finite Element Analysis of Solids and Structures: Advanced Topics*, vol. 2. 1996.

[53] D. Anderson, A. Warkentin, and R. Bauer, "Simulation of Deep Spherical Indentation Using Eulerian Finite Element Methods," *Journal of Tribology*, vol. 133, no. 2, p. 021401, 2011.

[54] D. J. Benson, "Computational methods in Lagrangian and Eulerian hydrocodes," *Computer Methods in Applied Mechanics and Engineering*, vol. 99, no. 2-3, pp. 235–394, 1992.

[55] S. Krenk, "Non-linear bar elements," in *Non-linear Modeling and Analysis of Solids and Structures*, pp. 17–46, Cambridge University Press, 2009.

[56] C. Zhangxin, *Finite Element Methods and Their Applications*. Springer Berlin Heidelberg, 2005.

[57] E. Dintwa, E. Tijskens, and H. Ramon, "On the accuracy of the Hertz model to describe the normal contact of soft elastic spheres," *Granular Matter*, vol. 10, no. 3, pp. 209–221, 2008.

[58] G. R. Johnson and W. H. Cook, "A constitutive model and data for metals subjected to large strains, high strain rates and high temperatures," 1983.

[59] D. A. Doman, "Rubbing & plowing phases in single grain grinding," no. August, 2008.

[60] F. Wang, J. Zhao, N. Zhu, and Z. Li, "A comparative study on Johnson-Cook constitutive modeling for Ti-6Al-4V alloy using automated ball indentation (ABI) technique," *Journal of Alloys and Compounds*, vol. 633, pp. 220–228, 2015.

[61] LSTC, "Keyword Users Manual (Material Models)," 2011.

[62] N. Kikuchi and J. T. Oden, *Contact Problems in Elasticity*. Society for Industrial and Applied Mathematics, jan 1988.

[63] J. O. Hallquist, G. L. Goudreau, and D. J. Benson, "Sliding interfaces with contact-impact in large-scale Lagrangian computations," *Computer Methods in Applied Mechanics and Engineering*, vol. 51, no. 1-3, pp. 107–137, 1985.

[64] LSTC, "LS-DYNA Theory Manual," 2017.

[65] J. L. Bucaille, S. Stauss, E. Felder, and J. Michler, "Determination of plastic properties of metals by instrumented indentation using different sharp indenters," *Acta Materialia*, vol. 51, no. 6, pp. 1663–1678, 2003.

[66] J. Alcalá and D. Esqué-De Los Ojos, "Reassessing spherical indentation: Contact regimes and mechanical property extractions," *International Journal of Solids and Structures*, vol. 47, no. 20, pp. 2714–2732, 2010.

[67] X. H. Tan and Y. L. Shen, "Modeling analysis of the indentation-derived yield properties of metallic multilayered composites," *Composites Science and Technology*, vol. 65, no. 11-12, pp. 1639–1646, 2005.

[68] E. Harsono, S. Swaddiwudhipong, and Z. S. Liu, "The effect of friction on indentation test results," *Modelling and Simulation in Materials Science and Engineering*, vol. 16, no. 6, p. 065001, 2008.

[69] S. Carlsson, S. Biwa, and P. L. Larsson, "On frictional effects at inelastic contact between spherical bodies," *International Journal of Mechanical Sciences*, vol. 42, no. 1, pp. 107–128, 2000.

[70] S. D. Mesarovic and N. A. Fleck, "Spherical indentation of elastic-plastic solids," *Proceedings of the Royal Society A: Mathematical, Physical and Engineering Sciences*, vol. 455, no. 1987, pp. 2707–2728, 1999.

[71] ASM International Handbook Committee., "Carbon and Low-Alloy Steels," in *ASM Handbook, Volume 1: Properties and Selection: Irons, Steels, and High-Performance Alloys*, ASM International, 1998.

[72] ASM International Handbook Committee, *Materials Characterization*, vol. 10. ASM International, 1986.

[73] W. Fortune Smith, *Structure and Properties of Engineering Alloys*. McGraw-Hill, 2nd ed., 1993.

[74] MatWeb, "AISI 4340 Steel," 2019.

[75] V. N. Kulkarni, N. Shukla, and N. S. Rajput, "Micro- and Nanomanufacturing by Focused Ion Beam," in *Micromanufacturing Processes* (V. K. Jain, ed.), pp. 113–130, Taylor and Francis Group, 2013.

[76] C. Kocer and R. E. Collins, "Angle of Hertzian Cone Cracks," *Journal of the American Ceramic Society*, vol. 81, no. 7, pp. 1736–1742, 2010.

[77] M. R. Begley, A. G. Evans, and J. W. Hutchinson, "Spherical impression of thin elastic films on elastic–plastic substrates," *International Journal of Solids and Structures*, vol. 36, no. 18, pp. 2773–2788, 1999.

[78] O. C. Zienkiewicz, R. L. Taylor, and J. Z. Zhu, *Finite Element Method - Its Basis and Fundamentals*. Elsevier, 6 ed., 2005.

[79] W. K. Rule, “A numerical scheme for extracting strength model coefficients from Taylor test data,” *International Journal of Impact Engineering*, vol. 19, no. 9-10, pp. 797–810, 1997.